University of Nevada, Reno

Applications of multi-season hyperspectral remote sensing for acid mine water characterization and mapping of secondary iron minerals associated with acid mine drainage

A thesis submitted in partial fulfillment of the
requirements for the degree of Master of Science in
Hydrogeology

by

Gwendolyn E. Davies

Dr. Wendy M. Calvin/Thesis Advisor

December, 2015

N

We recommend that the thesis
prepared under our supervision by

GWENDOLYN E. DAVIES

entitled

Applications of Multi-Season Hyperspectral Remote Sensing for Acid Mine Water Characterization and Mapping of Secondary Iron Minerals Associated with Acid Mine Drainage

be accepted in partial fulfillment of the
requirements for the degree of

MASTER OF SCIENCE

Wendy M. Calvin, Ph.D., Advisor

Simon R. Poulson, Ph.D., Committee Member

Glenn C. Miller, Ph.D., Graduate School Representative

David W. Zeh, Ph.D., Dean, Graduate School

December, 2015

Abstract:

Acid mine drainage (AMD) resulting from the oxidation of sulfides in mine waste is a major environmental issue facing the mining industry today. Open pit mines, tailings ponds, ore stockpiles, and waste rock dumps can all be significant sources of pollution, primarily heavy metals. These large mining-induced footprints are often located across vast geographic expanses and are difficult to access. With the continuing advancement of imaging satellites, remote sensing may provide a useful monitoring tool for pit lake water quality and the rapid assessment of abandoned mine sites. This study explored the applications of laboratory spectroscopy and multi-season hyperspectral remote sensing for environmental monitoring of mine waste environments. Laboratory spectral experiments were first performed on acid mine waters and synthetic ferric iron solutions to identify and isolate the unique spectral properties of mine waters. These spectral characterizations were then applied to airborne hyperspectral imagery for identification of poor water quality in AMD ponds at the Leviathan Mine Superfund site, CA. Finally, imagery varying in temporal and spatial resolutions were used to identify changes in mineralogy over weathering overburden piles and on dry AMD pond liner surfaces at the Leviathan Mine. Results show the utility of hyperspectral remote sensing for monitoring a diverse range of surfaces associated with AMD.

Acknowledgements:

I would like to extend my gratitude to the many people who supported me during this endeavor. Foremost, I would like to thank Dr. Wendy Calvin for her guidance, compassion, and patience during my time at the University of Nevada, Reno. I feel very fortunate to have been handpicked by such an esteemed scientist to work on a project so aligned with my interests. I am deeply grateful for her financial support throughout my entire program of study. Additionally, I must thank Dr. Calvin for supporting and understanding my brief hiatus from school to finish hiking the Appalachian Trail.

I would like to recognize Dr. Simon Poulson and Dr. Glenn Miller for serving as advisory committee members and providing very valuable comments for several drafts of this thesis. Furthermore, I thank Dr. Poulson for the use of his laboratory and field equipment, which were so vital to this research.

I would like to sincerely thank Doug Carey and Taylor Zetner at the Lahontan Regional Water Quality Control Board for graciously supporting my field work at the Leviathan Mine. I appreciate Doug for his encouragement to find a career rich in adventure.

I would like to thank my boyfriend and field assistant Dylan Baldwin for not only providing loving support but also expert geologic guidance. I must also thank my lab mates Neil Pearson and Tim Cramer for their wonderful comradery and for providing invaluable assistance while deciphering image processing software.

I would like to acknowledge my former supervisor Corey Meier for inviting me to work in Butte, Montana—a job which will forever shape my career aspirations toward the protection of environmental quality. I would also like to acknowledge another former supervisor, Misty Vermulm, for giving me so much positive encouragement and confidence in my work.

Last but certainly not least, I would like to thank my family. Mom, Dad, Ryan, and Yoonmi—thank you for your eternal love and support during all my high and low points.

Table of Contents:

Introduction:

The impacts of mineral extraction may be detrimental to environmental quality and human health by impacting surface and ground waters. There is a constant need to refine resource monitoring and management techniques with new advances in science and technology. The task of quantifying the impacts of past and current resource extraction and their evolution over time will provide valuable information which may be used to manage our natural resources more efficiently. The following work will explore the applications of laboratory, ground based, and airborne spectroscopy of water and sediment targets for environmental quality monitoring. These applications could be used by a variety of federal and private environmental monitors and regulators. This work will hopefully expand global spectral libraries of mine waste surfaces and further support the rapid assessment of mining induced environmental contamination.

This study used laboratory, field, and airborne imagery data collected over Leviathan Mine Superfund site located in California. This work was supported by the NASA HyspIRI Preparation Data campaign using airborne imagery collected in 2013 and 2014.

Chapter 1—Manuscript submitted to Mine Water and the Environment (Submitted September 17, 2015)

Title: Quantifying iron concentration in local and synthetic acid mine drainage waters: A new technique using handheld field spectrometers.

Authors: Gwendolyn Davies, Wendy Calvin

Abstract:

Pit lakes present a concern for public safety and environmental quality. They are often located across large geographic expanses and are difficult to access. With continuing advancement of imaging satellites, remote sensing spectroscopy may provide a useful monitoring tool for identifying pit water quality across vast mining districts. Visible to shortwave infrared remote sensing has been widely used to monitor acid mine drainage mineralogy at mine sites. However, few studies have examined the spectral signatures of mine-affected waters and open pit water bodies from a remote platform. The motivation for this study was to identify the spectral characteristics of acid mine waters in a controlled laboratory setting in order to better interpret acid mine water bodies in remote sensing imagery. The spectral response of synthetic and local acid mine waters were measured using a field spectrometer. Increasing ferric and ferrous iron concentration solutions were mixed in order to mimic the chemical properties of local acid mine waters. Synthetic solutions with known iron concentrations were compared with local acid mine waters for quantitative assessment. The spectral signatures of ferric iron dominated waters possessed distinct characteristics which may be used for diagnostic identification. Specifically, the region between 0.35 and 0.625 µm was used to approximately quantify ferric iron concentration. Subtle changes in iron concentration in local acid mine waters due to environmental and seasonal conditions were identified using a field spectrometer alone. These findings suggest subtle changes in open pit water quality may also be qualitatively and quantitatively measured by remote sensing spectroscopy.

Keywords: Mine Waste, Spectroscopy, Aqueous Ferric Iron, Environmental Monitoring

1.   Introduction

One of the largest environmental issues facing the global mining industry is the water quality of open pit lakes (Castendyk and Eary 2009). Within the next ten years almost 50 open pit mines, which intercept the groundwater table, will be completed in the United States (Vandersluis 1995). In the state of Nevada alone, 35 mines will have a lake in their open pit after dewatering ceases (Shevenell 1999). Improved technologies for monitoring these potentially environmentally hazardous features are needed. Open pits range in size from relatively small borrows about 100 m in diameter, to enormous open cut operations such as the Bingham Canyon copper mine in Utah, which measures 4 km wide and 1.2 km deep (McCullough et al. 2011; Castendyk and Eary 2009). These large footprints are observable from imaging satellites (Peichang et al. 2004; Sanliyuksel et al. 2014). With the continuing advancement of imaging satellites, remote sensing may provide a useful monitoring tool for snapshots of pit water quality across large western mining districts.

This paper will explore the potential use of visible to short wave infrared (VSWIR) spectroscopy for water quality analysis relating to pit lakes. The results of this paper are intended to lay a foundation for subsequent application to remote sensing spectroscopy. The objectives are to 1) identify the unique spectral response of acid mine discharge from a local source in a laboratory setting, 2) identify the spectral response of simplified synthetic mine water in a laboratory setting, and 3) compare the local and synthetic datasets in order to make a qualitative and quantitative assessment on the diagnostic spectral features of acid mine waters.

2.   Background

The oxidation of sulfide minerals releases hydrogen ions into mine waters, in addition to liberating metals and sulfate into solution. Acid mine drainage (AMD) is associated with the release of sulfate, heavy metals (Fe, Cu, Pb, Zn, Cd, Co, Cr, Ni, Hg), metalloids (As, Sb, Se, Te), and other elements (Si, Ca, Na, K, Mg, Ba) (Lottermoser 2003). These waters are characterized by exceptionally high sulfate (>1000 mg/L), high iron and aluminum (>100 mg/L), and elevated copper, chromium, nickel, lead, and zinc concentrations (>10 mg/L) (Lottermoser 2003). Many pit lakes from former gold, metal-sulfide, or coal mines contain significant concentrations of heavy metals and/or metalloids, acidic pH, high total dissolved solids (TDS), and elevated turbidity (Gammons 2009).

The iron cation strongly affects the 0.4 to 1.1 μm portion of the VSWIR region, producing diagnostic absorption minima which may be used for mineral identification (Hunt and Ashley 1979; Burns 1993). Iron was chosen for the focus of this study because of its spectral robustness and occurrence in high concentrations in pit lakes. Poor water quality in open pit lakes or AMD discharge is commonly recognized by the water's intense red color associated with high iron concentrations. One of the most extreme

examples of this is the Berkeley Pit Lake in southwestern Montana. Approximately 39 billion gallons of red water are contained in the lake, with a surface water composition of pH 2.75 and 484 mg/L Fe (Duaime and Tucci 2009).

This study will examine the AMD waters at the Leviathan Mine Superfund site, located in the Monitor Pass mining district in Alpine County, California (Fig. 1). Leviathan Mine is a high sulfidation epithermal replacement deposit (Evans 1977; California Regional Water Quality Control Board 2015). Approximately 500,000 tons of native sulfur were extracted from Leviathan during open pit mining from 1952-1962 (Evans 1977). The primary source of AMD emanates from discharging groundwater from a remnant tunnel and adit structure. Currently, AMD is collected in a series of evaporation ponds and treated at an on-site facility (California Regional Water Quality Control Board 2015). Fresh AMD from the adit/tunnel is piped into the south end of Pond 1 (Fig. 1). From there, water is distributed between Ponds 1, Pond 2 South, and Pond 2 North, which are interconnected and are at the same elevation. Excess water may be released down to Pond 3 for additional storage if necessary. Water is stored in the ponds throughout the winter and spring before being pumped into the treatment facility in mid-summer. As the AMD water oxidizes and accumulates in the ponds it becomes strikingly red in color (Figs. 1 and 2). During the time of this study Pond 3 was not used for AMD storage. Water was only present in Pond 3 in the spring and contained meteoric water. In 2014, AMD was treated between September 8 and 12.

3. Methods

    a. Local AMD Waters

Reconnaissance data was collected at Leviathan Mine on 05/22/14. Water samples were taken near the inlet pipe in Pond 1, on the east shore of Pond 2 South, and on the south edge of Pond 3. Samples were collected in HDPE bottles supplied by SEM, Inc. (Reno, NV), stored on ice, and delivered to the SEM, Inc. laboratory for basic water chemistry analysis including major anions/cations, trace elements, ferric/ferrous iron, TDS, pH, redox potential, and turbidity (Al, B, Ca, Fe, Mg, K, SiO_2, and Na by ICP-OES; Sb, As, Ba, Be, Cd, Cr, Co, Pb, Mn, Ni, Se, Ag, TI, and Zn by ICP-MS; Cl, F, NO_3, and SO_4 by Ion Chromatography; Hg by AA Cold Vapor).

Water samples for laboratory spectral analysis were taken on 08/08/14 and 10/09/14. At each visit, water samples were collected in HDPE Nalgene containers from all ponds with standing water, stored on ice, and analyzed within 48 hrs. Samples were taken directly from the inlet pipe in Pond 1, on the north shore of Pond 1, and on the east shore of Pond 2 North (Pond 2 North was safer to access for sampling than Pond 2 South on 08/08/14 and 10/09/14). On all sampling occasions field pH was measured with a Double Junction Waterproof pHTestr 20, calibrated using pH 4 and 7 buffer solutions.

On 08/08/14, Pond 3 had dried up while Pond 1, Pond 2 North, and Pond 2 South were slightly lower than their previous levels on 05/22/14. On 10/09/14, water samples were collected from Pond 1 at the inlet and Pond 2 North, and analyzed for ferric/ferrous iron, TDS, pH, redox potential, and turbidity by SEM, Inc. Because iron was identified as the principal spectral absorption component in local AMD waters, a full set of metal analysis was deemed unnecessary. During the 10/09/14 sampling, Pond 2 South was essentially dried up, while Pond 2 North still contained several inches of water. Pond 1 was notably lower than its level during the previous two samplings.

Each water sample was filtered through a 0.45 μm cellulose nitrate filter membrane in order to separate fine particulates. Two spectral measurements were made on each water sample; filtered and unfiltered solutions. Spectral measurements were taken using a FieldSpec ASD spectrometer, which collects spectral reflectance from 0.35-2.5 μm in 2,151 bands at 1 nm sampling interval. 100 mL of each solution was placed in a 150 mL Pyrex beaker, resting on top of a halon plate (white reference which contains no spectral features). Spectral measurements were made in a dark room using the ASD's contact probe with halogen light source. The probe was placed on top of the beaker just above the water level. The ASD collection program was set to average 60 individual spectra in each measurement to minimize noise. The resulting spectral response was a combination of water surface reflectance, volume reflectance within the beaker, and bottom reflectance from the halon plate (Fig. 3).

The filtrates were stored in covered plastic petri dishes and allowed to dry at room temperature. Spectral measurements were made directly on the filter paper using the contact probe with halogen light source. A blank filter was also measured, making it possible to distinguish the properties exclusive to the filter membranes.

For comparison to natural water bodies, an additional water sample was taken on 08/07/14 from the East Fork of the Carson River, about 6 miles west of Leviathan Mine on CA highway 89. It had rained several days prior to this sampling and the river was particularly turbid.

b. Synthetic AMD Solutions

Synthetic ferric iron solutions were prepared by dissolving reagent grade iron (III) sulfate hydrate ($Fe_2(SO_4)_3$, Sigma Aldrich) into deionized (DI) water. Fifteen solutions of increasing ferric iron concentration were produced to mimic the concentrations typically observed in AMD (25-5000 mg/L Fe^{3+}). 100 mL of DI water was mixed with reagent in a 150 mL Pyrex beaker with glass stirring rod. The solutions were stirred until no undissolved $Fe_2(SO_4)_3$ particulates were visibly suspended. The pH of the solutions was monitored throughout the experiment. When $Fe_2(SO_4)_3$ dissolves into water, protons are produced by the hydrolysis of $Fe_2(SO_4)_3$ and the pH is reduced. The resulting solution pHs were comparable to that of Leviathan's waters (pH 3.06-1.73). Spectral measurements were made immediately

after mixing using the same technique stated above. The solutions varied visually from a faint brown color in the 25 mg/L Fe^{3+} solution to dark reddish brown color in the 5000 mg/L Fe^{3+} solution.

Using the same techniques, a second batch of synthetic solutions were made with ferrous iron. Reagent grade iron (II) sulfate heptahydrate ($FeSO_4 \cdot 7H_2O$, Sigma Aldrich) was dissolved in DI water. Eight different solutions of increasing ferrous iron concentration were produced to mimic the concentrations typically observed in AMD (25-1000 mg/L Fe^{2+}). The solutions were again mixed until no undissolved particles were visually suspended. The solution pHs were acidified to approximately 2.7 using dilute sulfuric acid (H_2SO_4). All solutions were colorless.

The spectral data was analyzed using the continuum removed (CR) method (Clark and Roush 1984). The continuum of a spectrum is a convex hull fit over the top of the spectrum using straight-line segments that connect spectral maximums (Kruse and Lefkoff 1993). The continuum is always convex and does not cross through the original spectrum (Fig. 4). Dividing the spectrum by its continuum results in a CR spectrum containing normalized reflectance values from 0.0 to 1.0. Absorption features, which occur superimposed on a background slope in the original data, are transformed into features with a uniform, flat background of 1.0 in the CR spectrum. This allows the strength (band depth) of each absorption feature to be quantitatively analyzed with respect to a consistent reference level.

4. Results

    a. Local AMD Waters

        i. Water Chemistry

Water chemistry analyses from 05/22/14 and 10/09/14 are summarized in Tables 1 and 2, respectively. The chemistry of Pond 1 inlet and Pond 2 South on 05/22/14 were similar. The pH was very acidic (2.6 - 2.8) and the waters contained substantial concentrations of heavy metals and sulfate. Most ion concentrations were comparable between the two. Pond 1 inlet had a slightly lower redox potential than Pond 2 South; 663 vs. 721 mV, respectively. As a result, iron speciation was different between the two samples. Pond 1 inlet contained mostly reduced ferrous iron, while Pond 2 South contained mostly oxidized ferric iron (Fe^{3+}/Fe^{2+} ratios for Pond 1 inlet and Pond 2 South were 0.179 and 8.75, respectively). The chemistry of Pond 3 was considerably different from the other ponds. Although still very poor in quality, Pond 3 had a higher pH and did not contain exceptionally high iron concentrations. Pond 3 had notably higher concentrations of Al, Co, Mg, Mn, and Zn, and high turbidity. Samples from Pond 2 South and Pond 3 were brown to light-brown in color, while the sample from the Pond 1 inlet was colorless. TDS for all three samples ranged from 4800 to 6800 mg/L.

On 10/09/14 the iron chemistry of the Pond 1 inlet and Pond 2 North were drastically different. The total iron content in Pond 2 North was over four times as high as Pond 1 inlet (2215 mg/L Fe, 530 mg/L Fe). The redox potentials from Pond 1 inlet and Pond 2 North were comparable to those from the 05/22/14 sampling. Pond 1 inlet had lower redox potential than Pond 2 North; 619 mV vs. 794 mV, respectively. Once more, Pond 1 contained dominantly reduced ferrous iron, while Pond 2 North contained almost entirely oxidized ferric iron (Fe^{3+}/Fe^{2+} ratios for Pond 1 inlet and Pond 2 North were 0.060 and 146, respectively). Pond 2 North had an extremely high TDS of 33000 mg/L, while Pond 1 had a value comparable to the 05/22/14 sampling (3700 mg/L TDS). The Pond 2 North sample was dark brown in color, while the sample from the Pond 1 inlet was again colorless.

ii.   Water Spectroscopy

All spectral curves for local AMD waters are displayed in Fig. 5 and 6. The DI water spectral curve was relatively featureless until the appearance of broad absorption features centered at 0.763 and 0.975 μm, followed by a steep decreasing slope to virtually 100 percent absorption beyond 1.15 μm (Fig. 5c). This spectral curve served as a "blank" and demonstrated the spectral features of pure water. The absorption features at 0.763 μm, 0. 975 μm, and beyond 1.15 μm were characteristic of the water molecule in the liquid phase (Dozier and Painter 2004; Green et al. 2006). Liquid water exhibits multiple absorption features between 0.4 and 2.5 μm, which result from combinations of three fundamental vibrational modes of the water molecule. These fundamental absorptions occur beyond the VSWIR region near 2.9, 3.1, and 6.1 μm, but their combinations and overtones occur in the VSWIR region (Green et al. 2006).

Generally, the curves of local AMD waters were characterized by virtually no reflectance below 0.4 μm, with an increasing slope through the blue/green regions (0.4-0.65 μm), and a peak reflectance between 0.65-0.66 μm (Fig. 5a-b). The absorption features in the local AMD curves were identical to those in the DI water curve from 0.763 μm onward. There was notable variation between local AMD waters in the 0.35-0.65 μm region. Pond 1 from the inlet had the least absorption in the blue/green region with a very slight inflection point at 0.453 μm. Pond 1 from the north shore had more absorption in the blue/green region with a more pronounced 0.453 μm inflection, and emergence of a second absorption feature at 0.54 μm. Pond 2 North had the lowest reflectance level in the blue/green region and a prominent 0.54 μm shoulder. Pond 3 had low reflectance on the edge of the UV, but did not exhibit any absorption features in the blue/green region (Fig. 5c). It had a curve more closely resembling that of DI water. The turbid Carson River sample was essentially featureless with no reflectance (Fig. 5c).

There was little variation in spectral features between the filtered and unfiltered local AMD waters. However, the filtered samples generally had lower overall reflectance than their filtered

counterparts, with the exception being the filtered Carson River sample, which had a curve almost identical to that of DI water after filtering removed all suspended sediments.

In CR format, the region of greatest interest was between 0.35-0.625 µm (Fig. 6). An absorption feature occurred in the blue/green region for both Pond 1 and Pond 2 North (Fig. 6a-b). In August and October, Pond 1 from the inlet had an absorption feature centered at wavelengths less than 0.38 µm. Pond 1 from the north shore in October had an absorption feature centered at slightly longer wavelengths and a second smaller feature between 0.43-0.47 µm. Pond 2 North had the broadest overall absorption centered at the longest wavelengths with two features centered near 0.44 and 0.55 µm. In August, the Pond 1 north shore and Pond 2 North spectral shapes are quite similar to each other and most similar to the shape from Pond 2 North in October. Pond 3 and the filtered Carson River had no absorption features in this range (Fig. 6c). The unfiltered Carson River showed lower overall CR reflectance, however the spectral shape was dramatically different than the AMD curves.

b. Synthetic AMD Solutions

i.   Water Spectroscopy

Spectral curves for synthetic AMD solutions are displayed in Fig. 7 and 8. The ferric iron solutions had virtually no reflectance below 0.4 µm, then steeply increased from 0.38-0.433 µm followed by an inflection point centered at 0.453 µm (Fig. 7a). Peak reflectance occurred at about 0.66 µm, followed by a broad absorption feature centered at 0.763 µm and a second feature centered at 0.975 µm, with near 100 percent absorption beyond 1.15 µm. With increasing ferric iron concentration, the inflection point at 0.453 µm began to deepen. Approaching higher concentrations, a shoulder appeared at 0.54 µm, masking the shorter wavelength feature. Generally, reflectance decreased as ferric iron sulfate concentrations increased.

In CR format the absorption feature occurring in the blue/green region broadened, and the band center shifted to longer wavelengths in the higher ferric iron concentration solutions (Fig. 8a). For example, the 50 mg/L ferric iron solution's band center occurred at 0.375 µm, while the 5000 mg/L ferric iron solution's band center was at 0.438 µm. Additionally, two absorption features occurred at 0.453 and 0.54 µm. The 0.453 µm feature was most pronounced in concentrations below 500 mg/L Fe^{3+}. Above 500 mg/L Fe^{3+}, this feature becomes a small inflection in the expanded envelope of the blue/green absorption band.

The spectrum of the lower concentration ferrous iron solutions strongly resembled the spectrum for DI water (Fig. 7b). Absorption features in the 50 mg/L Fe^{2+} solution curves were identical to those in the DI water curve, and subsequent concentrations exhibited increasing absorption only at the shortest wavelengths. A small inflection point at 0.48 µm appeared in the 600 mg/L Fe^{2+} solution and deepened

with increasing iron concentrations. In CR format, any absorption in the blue/green region was very minimal (Fig. 8b). At higher ferrous iron concentrations, although the absolute reflectance decreased in the blue-green, the CR process followed the contour of the original reflectance spectrum, so that there was no feature in the CR plot. At wavelengths 0.35 to 0.4 μm, the highest ferrous iron concentration solutions exhibited deeper band depths.

5. Discussion

   a. Water Chemistry

   Given the measured redox potential and pH values of the local AMD waters, the speciation of aqueous iron is illustrated in Fig. 9. Aqueous iron occurs chiefly in sulfate complexes ($FeSO_4^+$, $FeSO_4^0$) and insoluble iron as Fe^{3+} oxyhydroxide (goethite, α-FeOOH). In natural waters, ferric iron forms strong complexes with many ligands (Cl^-, SO_4^{2-}, $H_2PO_4^-$, F^-, HPO_4^{2-}, OH^-) (Langmuir 1997). Sulfate is by far the dominant anion present in the local AMD waters. The common solid products of AMD tend to be of small particle size; specifically ferrihydrite, schwertmannite, and goethite exist characteristically in particles <10 nm in size (Murad and Rojik 2005). Thus, it is plausible for colloidal size goethite to flow through the 0.45 μm pores in the filter membranes. Gammons et al. (2009) notes a common source of colorant in pit lake waters results from the oxidation of dissolved iron to hydrous ferric oxide (HFO), a red-brown substance that is very fine-grained and slow to settle by gravity. HFOs include ferrihydrite, lepidocrocite, limonite, and goethite. Therefore, it is reasonable to assume the speciation of iron in Leviathan's AMD waters occurs primarily as ferric iron complexed with sulfate anions, or colloidal goethite (HFOs).

   This speciation is consistent with the analytical data from Pond 2, however, the analytical data from the Pond 1 inlet shows iron is chiefly present in the reduced ferrous form. The old tunnel in which the AMD emanates at Leviathan was reported to extend 450 feet below the surface (Evans 1977). At that depth, the redox potential may be lower than at the surface discharge elevation, which would be consistent with the speciation of aqueous iron as ferrous iron. Throughout its journey from groundwater to surface water discharge, the AMD is slowly oxidizing as it reaches equilibrium with the atmosphere, so that water at the south end of Pond 1 (by the inlet pipe) is more reduced than the water on the north end of the Pond 1 and in Pond 2.

   b. Spectroscopy

      i. Local AMD Waters

Nearly all of the filtered samples have lower total reflectance than their unfiltered equivalents (Fig. 5). This is consistent with the Tyndall effect, which is the effect of light scattering by particles in a colloid or particles in a fine suspension (Brown et al. 2006). The filtered samples have lower total reflectance because there are fewer particles in suspension that will scatter light and increase reflectance leaving the water. The exception to this was the unfiltered Carson River sample, which was turbid enough to reverse the Tyndall effect through suspended sediments absorbing virtually all of the incoming light from the ASD's halogen probe.

There is very little difference in the spectral absorption features of filtered and unfiltered samples when analyzed in reflectance and CR formats. This suggests that the majority of the coloring agent in local AMD waters is an ion or a colloidal fraction less than 0.45 μm in size. It should be noted the local AMD waters have relatively low turbidity (1.5-11 NTU). It is not surprising that the spectral responses of these waters are not predominately caused by larger suspended particles.

ii.   Synthetic AMD Solutions

In this study, all ferric iron influenced waters are characterized by a rapid decrease in reflectance at shorter wavelengths. Additional absorption bands centered at 0.453 and 0.54 μm occur. As noted in the previous section, the most likely cause of color is ferric iron complexed with sulfates, or colloidal HFOs such as ferrihydrite, lepidocrocite, limonite, and goethite. Absorption spectra of ferric oxide and sulfate minerals have been presented by a number of previous studies (e.g. Sherman and Waite 1985; Crowley et al. 2003, 2006; Cloutis et al. 2006). Ferric iron in minerals has a number of electronic absorption features related to charge transfer between the ferric cation and associated oxygen anions, the strong absorption edge may also be due to magnetic coupling of ferric ions (Sherman and Waite 1985). In minerals, the crystallography will impart mineral-specific absorption features due to the distortion of the electronic configuration of the iron cation by the crystal structure and surrounding atoms. For iron complexed with sulfates or hydrous oxides in solution, crystal field transitions are not expected, but the absorption features of the synthetic AMD solutions are similar to that seen in ferric oxides and sulfates, and are attributed to ligand field and ligand-metal charge transfer transitions. These absorption bands occur near 0.360-0.80, 0.430, and 0.485-0.550 μm (Sherman and Waite 1985), which is consistent with the 0.453 and 0.54 μm absorption bands identified in the study's water spectra.

The CR spectra show a consistent correlation between ferric iron concentration in solution and VSWIR diagnostic features. The depth and extent of the absorption features in the region between 0.35 and 0.625 μm may provide a reliable approximation of ferric iron concentration in aqueous solutions (Fig. 8a). In order to quantify the depth of the absorption band due to ferric iron, the integrals of the CR curves were calculated for synthetic AMD solutions in the wavelength range 0.35 to 0.625 μm. When the integral

values are plotted against their respective iron concentrations, a calibration curve with an r-squared value of 0.96 is produced (Fig. 10). The ferric iron concentration (x) may be estimated using the equation $x = e^{(y + 0.38)/0.1063}$, where y equals the integrated band depth between 0.35 and 0.625 μm (sum of CR values between 0.35 and 0.625, divided by 0.275).

Ferrous iron impacts the spectral reflectance by absorbing wavelengths below 0.6 μm, but CR reflectance does not quantify ferrous iron's contribution effectively. At wavelengths 0.35 to 0.4 μm, the band depth of absorption generally correlates with ferrous iron concentrations (Fig. 8b). However, this is an extremely noisy region in the ASD spectrometer's range and is challenging to examine in detail. The depth of this absorption band is also extremely shallow compared to the band depths caused by ferric iron (Fig. 8a-b). Additionally, it may be very difficult to confidently identify spectral absorption features specifically owing to ferrous iron in environmental samples when ferric ion exhibits more robust features in the same wavelength region.

      iii.   Correlation of Local and Synthetic Waters

All local AMD water CR curves plot agreeably within the range established by the synthetic AMD solution CR curves (Fig. 11). Over the course of this study, the concentration of ferric iron at the Pond 1 inlet fluctuated between 30 and 70 mg/L Fe^{3+}, whereas the concentration of Pond 2 fluctuated between 280 to 2200 mg/L Fe^{3+}. Pond 1 represents freshly discharge AMD, while Pond 2 represents a more evapo-concentrated version of AMD. This variation is distinguishable in the VSWIR spectral response of local AMD waters. The concentration of ferric iron can be approximated using the synthetic AMD curves as contour lines (Fig. 11). The Pond 1 inlet curves consistently plot closer to the 50-300 mg/L Fe^{3+} contour lines, while the Pond 2 curves plot closer to high concentration contour lines.

This method appears to be most accurate for lower ferric iron concentrations. The local AMD waters with concentrations below 500 mg/L Fe^{3+} plot closer to their respective synthetic AMD contour lines. The local AMD sample with over 2000 mg/L Fe^{3+} has the most error, i.e. greatly over estimating iron concentration.

There is a problematic dynamic when measuring iron by VSWIR reflectance if the majority of iron is in the reduced form. Ferrous iron lacks diagnostic VSWIR features that are easily measured using basic spectral reflectance analysis techniques. The methods described in this paper may be limited to only highly oxidized AMD waters.

Mine waters are highly variable in their composition and may be dominated by numerous dissolved constituents and thermodynamic conditions depending on the geologic environment in which they originate (Lottermoser 2003). The methods described in this paper may not be suitable for all AMD

waters. Similar to optical studies of natural water bodies, the inherent and apparent optical properties of AMD waters are influenced by a range of physical, biological and chemical processes, which may interfere with accurate estimation of constituents based on spectral signatures. We recommend this method for aqueous ferric iron concentration estimation be restricted to mine waters that are acidic (pH range 2-6) due to the oxidation of iron rich sulfides, commonly found at base metal, gold, and coal mines. Highly turbid waters should be filtered or allowed to settle before employing this method. If the water volume is too turbid for light to effectively penetrate the column, the resulting spectrum should not be examined for ferric iron concentration.

7. Conclusions

The spectral response of ferric iron dominated AMD waters in the VSWIR region is unique. Compared with non-iron rich impaired water, turbid river water, and DI water, the AMD from Leviathan Mine possessed distinct characteristics that may be used for diagnostic identification. Specifically, the region between 0.35 and 0.625 μm may be used to approximately quantify ferric iron concentration. This method may be best suited for mine waters that are acidic, high in sulfate, and low in turbidity. Ferric iron concentration is a useful value which may imply other parameters such as pH, Eh, and general water quality. Subtle changes in ferric iron concentration due to environmental and seasonal conditions at Leviathan Mine were identified using VSWIR spectroscopy alone. These findings suggest subtle changes in mine water quality may also be identified qualitatively and quantitatively via remote spectroscopy.

Acknowledgements:
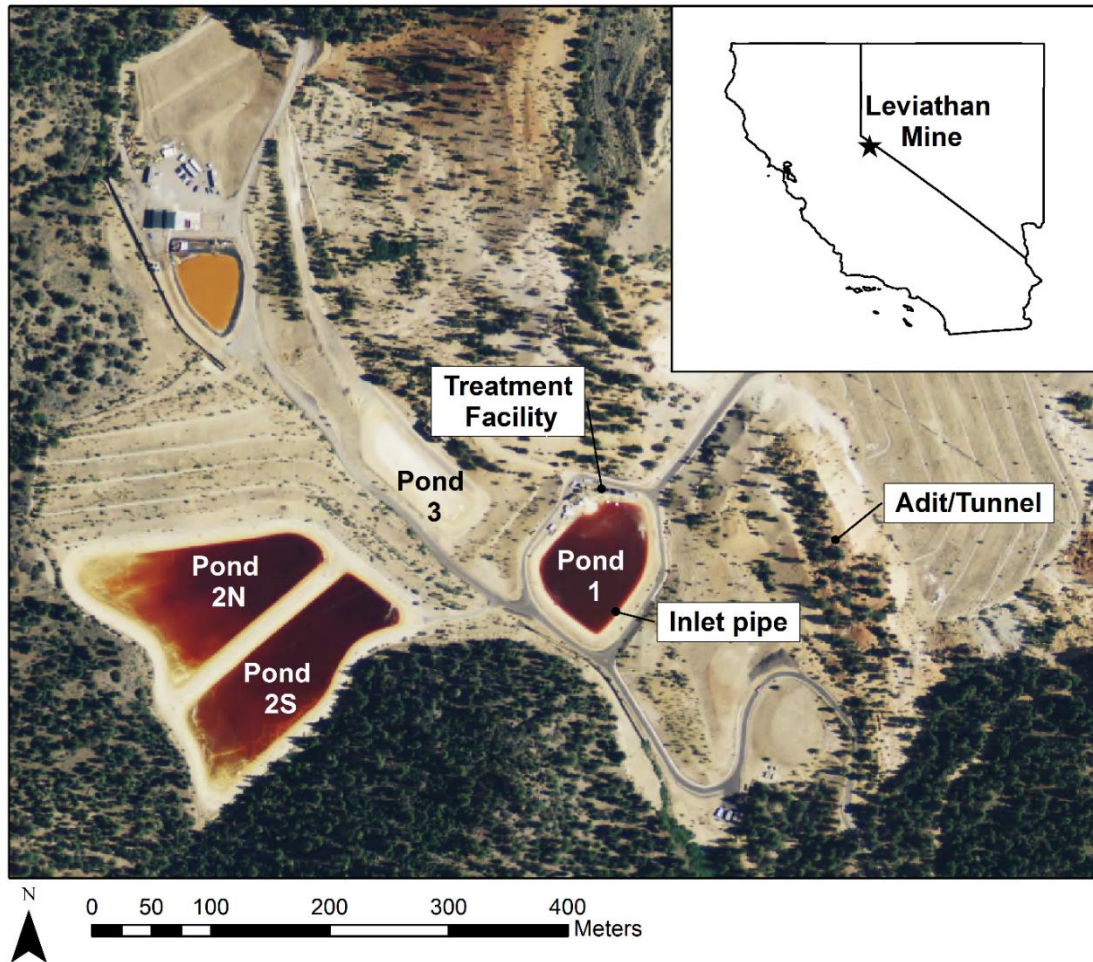
8. Figures and Tables

Fig. 1 Leviathan Mine is located in Alpine County, California, 10 miles east of Markleeville and 2 miles north of the Monitor Pass Highway (Sections 15 and 22, Township 10N, Range 21E)

Fig. 2 Leviathan Mine: a) From the south shore of Pond 1 looking north. Inlet pipe is along shoreline. Water treatment facility in background. Photo taken by author on 05/22/2014. b) From east shore of Pond 2 South looking west. Photo taken by author on 04/24/2014
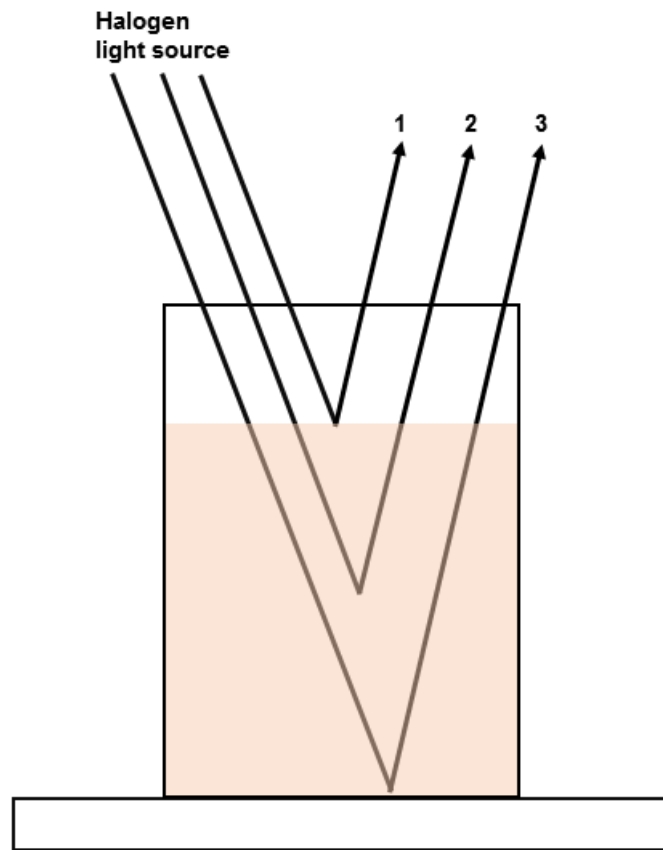
Fig. 3 Schematic of beaker solution and reflected light path. Halogen light source was from the ASD spectrometer probe attachment. 1) Spectral reflectance from water surface. 2) Volumetric scattering and reflectance. 3) Bottom reflectance from halon plate. Not drawn to scale

Table 1. SEM Inc. Water Quality Data Sampled 05/22/14				
Parameter	Units	Pond 1 (near the inlet)	Pond 2S	Pond 3
pH (lab)	pH	2.84	2.64	3.76
pH (field)	pH	2.65	2.59	3.72
Temperature (lab)	℃	18.5	19.3	18.7
Temperature (field)	℃	18.2	15.4	20.3
Redox Potential (Eh)	mV	663	721	621
Total Dissolved Solids	mg/L	5100	4800	6800
Turbidity	NTU	1.5	3.7	19
Alkalinity, Total	mg/L CaCO$_3$	<2	<2	<2
Alkalitnity/Bicarbonate	mg/L CaCO$_3$	<2	<2	<2
Alkalinity/Carbonate	mg/L CaCO$_3$	<2	<2	<2
Alkalinity/Hydroxide	mg/L CaCO$_3$	<2	<2	<2
Aluminum	mg/L	270	280	190
Antimony	mg/L	<0.002	<0.002	<0.002
Arsenic	mg/L	4.6	2.1	0.02
Barium	mg/L	0.006	0.002	0.008
Beryllium	mg/L	0.01	0.01	0.01
Boron	mg/L	0.11	0.1	0.31
Cadmium	mg/L	0.023	0.029	0.11
Calcium	mg/L	140	160	310
Chloride	mg/L	8	9	13
Chromium	mg/L	0.56	0.57	0.048
Cobalt	mg/L	1.4	1.4	4.2
Copper	mg/L	0.72	1.3	1.1
Ferric Iron	mg/L	70	280	<1
Ferrous Iron	mg/L	390	32	8
Fluoride	mg/L	6	6	10
Iron (total)	mg/L	460	310	7.4
Lead	mg/L	<0.002	<0.002	<0.002
Magnesium	mg/L	38	39	650
Manganese	mg/L	9.1	8.8	24
Mercury	mg/L	<0.0001	<0.0001	<0.0001
Nickel	mg/L	4	4.9	9.2
Nitrate	mg/L N	0.22	<0.05	1.2
Phosphorus Total	mg/L	3.2	1.7	0.07
Potassium	mg/L	7.5	0.53	<0.5

Selenium	mg/L	<0.01	<0.01	<0.01
Silica	mg/L SiO_2	84	79	42
Silver	mg/L	<0.002	<0.002	<0.002
Sodium	mg/L	28	14	30
Sulfate	mg/L	3300	3200	4800
Thallium	mg/L	0.15	0.008	0.024
Zinc	mg/L	0.72	0.72	2.3

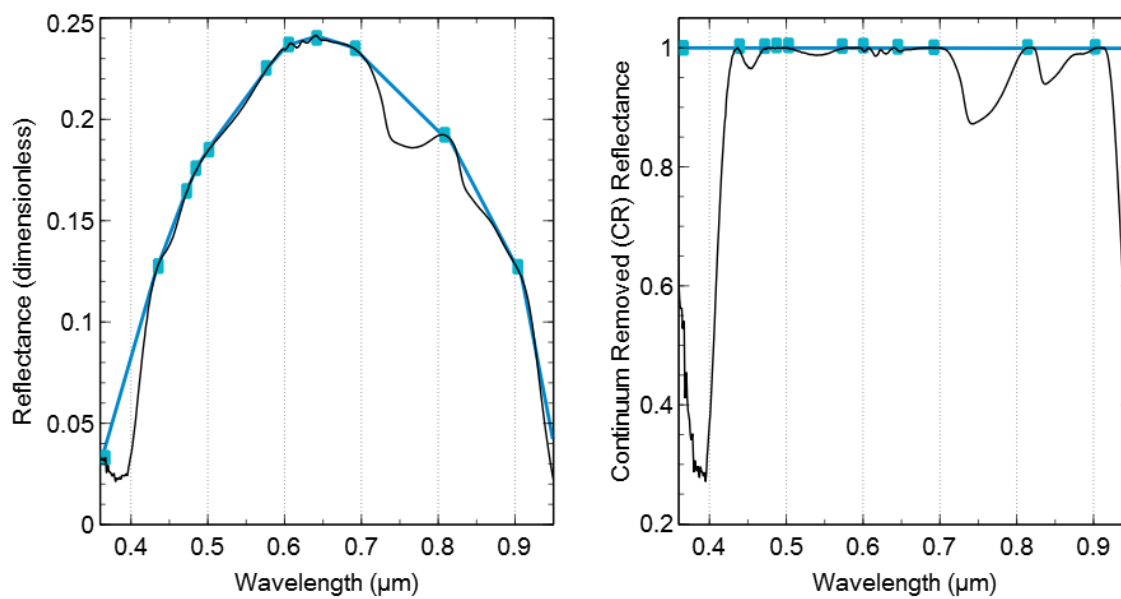| **Table 2.** SEM Inc. Water Quality Data Sampled 10/09/14				
Parameter	Units	Pond 1 (at the inlet)	Pond 1 (North Shore)	Pond 2N
Ferric Iron	mg/L	30		2200
Ferrous Iron	mg/L	500		15
Total Iron	mg/L	530		2215
pH (lab)	pH	3.09		2.31
pH (field)	pH	2.97	2.78	2.23
Temperature (lab)	℃	21.2		21.2
Temperature (field)	℃	18.1	17.4	22.2
Redox Potential (Eh)	mV	619		794
TDS	mg/L	3700		33000
Turbidity	NTU	11		2.4

Fig. 4 Plot demonstrating Continuum Removal (CR) method. Straight-line segments denote the continuum. CR reflectance = source spectrum / continuum spectrum. Example source spectrum is 200 mg/L Fe^{3+} solution
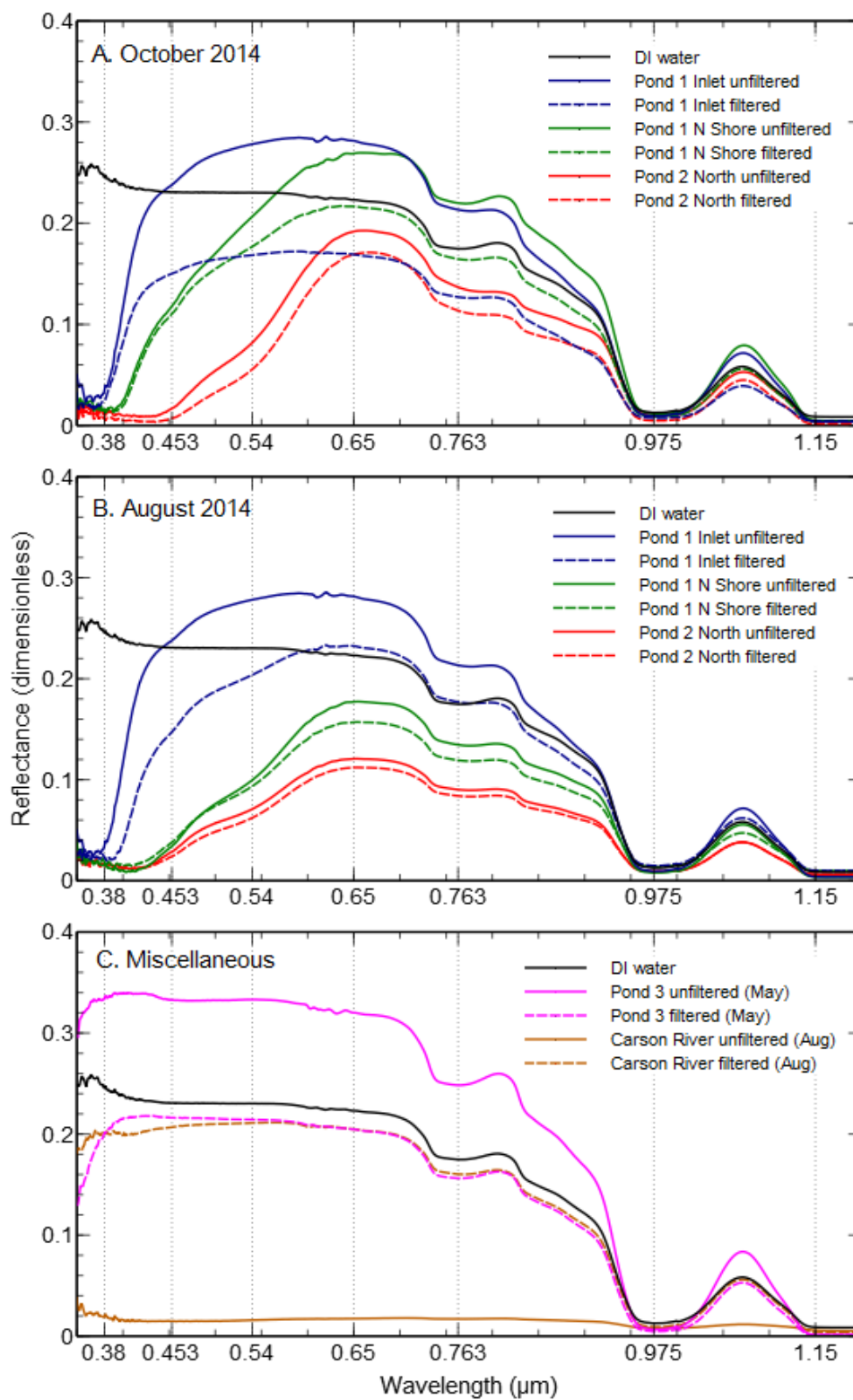
Fig. 5 Unfiltered samples are solid lines and filtered samples are dashed lines. Gridlines are placed at 0.38, 0.453, 0.54, 0.65, 0.763, 0.975 and 1.15 μm
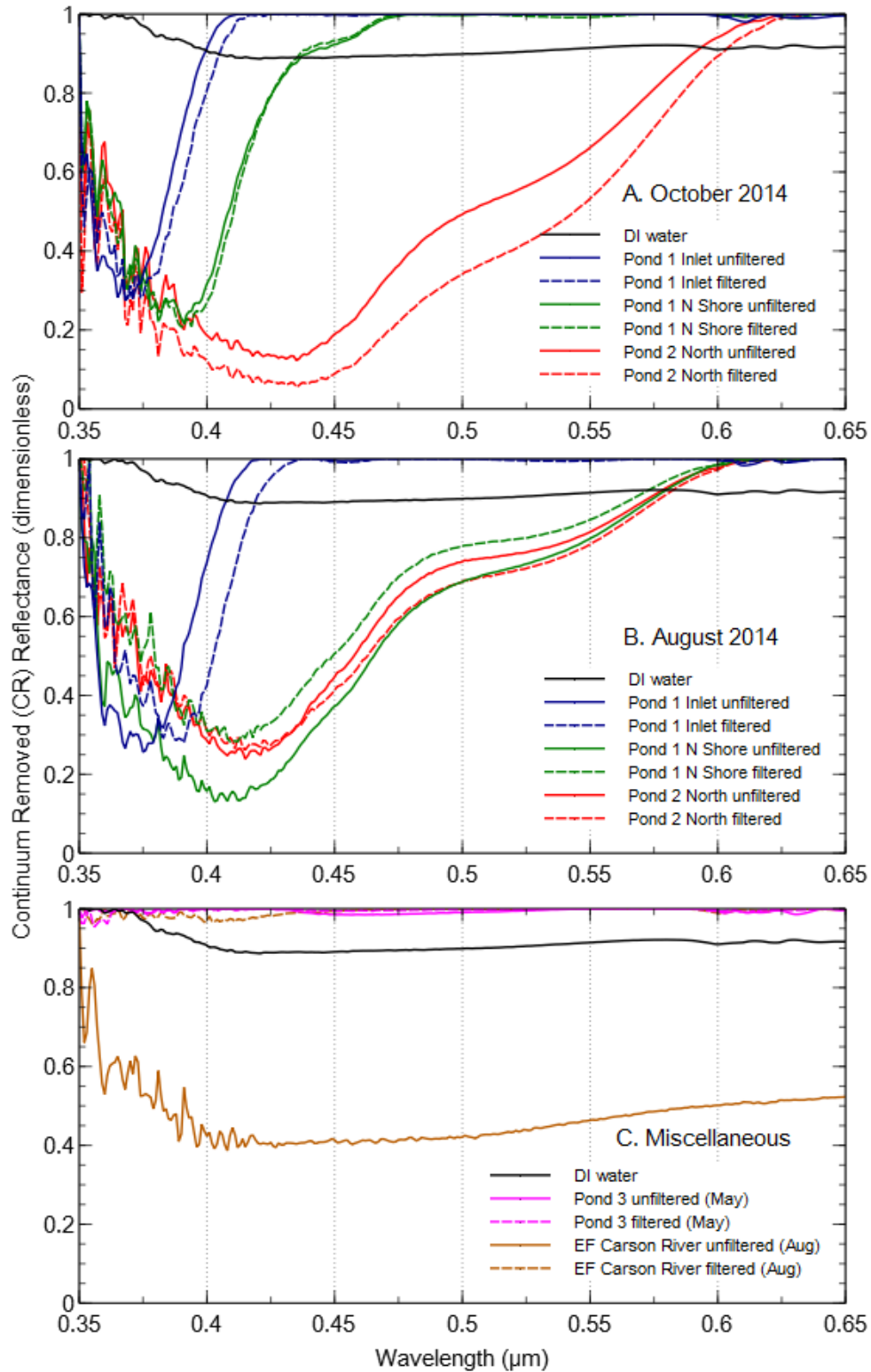
Fig. 6 Unfiltered samples are solid lines and filtered samples are dashed lines
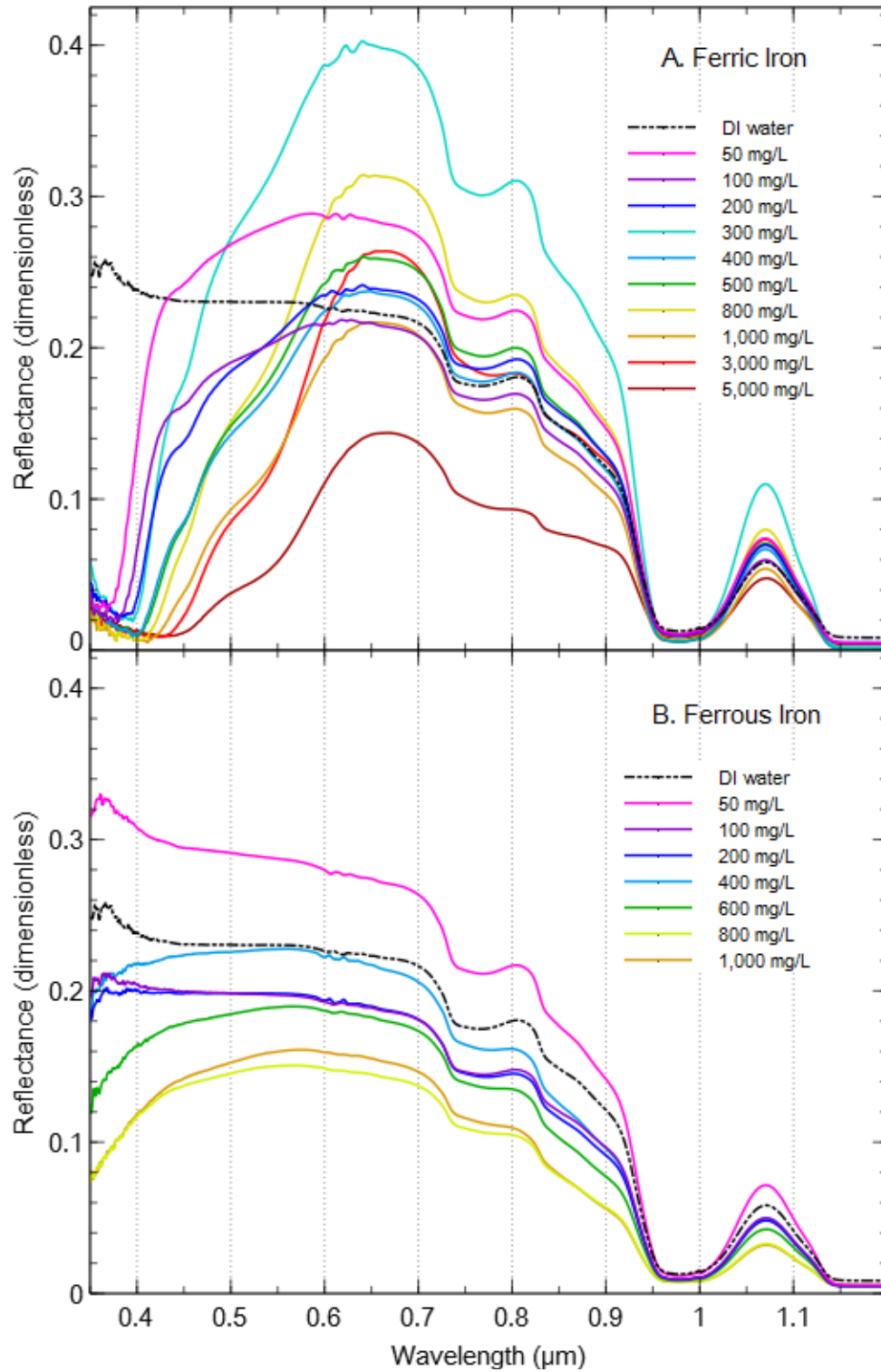
Fig. 7 Synthetic lab solutions demonstrating the spectral effect of a.) ferric and b.) ferrous iron in incrementing concentrations
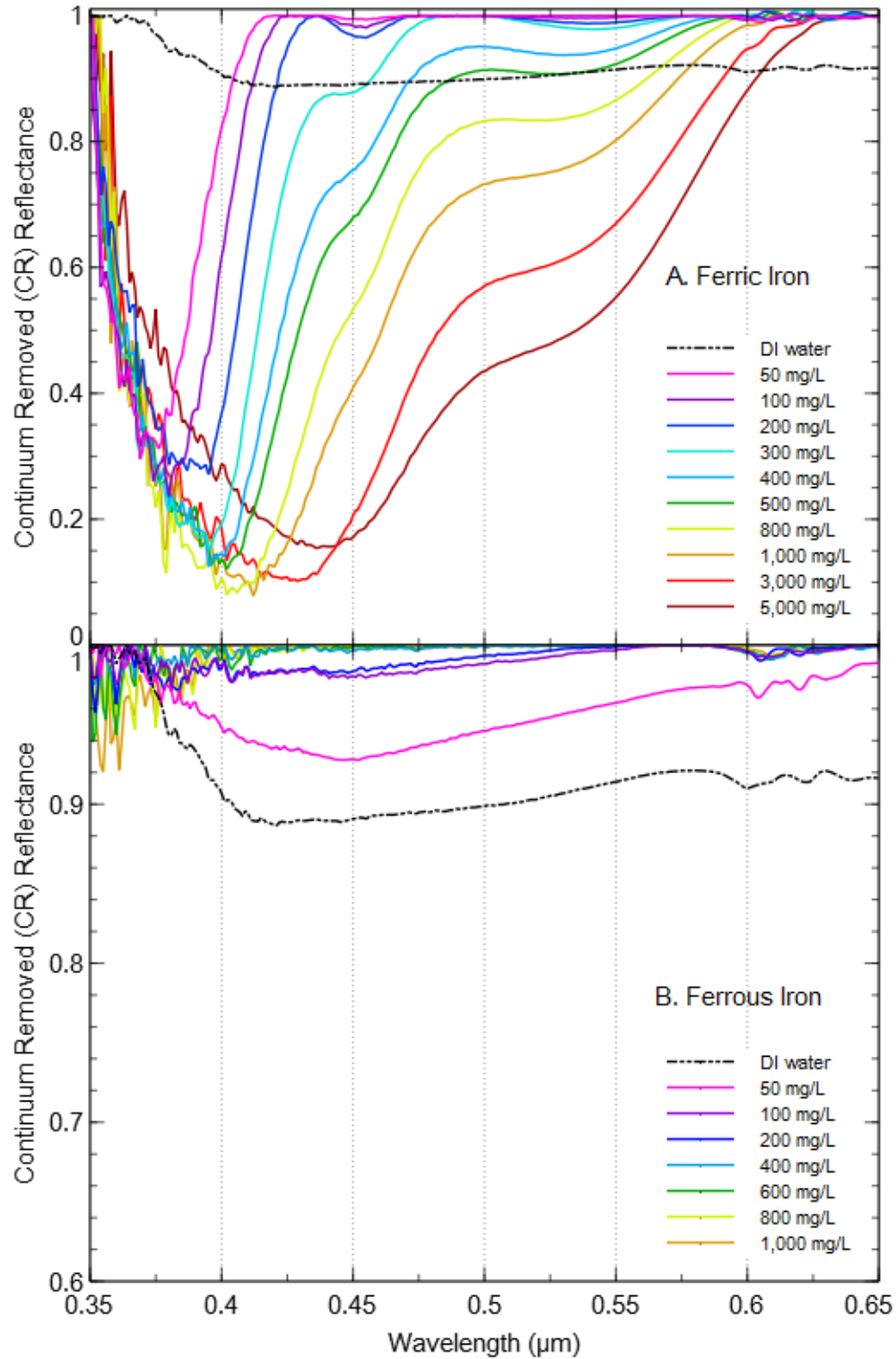
Fig. 8 Synthetic lab solutions demonstrating the spectral effect of a.) ferric and
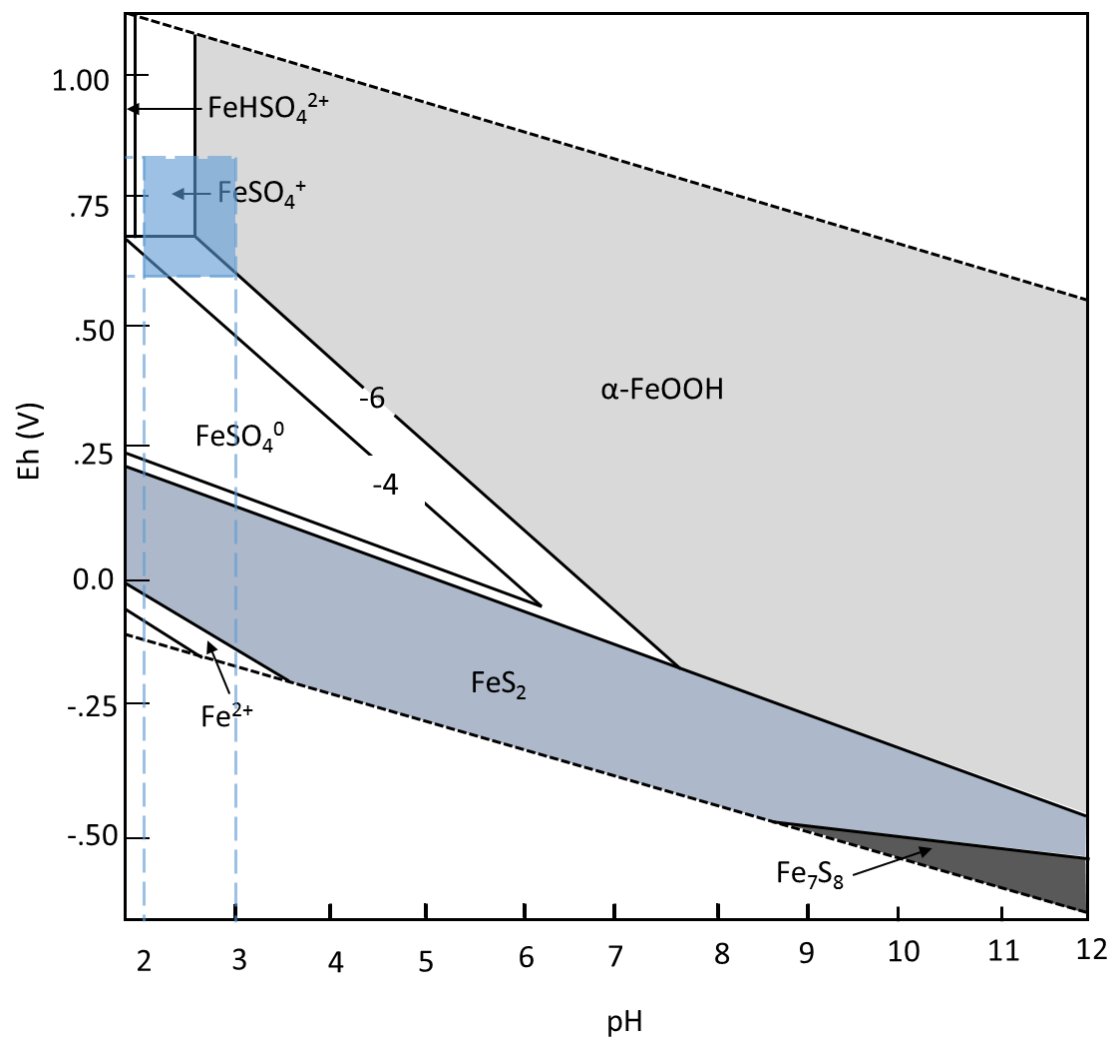b.) ferrous iron in incrementing concentrations, in continuum removed mode

Fig. 9 Eh-pH diagram for the system Fe-O$_2$-S-H$_2$O at 25 ℃, showing stability fields of goethite (α-FeOOH), pyrite (FeS$_2$), and monoclinic pyrrhotite (Fe$_7$S$_8$) for ΣS(aq) = 10^{-2} mol/kg, and total carbonate 10^{-4} mol/kg. ΣFe(aq) = 10^{-6} and 10^{-4} mol/kg at aqueous/solid boundaries. The blue shaded box shows that dissolved iron occurs chiefly in sulfate complexes given the pH and Eh range. Adapted from Barnes and Langmuir (1979)

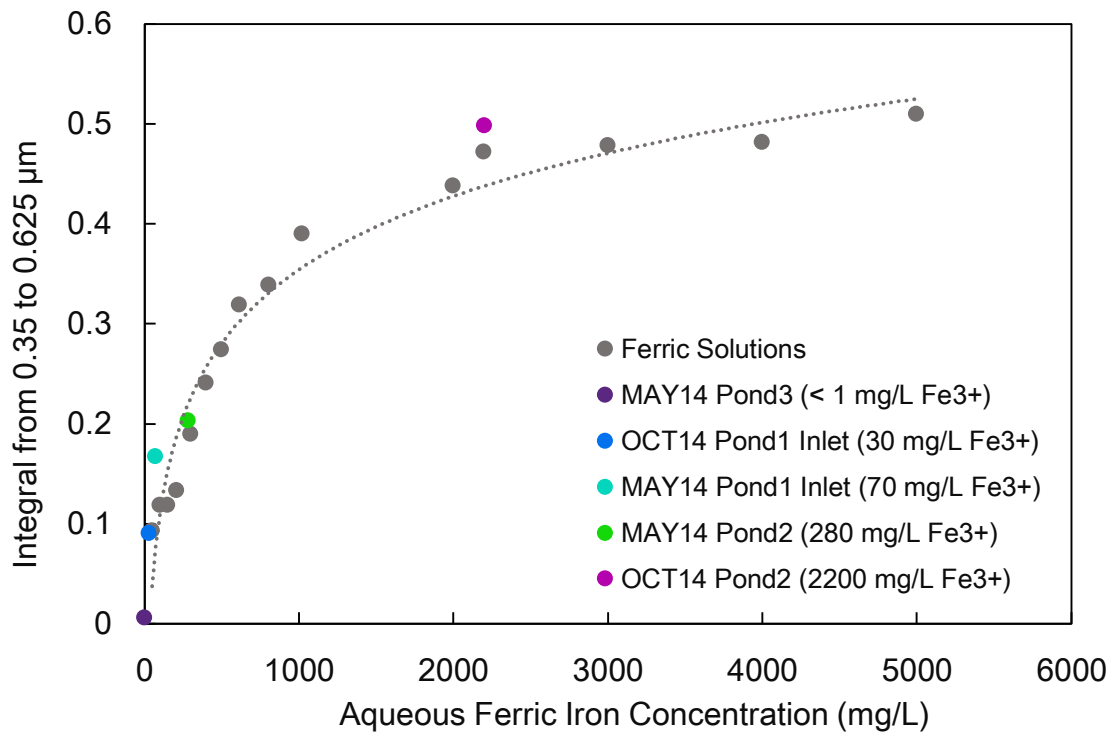**Fig. 10** Plot of Fe^{3+} concentration vs $\int_{0.350}^{0.625} CR\ Reflectance\ dx$. AMD sample points (colored) are unfiltered and have known Fe^{3+} concentration from SEM Inc. analysis. Synthetic AMD solutions (gray) from laboratory experiment. Trend line equation y = 0.1063ln(x)-0.38 and R^2 = 0.9618. The calibration curve is pH dependent (pH range 3-1.7)
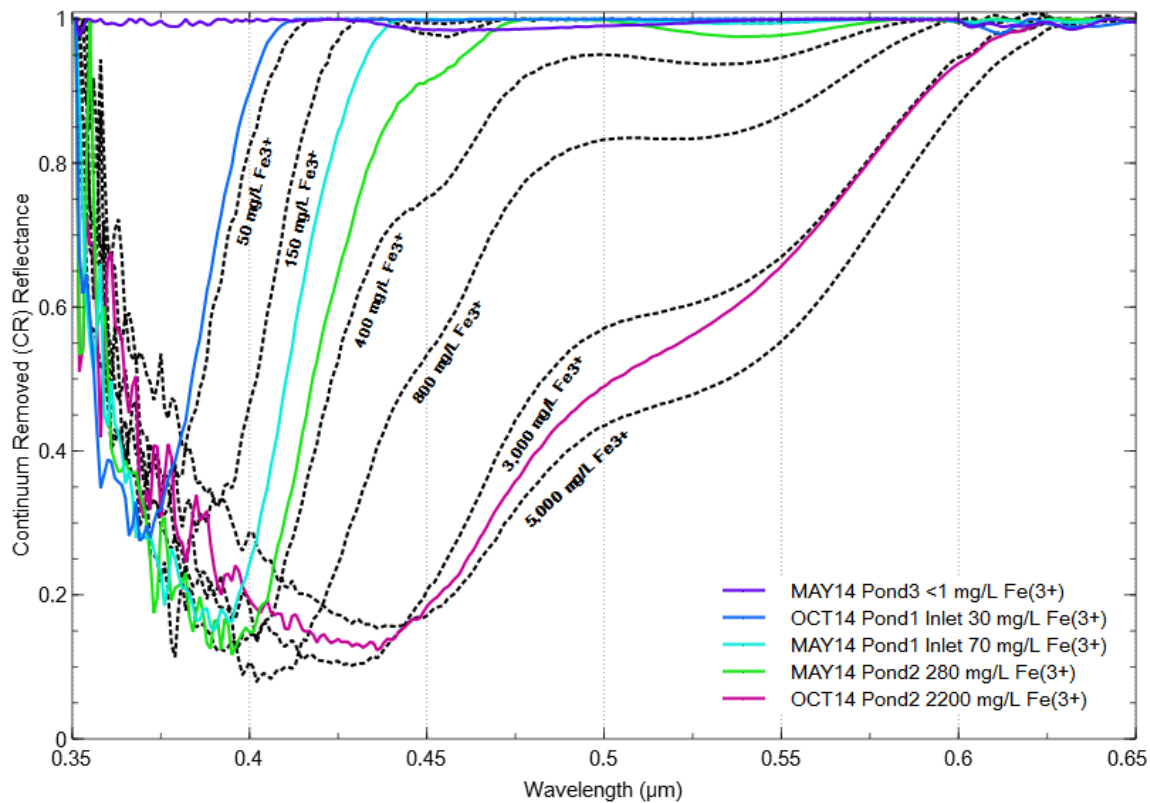
Fig. 11 Colored plots are local AMD samples with known Fe concentration (from SEM Inc. analysis). Local AMD samples are unfiltered. Dotted contour plots are from synthetic AMD solutions

9. References

Brown TL, LeMay HE, Bursten BE, Murphy CJ (2006) Ch.13 Properties of solutions. In: Chemistry: The central science 10th ed. Prentice-Hall, Upper Saddle River, New Jersey, pp 559

Burns RG (1993) Origin of electronic spectra of minerals in the visible to near-infrared region. In: Remote geochemical analysis: elemental and mineralogic composition. Cambridge Univ. Press, New York, pp 3–29

Castendyk DN, Eary LE (2009) Ch.1 The nature and global distribution of pit lakes. In: Mine pit lakes - characteristics, predictive modeling, and sustainability, vol 3. Society for mining, metallurgy, and exploration, Inc. (SME), electronic edition, pp 1-11

California Regional Water Quality Control Board, Lahontan Region (2015) Year-end report for the 2014 field season at Leviathan Mine. http://www.swrcb.ca.gov/lahontan/water_issues/projects/leviathan_project/docs/lev2014rpt.pdf. Accessed 20 August 20 2015

Clark RN, Roush TL (1984) Reflectance spectroscopy: Quantitative analysis techniques for remote sensing applications. Journal of Geophysical Research 89: B7: 6329-6340 doi:10.1029/JB089iB07p06329

Cloutis EA, Hawthorne FC, Mertzman SA, Krenn K, Craig MA, Marcino D, Methot M, Strong J, Mustard JF, Blaney DL, Bell JF, Vilas F (2006) Detection and discrimination of sulfate minerals using reflectance spectroscopy. Icarus, 184: 1: 121-157. doi:10.1016/j.icarus.2006.04.003

Crowley JK, Williams DE, Hammarstrom JM, Piatak N, Chou IM, Mars JC (2003) Spectral reflectance properties (0.4-2.5 μm) of secondary Fe-oxide, Fe-hydroxide, and Fe-sulphate-hydrate minerals associated with sulphide-bearing mine wastes. Geochemistry: Exploration, Environment, Analysis 3: 3: 219-228. doi:10.1144/1467-7873/03-001

Crowley JK, Williams DE, Hammarstrom JM, Piatak N, Mars JC, Chou IM (2006) Spectral reflectance properties (0.4-2.5 um) of secondary Fe-oxide, Fe-hydroxide, and Fe-sulfate-hydrate minerals associated with sulfide-bearing mine waste. USGS Open File Report Rep. 2003-196

Dozier J, Painter TH (2004) Multispectral and hyperspectral remote sensing of alpine snow properties. Annual review of earth and planetary sciences 32: 465-494. doi:10.1146/annurev.earth.32.101802.120404

Duaime TE, Tucci NJ (2009) Butte mine flooding operable unit water-level monitoring and water-quality sampling, 2008 consent decree update. Montana bureau of mines and geology, open file report no. 589 pp 95

Evans JR (1977) Zaca mine and Leviathan mine. In: Mines and mineral resources of alpine county, California, county report 8. California division of mines and geology pp 22–27

Gammons CH, Harris LN, Castro LM, Cott PA, Hanna BW (2009) Creating lakes from open pit mines: process and considerations, with emphasis on northern environments. Canadian technical report of fisheries and aquatic sciences 2826

Green RO, Painter TH, Roberts DA, Dozier J (2006) Measuring the expressed abundance of the three phases of water with an imaging spectrometer over melting snow. Water Resources Research 42: 10. doi:10.1029/2005wr004509

Hunt GR, Ashley RP (1979) Spectra of altered rocks in the visible and near infrared. Economic Geology 74: 1613-1629. doi:10.2113/gsecongeo.74.7.1613

Kruse FA, Lefkoff AB (1993) Knowledge-based geologic mapping with imaging spectrometers. Remote Sensing Reviews, special issue on NASA Innovative Research Program (IRP) results 8: 3-28. doi:10.1080/02757259309532188

Langmuir D (1997) Ch.12 Iron and sulfur geochemistry. In: Aqueous environmental geochemistry. Prentice-Hall, Upper Saddle River, New Jersey, pp 431-474

Lottermoser BG (2003) Ch.3 Mine water. In: Mine wastes. Springer, New York, pp 83-141

McCullough CD, Müller M, Eulitz K, Lund MA (2011) Modelling a pit lake district to plan for abstraction regime changes. In: Mine closure 2011, Alberta, Canada conference proceedings, pp 581-592

Murad E, Rojik P (2005) Iron mineralogy of mine-drainage precipitates as environmental indicators: review of current concepts and a case study from the Sokolov Basin, Czech Republic. Clay Minerals40: 427-440. doi:10.1180/0009855054040181

Peichang S, Cheng S, Smith S (2004) Acid lake identification using GIS and remote sensing. In: Geological Society of America, Denver annual meeting, Nov 7-10

Sanliyuksel D, Yucel MA, Baba A (2014) Change detection and visualization of acid mine lakes using time series satellite image data in geographic information systems (GIS): Can (Canakkale) County, NW Turkey. Environ Earth Sci 72: 4311-4323. doi:10.1007/s12665-014-3330-6

Shevenell LA (2000) Water quality in pit lakes in disseminated gold deposits compared to two natural, terminal lakes in Nevada. Environmental Geology 36: 7: 807-815. doi:10.1007/s002540050497

Vandersluis GD, Straskraba V, Effner SA (1995) Hydrogeological and Geochemical Aspects of Lakes Forming in Abandoned Open Pit Mines. In: proceedings of Water Resources at Risk. IMWA-162-IMWA-177

Chapter 2—Manuscript for submission to Remote Sensing of Environment

Title: Using multi-season airborne hyperspectral imagery to examine mine affected water bodies.

Authors: Gwendolyn Davies, Wendy Calvin

Abstract

1. Introduction
2. Study Area—Leviathan Mine
3. Dataset
4. Methods
    a. Field Data
    b. Water Remote Sensing
5. Results
    a. Water Chemistry and Environmental Conditions
    b. Water Spectroscopy
6. Discussion
7. Conclusions
8. Figures
9. Reference

Abstract:

The water quality of pit lakes is one of the largest environmental issues facing the global mining industry. Pit lakes are often located across large geographic expanses and are difficult to access. With continuing advancement of imaging satellites, hyperspectral remote sensing may provide a useful monitoring tool for identifying pit water quality across vast regions. Visible to shortwave infrared hyperspectral remote sensing has been widely used to monitor acid mine drainage mineralogy. In comparison, very few studies have examined the spectral signatures of mine-affected waters and open pit lakes from a remote platform. This study used seasonal hyperspectral imagery (AVIRIS) to examine the spectral signatures of acidic mine water in large retention ponds at the Leviathan Mine Superfund site, California. Spectral curves of acidic water were characterized by shifted peak reflectance to red wavelengths and high overall reflectance. These absorption features correlated to those seen in laboratory spectral studies of synthetic mine water solutions, and were attributed to elevated aqueous ferric iron concentration. Shifted peak reflectance and high overall reflectance may be used for first order diagnostic criteria of poor pit lake water quality. Similar to natural waters, the spectral signatures of mine waters were strongly influenced by environmental factors including bottom reflectance, turbidity, biomass, and seasonality. This prohibited the direct comparison of airborne spectral curves to laboratory spectral studies for quantification of aqueous ferric iron concentration. However, results show that high spectral resolution imagery may have the capability to identify fluctuations in aqueous ferric iron concentration in water bodies—an application that would be beneficial in environmental monitoring of pit lake water quality.

1. Introduction

Over the past few decades, advances in modern mining and processing techniques have made it feasible and economical to pursue large open pit mining (Shevenell 1999). As a result, the number of open pit mine operations has increased relative to underground mining (Castendyk and Eary 2009). These operations commonly extract ore from below the water table and remove large volumes of water to maintain dry operating conditions. Once mining is complete and dewatering ceases, pits fill in with water to the pre-mining groundwater level. Depending on the acid producing potential of the surrounding geologic material, this water may not meet water quality standards. Sites with poor water quality have the potential to degrade surrounding water resources and affect ecosystem and human health (Castendyk and Eary 2009). By 2025, almost 50 open pit mines, which intercept the groundwater table, will be completed in the United States (Vandersluis 1995). In the state of Nevada alone, over 35 mines currently have a lake filling in their open pits (Shevenell 1999). When filled, it is estimated that these pit lakes will contain more water than all of the manmade reservoirs within the borders of Nevada, excluding Lake Mead (Miller 2002). Monitoring these mining features as they change with time will be an important task, particularly for Nevada. An extreme example of the potential legacy of open pit mines is demonstrated at the Berkley Pit Lake in Montana, where over 1.5×10^8 liters (3.9×10^7 gallons) of AMD have accumulated in the old open pit, and sit directly adjacent to a town of 34000 people.

Hyperspectral remote sensing (200 or more spectral bands) has been widely used to characterize mine waste environments, focusing on surface minerals associated with acid mine drainage (AMD) (Swayze et al. 2000; Montero et al. 2005; Riaza et al. 2012a; Kopachova 2014). These studies typically assign "high" and "low" priority contamination zones to mine waste surfaces based on the zonation of surface mineralogy. In comparison, very few studies have specifically examined the spectral signatures of mine-affected waters in rivers and streams or in mining pit lakes. The spectral response of these waters could provide valuable information about water quality.

In order to properly identify the distinct spectral properties of mine waters, one must understand the spectral properties of natural waters. Diffuse spectral reflectance from inland waters is influenced by the interaction of several factors, including atmospheric scattering, roughness of the water surface, volume reflection within the water column, and in some instances, bottom reflection (Campbell and Wynne 2011). As light strikes the surface of a water body a small percentage of the incident light is reflected back into the atmosphere, and the remaining is refracted into the water column. Light entering the water body may be scattered or absorbed by the water molecule itself, or by suspended constituents. These constituents include water quality parameters such as chlorophyll-*a* (chl-a), suspended minerals, and colored dissolved organic matter (Bukata et al. 1995). Incident light may also be reflected from the bottom surface in shallower waters. Low concentrations of most other minor compounds in surface waters produce negligible absorption and scattering impacts in reflectance spectra (by comparison with the concentrations of water

quality parameters mentioned above) (Bukata et al. 1995; Jerlov 1976). Mine affected waters, however, typically have significantly elevated concentrations of trace metals and dissolved inorganic salts—orders of magnitude greater than natural marine and inland waters. Mine affected waters are characterized by exceptionally high sulfate (>1000 mg/L), high iron and aluminum (>100 mg/L), and elevated copper, chromium, nickel, lead, and zinc concentrations (>10 mg/L) (Lottermoser 2003). These elevated concentrations very likely impact the spectral response of mine waters.

Identification of acidic water with remote sensing could be a useful tool in environmental monitoring, but research on this topic has been inadequate. Riaza et al. (2012b; 2015) identified specific absorption features in mine affected river water with varying pH using hyperspectral imagery (HyMap), however, the authors' interpretation of spectral differences due to water composition are not well supported. Direct spectral comparison between airborne and field spectral data are either nonexistent or contradictory. Spectra in these studies appear to be greatly influenced by bottom reflectance and vegetation. Without knowledge of sediment load, channel depth, and chl-a concentration, these data are ineffective for spectral based water quality analysis. Several studies have examined the spectral responses of mine-affected waters as they would occur in large open pit lakes or treatment ponds (Schroeter and Gläßer 2011; Gläßer et al. 2011; Riaza et al. 2012a). Schroeter and Gläßer (2011) compared multispectral imagery (Landsat TM) and water quality parameters in lignite mining lakes of Eastern Germany using multivariate statistical cluster analysis. Authors found a correlation between TM3 band (630 to 690 nm) and iron concentration as well as a correlation between high suspended matter. Gläßer et al. (2011) used hyperspectral imagery (Cessna 207T) to examine the same study area, and more detailed spectral curves of mining lakes were used to estimate water pH. Riaza et al. (2012a) identified spectral differences in mine ponds with different water chemistry. Again, this study lacked both identification of bottom reflectance contribution and water chemistry data to back up water composition classifications. These studies did, however, identify the influence of iron compounds on mine water spectral signatures. Similarly, Davies and Calvin (2015, in review) demonstrated the impact of ferric iron in the spectral response of synthetic and local AMD waters in a laboratory setting using a handheld spectrometer. The region between 350 and 625 nm was identified as a diagnostic region that may be used to approximate ferric iron concentration in mine waters.

There remain gaps in the field of hyperspectral remote sensing for mine water characterization. Furthermore, the water chemistry of mine water bodies may vary significantly depending on geologic and hydrologic conditions, resulting in potential for high diversity of mine water spectral signatures. With the accelerating rate of open pit lake formation in the western U.S., a better understanding of the spectral dynamics of mining-induced impaired water bodies and the development of mine water spectral libraries are needed. Hyperspectral remote sensing may provide a useful tool for rapidly and economically monitoring the water quality of pit lakes.

This study will explore the ability of multi-season airborne hyperspectral imagery to examine mine affected water surfaces at the Leviathan Mine Superfund site. Specifically, the goals are to:

1) Identify the unique spectral properties of mine affected waters as compared to natural water bodies,

2) Determine if water quality parameters (e.g. pH, iron concentration) can be approximated from remotely sensed imagery through comparison with laboratory spectral libraries, and

3) Identify the influence of other environmental factors (e.g. bottom reflectance, turbidity, biomass, seasonality) in the spectral signatures of mine affected waters.

2. Study Area—Leviathan Mine

Leviathan Mine is located in the Monitor Pass mining district in Alpine County, California (Sections 15 and 22, Township 10N, Range 21E). The Monitor Pass district is contained in andesitic and porphyry rocks from Pliocene intrusions and volcanic activity in the Eastern Sierra Nevada (Vikre and Henry 2011). The mine is about 2,134 m above sea level and receives about 53 cm of annual precipitation. In total, approximately 4.5×10^8 kg of pure sulfur were extracted from Leviathan Mine by open-pit mining from 1952-1962 (Evans 1977). At its largest extent the pit was about 600 meters long, 300 meters wide, and 125 meters deep (Evans 1977). About 2.0×10^{10} kg of overburden material containing significant quantities of low-grade sulfur ore were spread over 1 square km (CA Dept of Health Services 2003). The mine area is bordered by two small tributaries which historically traveled directly through the waste pile and spoil areas, ultimately feeding into the East Fork of the Upper Carson River. Prior to remediation efforts, the Bryant Creek drainage basin was largely impaired by AMD from Leviathan mine. Fish, insect, and livestock kills have been reported downstream of the mine (EPA 2006; CA Dept of Health Services 2003). Today, the site is a U.S. Superfund site on the National Priorities List. Leviathan creek has been channelized and no longer flows through the waste rock piles. AMD is managed through a series of evaporation ponds and an on-site water treatment facility.

The primary source of AMD emanates from discharging groundwater from a remnant tunnel and adit structure (California Regional Water Quality Control Board 2015). The water has an average pH of 2.6, >3200 mg/L SO_4^{2-}, 400 mg/L Fe, and 4 mg/L As (Davies and Calvin 2015, in review). Fresh AMD from the adit/tunnel is piped into the south end of Pond 1 (Fig. 1). Water is distributed between Pond 1, Pond 2 South, and Pond 2 North, which are interconnected and are at the same elevation. The ponds are lined with a geotextile fabric and packed with crushed rock from the site. As the AMD water oxidizes and accumulates in the ponds, it becomes strikingly red in color (Fig. 2). Excess water may be released down to Pond 3 for additional storage if necessary. During the time of this study Pond 3 was not used for AMD storage and only contained meteoric water. Together, these four ponds have a total surface area of about 36000 square meters. The maximum depth in Pond 2 North and South is about 1.7 meters, and about 2.1

meters in Pond 1. The actual depth of water will vary depending on the season and year's annual precipitation.

The ponds are typically at their fullest in late spring (as water has collected throughout the winter), then levels slowly decline as evaporation increases in the early summer. By mid-summer, the ponds are virtually empty after water is pumped through the treatment facility. AMD is neutralized in 10000-gallon fiberglass tanks by the addition of lime ($Ca(OH)_2$) and the resulting metal-rich waste is transferred to the sludge pond ("Pit Clarifier"), which is about 2100 square meters in area. After treatment, any surplus lime is dumped onto the north shore of Pond 1, which typically still contains a small volume of water.

Previous water analysis at this site has shown that evaporation and atmospheric exposure cause AMD in Pond 2 North and Pond 2 South to become more oxidized and more concentrated than AMD in Pond 1 (Davies and Calvin 2015, in review). In mid-summer, evapo-concentrated AMD in Ponds 2 may contain ferric iron concentrations nearly five times that of Pond 1 (280 to 2200 mg/L Fe^{3+}). Pond 1 maintains a more reduced redox potential and is more dilute, as it constantly receives AMD discharging directly from the adit.

3. Dataset

A total of seven images were examined in this study. The images were collected as part of the National Aeronautics and Space Administration (NASA) Hyperspectral Infrared Imager (HyspIRI) preparatory mission. The mission used NASA's Airborne Visible/Infrared Imaging Spectrometer (AVIRIS) flown on the ER-2 aircraft for a series of seasonal (spring, summer, fall) data collections over two years (2013-2014). Collection dates are summarized in Table 1. AVIRIS provided 204 spectral channels at 10 nm intervals across wavelengths 366 to 2496 nm, with a spatial resolution of 15 meters.

4. Methods
   a. Field Data

Field data was collected with the ASD FieldSpec Pro spectrometer with pistol grip option, which provided 2,151 spectral channels at 1 nm intervals across wavelengths 350 to 2500 nm. Field visits occurred about one to three weeks before or after the corresponding flight date, between 10/2013-11/2014. When standing water was present in the ponds, spectra of the center was taken from the pond's rim.

On field visits between 05/22/2014 and 09/16/2015 the field pH of pond water was measured with a Double Junction Waterproof pHTestr 20, calibrated using pH 4 and 7 buffer solutions. On two occasions, water was collected in HDPE bottles, stored on ice, and delivered to the SEM, Inc. laboratory (Reno, NV)

for basic chemical analysis. On 05/22/2014 water samples were analyzed for major anions/cations, trace elements, ferric/ferrous iron, TDS, pH, redox potential, and turbidity (Al, B, Ca, Fe, Mg, K, SiO_2, and Na by ICP-OES; Sb, As, Ba, Be, Cd, Cr, Co, Pb, Mn, Ni, Se, Ag, TI, and Zn by ICP-MS; Cl, F, NO_3, and SO_4 by Ion Chromatography; Hg by AA Cold Vapor). On 10/09/2014 water samples were analyzed for ferric/ferrous iron, TDS, pH, redox potential, and turbidity. Additionally, on 09/16/2015 water was sampled and analyzed for chlorophyll-a and pheophytin concentration at the University of Nevada, Reno Aquatic Ecosystem Laboratory (concentration by glass microfiber filtration, extraction by freezing, and measured by fluorometer).

Data Acquisition Date	Water level in Pond 1	Water level in Pond 2 North & Pond 2 South
05/02/2013	Full	Full
06/04/2013	Full	Full
09/19/2013	Low	Empty
04/10/2014	Full	Full
06/02/2014	Full	Full
09/09/2014	Very Low	Empty
11/17/2014	Low	Empty

Table 1 Imagery retrieval dates and corresponding pond water levels

b.   Water Remote Sensing

All image processing was completed using the Environment for Visualizing Images (ENVI) version 5.1 software package. The AVIRIS images were calibrated and corrected for atmospheric effects by the HypsIRI preparatory mission team at the Jet Propulsion Laboratory (JPL) in Pasadena, California.

Regions of Interest (ROIs) were collected over the center of Pond 1 in each seasonal image (seven images). ROIs were also collected over the deepest section of Pond 2 North and Pond 2 South in the spring images (four images). Each ROI contained about 10 to 25 pixels, with each pixel measuring 15 m by 15 m. Additionally, 13 ROIs from numerous water bodies within the HypsIRI preparatory mission dataset were collected. These water bodies included Lake Tahoe, Mono Lake, Topaz Lake, Heenan Lake, the Stanislaus River, and Yerington Pit Lake. Each of these additional ROIs contained about 25 to 100 pixels, again with each pixel measuring 15 m by 15 m. The additional ROIs were intended to showcase the large variation in spectral characteristics which occur in natural inland water bodies and provide comparison with one other mine-affected water body (Table 2). The Leviathan ponds were also examined on a pixel by pixel basis, moving from the center of the ponds, outward into shallower water, in order to identify the effect of bottom reflectance from the pond liner surface.

Due to the strong absorption of water at longer wavelengths, the wavelength region of greatest interest was 375-1000 nm. Spectral features were examined by comparing the reflectance, Continuum Removed (CR) reflectance (Kruse and Lefkoff 1993), and reflectance first derivatives.

Water Target	General Water Quality	Source
Heenan Lake	Good; large algal blooms in late summer	
Topaz Lake	Good; Chl-a = 80 µg/L	NDEP (2008)
Lake Tahoe	Very good; Chl-a < 1 µg/L	NDEP (2008)
Stanislaus River	Good; supports Chinook salmon migration	
Yerington Pit Lake	Poor; pH = 8.1, 0.01 mg/L Fe, 270 mg/L SO_4^{2-}, TDS = 631 mg/L, Chl-a = 0.12 µg/L	Hershey et al. (2010)
Mono Lake	Poor; TDS = 90,000 mg/L, 10,300 mg/L SO_4^{2-}, Chl-a = 1.65 µg/L	Javor (1999)
Leviathan	Poor; pH = 2.6, 400 mg/L Fe, 3,200 mg/L SO_4^{2-}, TDS = 6,000 mg/L	Davies and Calvin (2015, in review), CA Regional Water Quality Control Board

Table 2 Imagery retrieval dates and corresponding pond water levels

5. Results

    a.   Water Chemistry and Environmental Conditions

Annual precipitation in 2013 and 2014 was 42.9 and 41.4 cm, respectively (NRCS, Monitor Pass SNOTEL). This was about 13 cm below the average annual precipitation for the past 25 years. AMD treatment dates and volumes are listed in Table 3. Generally, pond water pH did not vary significantly over the course of this study (Fig. 3). Pond 2 North pH was highest in the spring and most acidic at the end of summer. Pond 1 pH was always higher than Pond 2 North and displayed less variance. Complete water chemistry results from the 05/22/2014, 10/09/2014, and 09/16/2015 samplings are given in Table 4 and 5.

Year	AMD Treatment Dates	AMD Volume
2013	07/5-26	10,083,235 liters
2014	09/12-17	3,012,400 liters

Table 3 Leviathan Mine AMD treatment (data from the California Regional Water Quality Control Board, Lahontan Region)

Parameters	Units	Pond 1 (at inlet)	Pond 2 North	Heenan Lake
Chl-a	μg/L	1.22	1.59	9.97
Pheophytin	μg/L	0.70	4.30	6.54

Table 4 Water samples collected on 09/15/2015. Water quality data analyzed at the University of Nevada- Reno, Aquatic Ecosystem Laboratory

Parameter	Units	Sampled on 05/22/14			Sampled on 10/09/14	
		Pond 1 (at inlet, SE shore)	Pond 2S	Pond 3	Pond 1 (at inlet, SE shore)	Pond 2N
pH (lab)	pH	2.84	2.64	3.76	3.09	2.31
pH (field)	pH	2.65	2.59	3.72	2.97	2.23
Temperature (lab)	℃	18.5	19.3	18.7	21.2	21.2
Temperature (field)	℃	18.2	15.4	20.3	18.1	22.2
Redox Potential (Eh)	mV	663	721	621	619	794
Total Dissolved Solids (TDS)	mg/L	5100	4800	6800	3700	33000
Turbidity	NTU	1.5	3.7	19	11	2.4
Alkalinity, Total	mg/L CaCO$_3$	<2	<2	<2		
Alkalinity/Bicarbonate	mg/L CaCO$_3$	<2	<2	<2		
Alkalinity/Carbonate	mg/L CaCO$_3$	<2	<2	<2		
Alkalinity/Hydroxide	mg/L CaCO$_3$	<2	<2	<2		
Aluminum	mg/L	270	280	190		
Antimony	mg/L	<0.002	<0.002	<0.002		
Arsenic	mg/L	4.6	2.1	0.02		
Barium	mg/L	0.006	0.002	0.008		
Beryllium	mg/L	0.01	0.01	0.01		
Boron	mg/L	0.11	0.1	0.31		
Cadmium	mg/L	0.023	0.029	0.11		
Calcium	mg/L	140	160	310		
Chloride	mg/L	8	9	13		
Chromium	mg/L	0.56	0.57	0.048		
Cobalt	mg/L	1.4	1.4	4.2		
Copper	mg/L	0.72	1.3	1.1		
Ferric Iron	mg/L	70	280	<1	30	2200
Ferrous Iron	mg/L	390	32	8	500	15
Total Iron	mg/L	460	312	8	530	2215
Fluoride	mg/L	6	6	10		
Lead	mg/L	<0.002	<0.002	<0.002		
Magnesium	mg/L	38	39	650		
Manganese	mg/L	9.1	8.8	24		
Mercury	mg/L	<0.0001	<0.0001	<0.0001		
Nickel	mg/L	4	4.9	9.2		
Nitrate	mg/L	0.22	<0.05	1.2		
Phosphorus Total	mg/L	3.2	1.7	0.07		
Potassium	mg/L	7.5	0.53	<0.5		
Selenium	mg/L	<0.01	<0.01	<0.01		
Silica	mg/L	84	79	42		

Silver	mg/L	<0.002	<0.002	<0.002		
Sodium	mg/L	28	14	30		
Sulfate	mg/L	3300	3200	4800		
Thallium	mg/L	0.15	0.008	0.024		
Zinc	mg/L	0.72	0.72	2.3		

Table 4 Water quality data analyzed at SEM Inc. (Reno, NV)

b. Water Spectroscopy

Airborne spectra from natural water bodies and Leviathan ponds are summarized in Fig. 4. The spectral curves of natural water bodies were very diverse. The wavelength at which peak reflectance occurred varied between 405 nm and 570 nm. Wavelength of peak reflectance in natural water bodies and Leviathan waters are summarized in Fig. 5. "Pristine" waters such as Lake Tahoe displayed peak reflectance at the shortest wavelengths (the blue region). Absorption features between 400 nm and 725 nm varied significantly between different natural water bodies. Most natural water bodies decreased to a minima of virtually 100 percent absorption beyond 725 nm.

Leviathan water was characterized by low reflectance between 400-500 nm, followed by a steeply increasing slope through the blue/green regions (400-650 nm). Peak reflectance occurred between 638 and 648 nm. A narrow absorption feature occurred at 675 nm; depth of this feature varied between ponds and images. A second peak absorption occurred at about 690 nm, followed by a very steep decreasing slope to about 740 nm. A final slight peak occurred at 811 nm, which was more pronounced in the 2014 images. Beyond 840 nm, reflectance was featureless but did not drop to zero reflectance. The Leviathan water had notably higher overall reflectance than all other water bodies examined. Note that only Leviathan water ROIs from spring flights were used in this comparison. ROIs from summer and fall flights were intentionally left out because the pond water levels were not deep enough to ensure minimal effect from bottom reflectance.

Leviathan Pond 1 water reflectance and spectral first derivatives are summarized in Fig. 6. All curves were rather similar with exception of the 09/2014 water, which had greater overall reflectance and a different shape. This curve contained a shoulder feature at 675 nm, following peak reflectance at 705 nm, a broad minimum from about 750 nm to 800 nm, and a slight shoulder at 850 nm before reaching minimal reflectance by 950 nm. Among the remaining curves, the intensity of the absorption feature at 675 nm varied. The curve from 11/2014 had the deepest absorption at 675 nm. Finally, the wavelength of peak reflectance differed between the spring/early-summer and late-summer/fall curves. Peak reflectance occurred at 648 nm in the April-June curves, and at 695 nm in the September-November curves. Spectral first derivatives were used in an attempt to further identify unique spectral features. However, no major differences were identified between the Pond 1 ROI spectral first derivatives.

The reflectance progression from deep to shallow pixels in the Leviathan ponds are summarized in Fig. 7a-b. For comparison, a depth progression along the northeast shore of Lake Tahoe was also included (Fig. 7c). The depth of the water column in the center of Pond 1 and Pond 2 North during the 4/2014 flight was approximately 1.28 meters and 1 meter, respectively. The deepest pixels had the lowest overall reflectance. As the water column became shallower, overall reflectance increased and reflectance became higher at 695 nm. The shallowest pixels had two reflectance maximums (648 nm, 695 nm). The minor maxima feature between 800-810 nm strengthened in the shallower pixels. A similar trend of increased overall reflectance and peak reflectance at longer wavelengths with shallower water was also seen in the Lake Tahoe curves.

6.   Discussion

Pristine natural inland waters, such as Lake Tahoe, have peak reflectance at short wavelengths (appearing blue) because of inherent properties of the water molecule. At wavelengths less than 580 nm, the attenuation of light in water is primarily due to scattering by the water molecule, while at wavelengths greater than 580 nm, scattering is insignificant and attenuation is due to absorption by the water molecule (Bukata 1995). While blue light is greatly scattered by water molecules, red light is strongly absorbed, an absorption band that is peripheral to a stronger NIR absorption at wavelengths greater than 700 nm (Bukata 1995). With the absence of suspended constituents in a pure water column, a spectrum will peak in reflectance at blue wavelengths and remain essentially featureless as absorption gradually increases to 100 percent into the NIR. This is well demonstrated in the curves from deep water in Lake Tahoe (Fig. 7c). The other natural water bodies in this study are influenced by suspended material and exhibit peak reflectance at green or yellow wavelengths, but similarly absorb strongly at red wavelengths.

Mine water does not exhibit the typical reflectance properties of pure water. The shift in peak reflectance to longer wavelengths and very high overall reflectance are unique characteristics of Leviathan mine waters—no other water bodies in this dataset contain comparable features. Peak reflectance between 638-698 nm gives Leviathan water a dark red color. Gammons et al. (2009) notes that a common source of colorant in pit lake waters results from the oxidation of dissolved iron to hydrous ferric oxide (HFO), a red-brown substance that is very fine-grained and slow to settle by gravity. Given the high iron concentration (about 600 mg/L Fe) and low turbidity (2-11 NTU) of Leviathan water, the source of colorant is likely due to ferric iron complexed with sulfate anions or colloidal size HFOs (Davies and Calvin 2015, in review). The intensity of reflectance at red wavelengths is likely influenced by the quantity of aqueous ferric iron species in the water column. Therefore, this unique spectral shape and high overall reflectance could be used as a preliminary indicator of high ferric iron concentrations in mine pit lakes with low pH.

In transparent shallow natural water bodies, the bottom material imparts its color to the water column, influencing its optical properties (Lodhi 2002). This is well illustrated in Lake Tahoe (Fig. 7c), as water depth decreases, the bottom influence increases, shifting the color (peak reflectance) of water toward yellow and increasing the reflectance maximum. The wavelength of peak reflectance in Leviathan water is also affected by the depth of the water column. In the pixel-by-pixel depth comparison of both Pond 1 and Pond 2 North (Fig. 7a-b), the shallowest pixels have higher overall reflectance and peak reflectance shifts from 648 nm to 695 nm. In the seasonal variation of Pond 1 (Fig. 6), the effect of bottom reflectance is apparent in the September and November images. The water column in Pond 1 is shallower in the fall images than in the spring/early-summer images, as the majority of AMD has been treated for the season. Wavelength of peak reflectance is shifted from 638 nm in the spring images to 695 nm in the fall images.

Wide variability is seen in the field spectra of pond water (Fig. 8). This is attributed to bottom reflectance as well as low incidence angle. Collecting a "pure" spectra of deep pond water with a field spectrometer is difficult because the field of view is not close to a 90 degree incident angle, as it is from an airborne sensor. However, the same trend of shifted peak reflectance in shallow waters is present in the field spectra.

The consistency of Pond 1's water curves throughout the 2013-2014 seasonal images is reasonable given the stability of pH and iron concentrations. The pH varied from 2.65 to 2.97, which is seemingly not significant enough to identify major changes in the water's airborne spectral curves. The absorption feature at 675 nm, which occurs in all pond water curves, is likely due to phytoplankton biomass (Mishra and Mishra 2012; Mishra et al. 2014). Although measured chl-a concentrations are quite low (1.22-1.59 μg/L), they are large enough to plausibly affect the ponds' spectral reflectance (Pilorz and Davis 1990; Hamilton et al. 1993). Green algae is visible in the ponds throughout the year (Fig. 9). Variation in the intensity of this feature is most likely due to seasonal variation in nutrient availability and sunlight. Riaza et al. (2012a; 2012b; 2015) also notes an absorption feature at 675 nm in mine water attributed to vegetation. The surprising prominence of this 675 nm feature could also be attributed to bottom reflectance from the bright pond liner material. Rundquist et al. (1995) and Lodhi and Rundquist (2001) note that bottom brightness may accentuate the chl-a signal in algal waters.

The one outlier curve in the Pond 1 seasonal variation comparison (Fig. 6) can be attributed to turbidity and bottom reflectance. Although no direct turbidity measurements were taken on the day of the 09/2014 flight, water treatment commenced just two days prior to the flight (much later than the usual annual water treatment). Surplus lime was deposited onto the north shore of Pond 1 after water treatment, and this likely produced high turbidity as the remaining AMD water in Pond 1 experienced neutralization reactions along the north shore. Turbidity has the potential to greatly impact a water's reflectance (Campbell and Wynne 2011). More suspended sediments in a water column results in a shift in reflectance toward longer wavelengths in the VSWIR region (Lodhi 2002).

The one other mine affected water in this study, Yerington pit lake, has a very different spectral curve from Leviathan water (Fig. 4). Yerington water quality is generally good in terms of pH and iron concentration (pH=8.1, 0.01 mg/L Fe). However, selenium, copper, SO_4^{2-}, and TDS are elevated and prevent the water from meeting water quality standards (Hershey 2010). The spectral shape and reflectance intensity diagnostic criteria for poor pit lake water quality described here should be restricted to waters that have potential for acidic, not alkaline conditions.

Due to the relatively small area and shallow depth of the Leviathan ponds, mine water ROIs consist of a limited number of pixels. Each ROI represents about 2300 to 5600 square meters of water surface. The techniques discussed in this study should be limited to higher spatial resolution data, or over large areas of mine-affected waters at least 2300 square meters in size. The authors are hesitant to recommend application of these techniques to river channels or small streams because of their narrow size, irregular depth, and likelihood for high turbidity.

It should be noted, higher resolution airborne imagery was acquired over Leviathan in August of 2007 when the ponds were close to empty. The spectra of these water pixels are strongly influenced by bottom reflectance, yet exhibit a reflectance peak between 640 and 695 nm, and a sharp 675 nm absorption. The curves are comparable to those acquired in the 2013-2014 AVIRIS imagery, illustrating the consistency of the red peak reflectance as an indicator of low pH and elevated iron in solution, across years and different sensors. These spectra will be discussed in a separate work along with surface mineralogy of the site.

Comparison to Pit Lake Literature:

The wavelength of peak reflectance in Leviathan pond water is unique compared to hyperspectral acidic mine water curves in the literature (author only knows of three papers, Table 6). Peak reflectance at longer wavelengths give water an intense red color, which is also noted in Riaza et al. (2012a). Turbidity and bottom reflectance affect the spectral response of Leviathan pond water greatly in the fall, and less so in the spring. Although other studies mention these parameters as influences on the spectral response of mine waters, none explicitly state measurements of such parameters. As seen in the Leviathan data, those parameters affect the spectral curve of mine water and should be quantified in order to make conclusive estimates on mine water quality.

The airborne spectral curves from the Leviathan ponds are similar to laboratory spectral curves of synthetic AMD water and Leviathan water in Davies and Calvin (2015, in review). The laboratory curves are also characterized by strong absorption from 350 to 600 nm and high reflectance at red wavelengths (Fig. 10). Although similar, the airborne spectra are not directly comparable to the laboratory spectra. Laboratory spectroscopy differs from airborne spectroscopy in three ways: 1) individual samples are

analyzed under controlled conditions using artificial illumination; 2) there is little interfering atmosphere to block portions of the electromagnetic spectrum; and 3) spectral resolution and signal-to-noise ratio can be much higher (Swayze et al. 2009). Consequently, laboratory spectral measurements of acid waters can have much higher sensitivity to chemical changes in a small sample volumes compared to remote spectral measurements of Leviathan ponds. Additionally, fall airborne spectral curves were strongly affected by bottom reflectance, and therefore should certainly not be compared directly to laboratory spectral studies. Such comparisons for quantitative analysis would produce erroneous results. Environmental factors such as bottom reflectance, water column depth, and biomass cause the airborne spectral curves to deviate from our laboratory curves.

Study	Peak Reflectance (nm)	pH	Fe (mg/L)	SO_4^{2-} (mg/L)	Turbidity (NTU)	Chl-a (μg/L	Depth of Water Column (m)
Gläβer et al. (2011) Central Germany, "Iron Stage" Lignite Mine Lake	~670	<3.0	97	1,600	--	--	0.76 (secchi disk depth)
Gläβer et al. (2011) Central Germany, "Transition Stage" Lignite Mine Lake	560	4.5-7.3	0.2	420	--	1.7	2.4 (secchi disk depth)
Riaza et al. (2012a) Iberian Pyrite Belt, "Pyrite Pond"	580	3.0	--	2,093	--	--	--
Riaza et al. (2015) Odiel River, Spain	567-640	3.0	--	--	--	--	--
Leviathan Mine Ponds, CA	648	2.6	400	3,200	1.5-11	1.22-1.59	~1.5

Table 6 Studies in the literature that employ hyperspectral imagery for pit lake water quality analysis

7. Conclusions

Multi-season airborne hyperspectral imagery was successfully used to identify the unique properties of mine water. The spectral curves of acidic water at Leviathan Mine were characterized by shifted peak reflectance to red wavelengths and high overall reflectance. Environmental influences including bottom reflectance, turbidity, biomass, and seasonality, strongly affected the spectral signatures. Water curves from the fall images were considered contaminated by bottom reflectance and turbidity. A prominent absorption feature at 675 nm was identified and linked to biomass. Efforts to quantify this feature for chl-a concentration were not attempted as this wavelength region is strongly influenced by the inherent properties of mine water and by bottom brightness. Airborne spectral curves could not be directly compared to laboratory spectral studies. For this application, a study area with more constant water levels

and larger variation in pH and ferric iron concentration is needed. Locations such as the Berkeley Pit Lake in Montana or the Lone Tree Pit Lake in Nevada are suggested for promising study sites. Leviathan's water spectral curves were unique when compared to the limited number of pit lakes in the literature, demonstrating the wide variety of mine water chemistries and their spectral properties. These results show potential for use of hyperspectral imagery in the monitoring of pit lake water chemistry. As a minimum, pit lake waters which have a spectral curve with peak reflectance in the red region can be identified as having potentially poor water quality linked to acidic pH and dissolved iron. These techniques should be limited to higher spatial resolution data, or over large areas of mine-affected waters at least 2300 square meters in size.

8. Figures
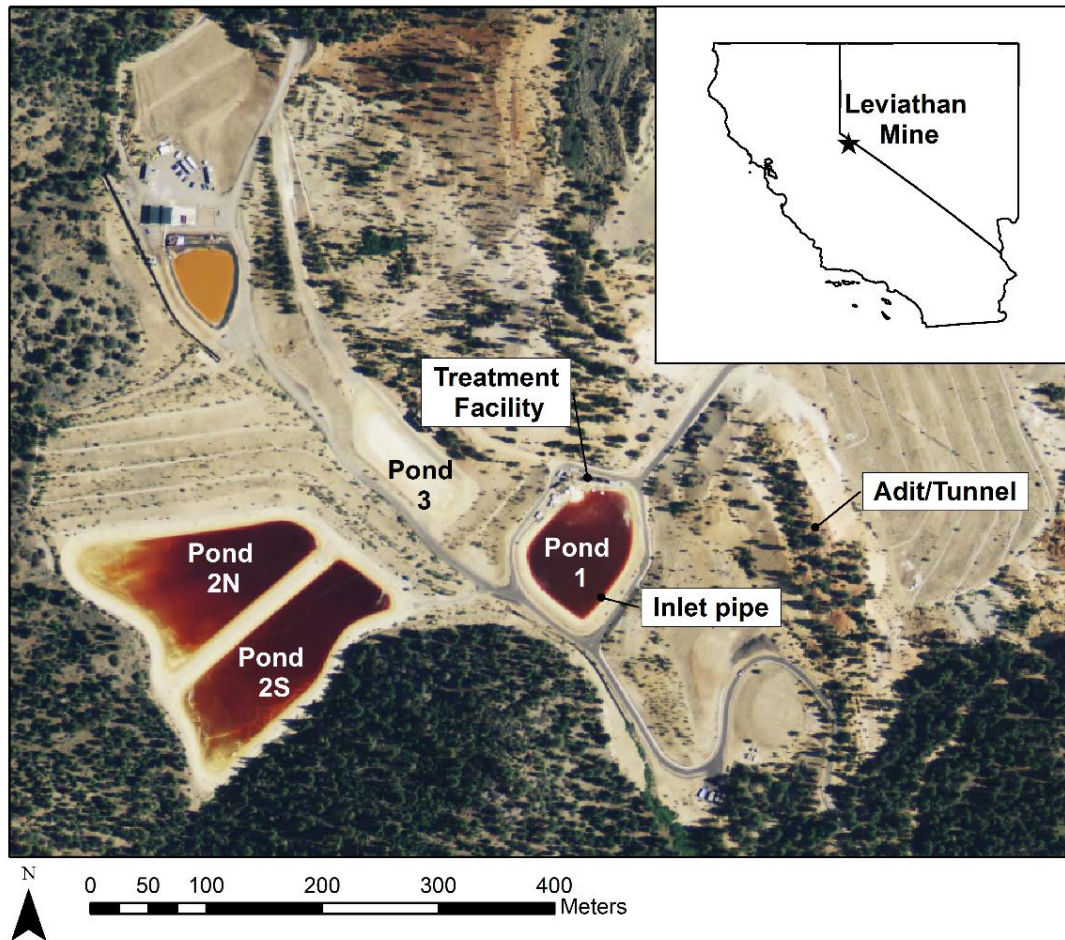
Fig. 1 Leviathan Mine is located in Alpine County, California, 10 miles east of Markleeville and 2 miles north of the Monitor Pass Highway (Sections 15 and 22, Township 10N, Range 21E)
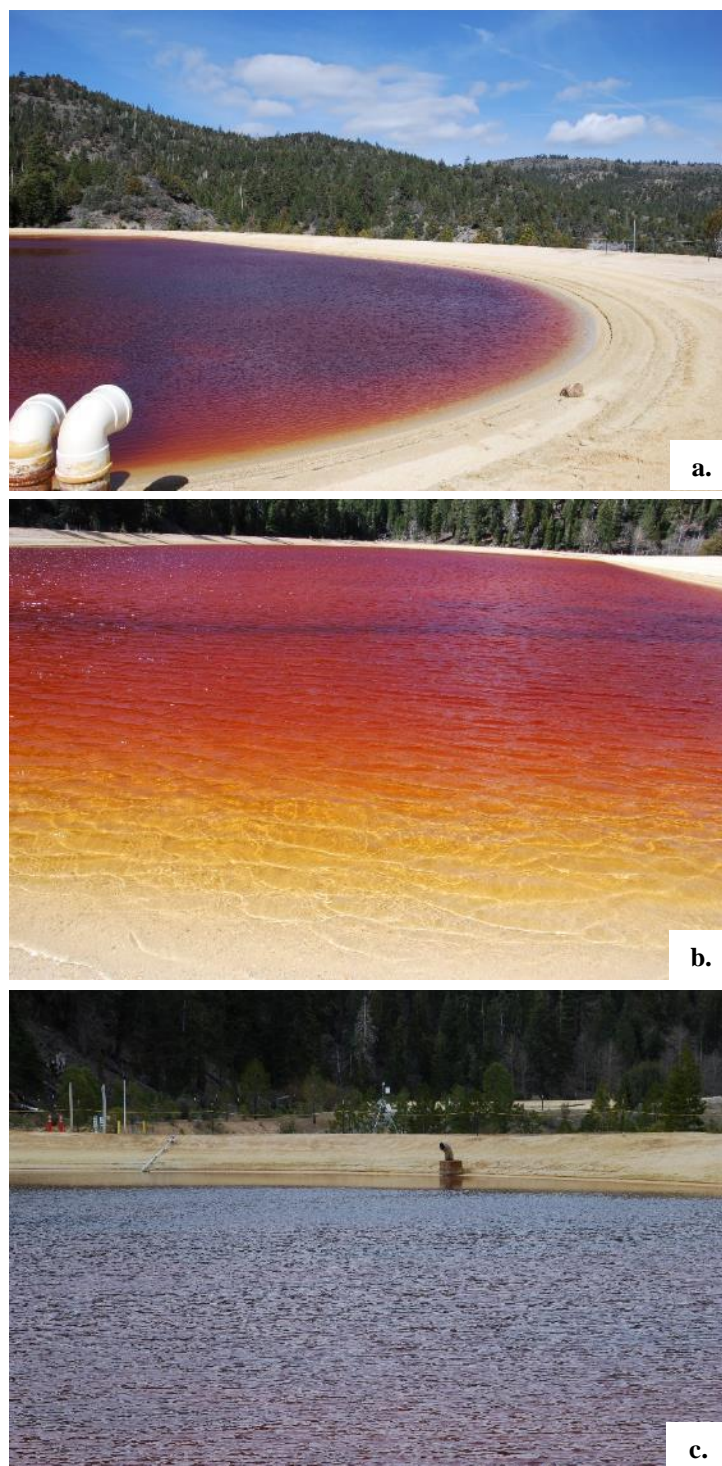
Fig. 2 Leviathan Mine: a) From the east shore of Pond 2 North facing north. Photo taken by author on 04/24/2014. b) From east shore of Pond 2 South facing west. Width of pond in field of view = 7 meters. Photo taken by author on 04/24/2014. c) From the north shore of Pond 1 facing west. Photo taken by author on 04/24/2014 (Photos are not retouched)
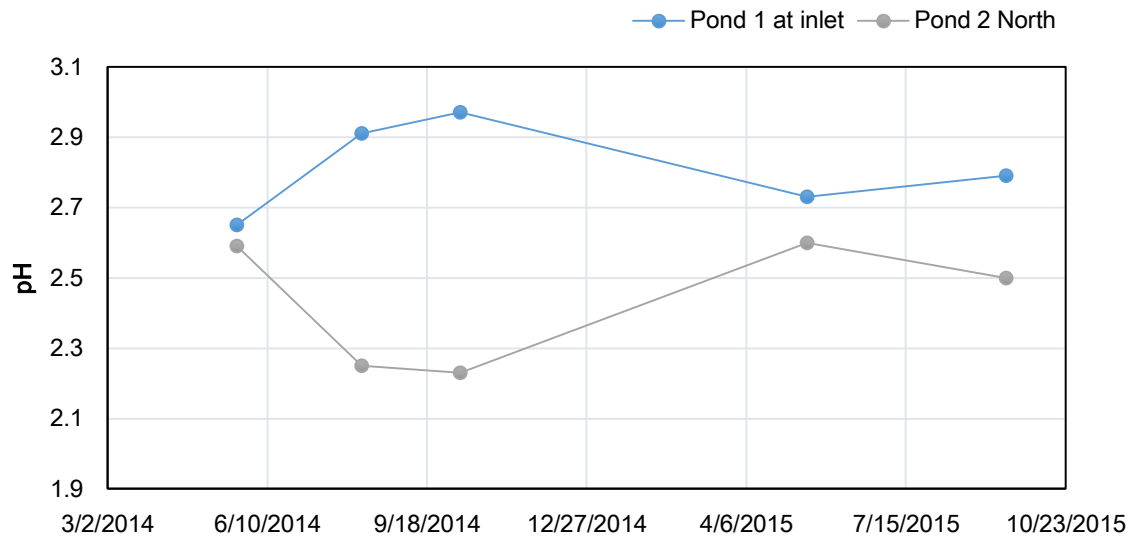
Fig. 3 Pond water pH variation from 5/22/2014 to 9/16/2015
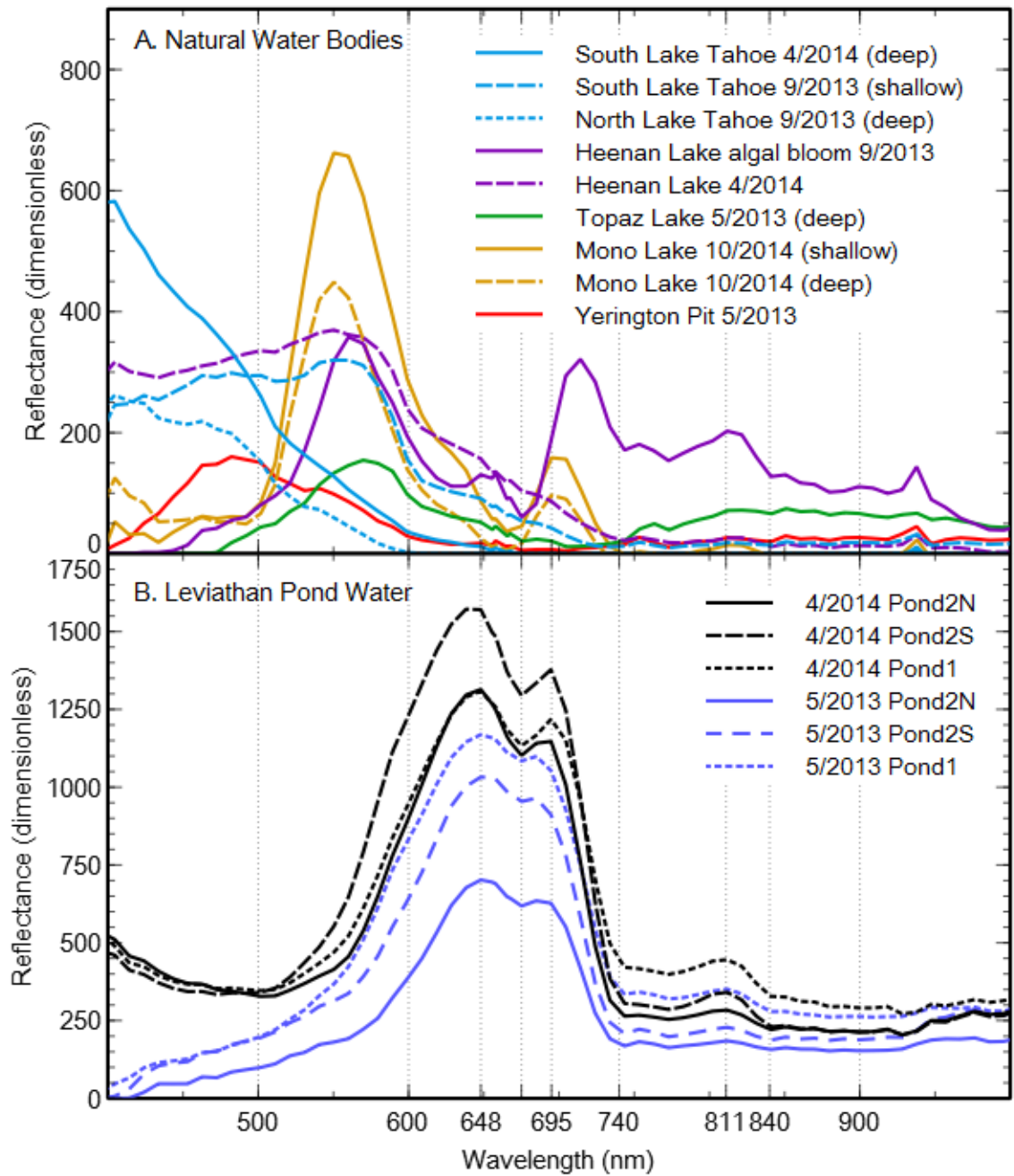
Fig. 4 Water body ROI comparison. Gridlines at 500, 600, 648, 675, 695, 740, 811, 840, and 900 nm
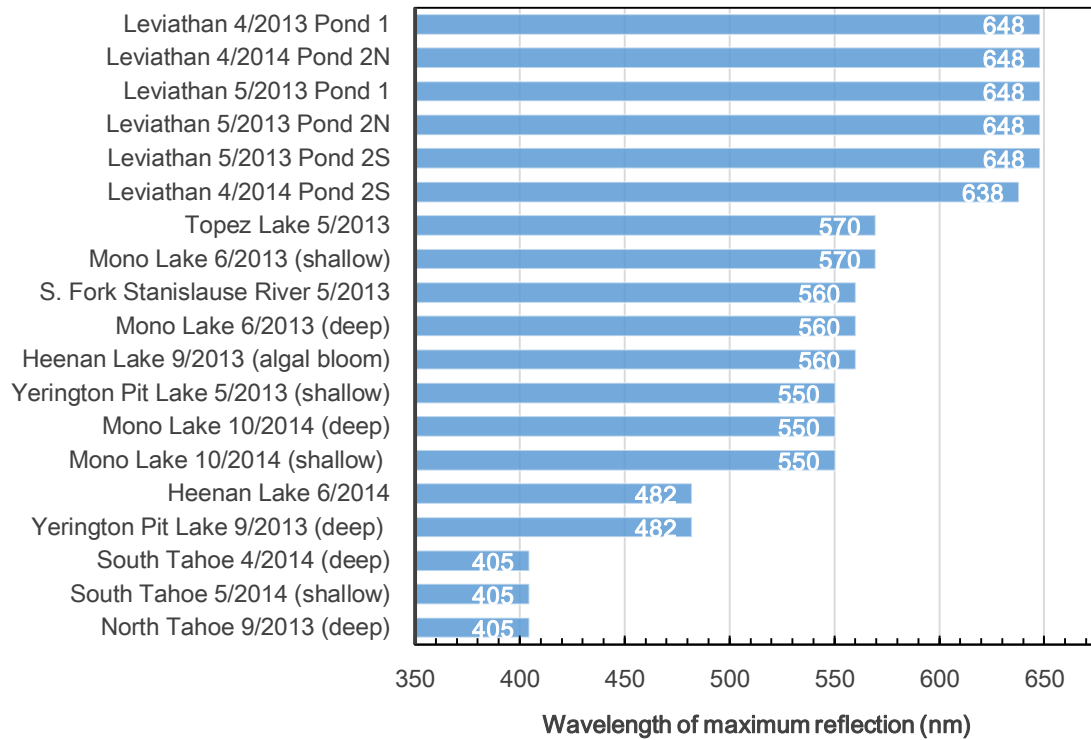
Fig. 5 Wavelength of peak reflectance in water body ROI comparison
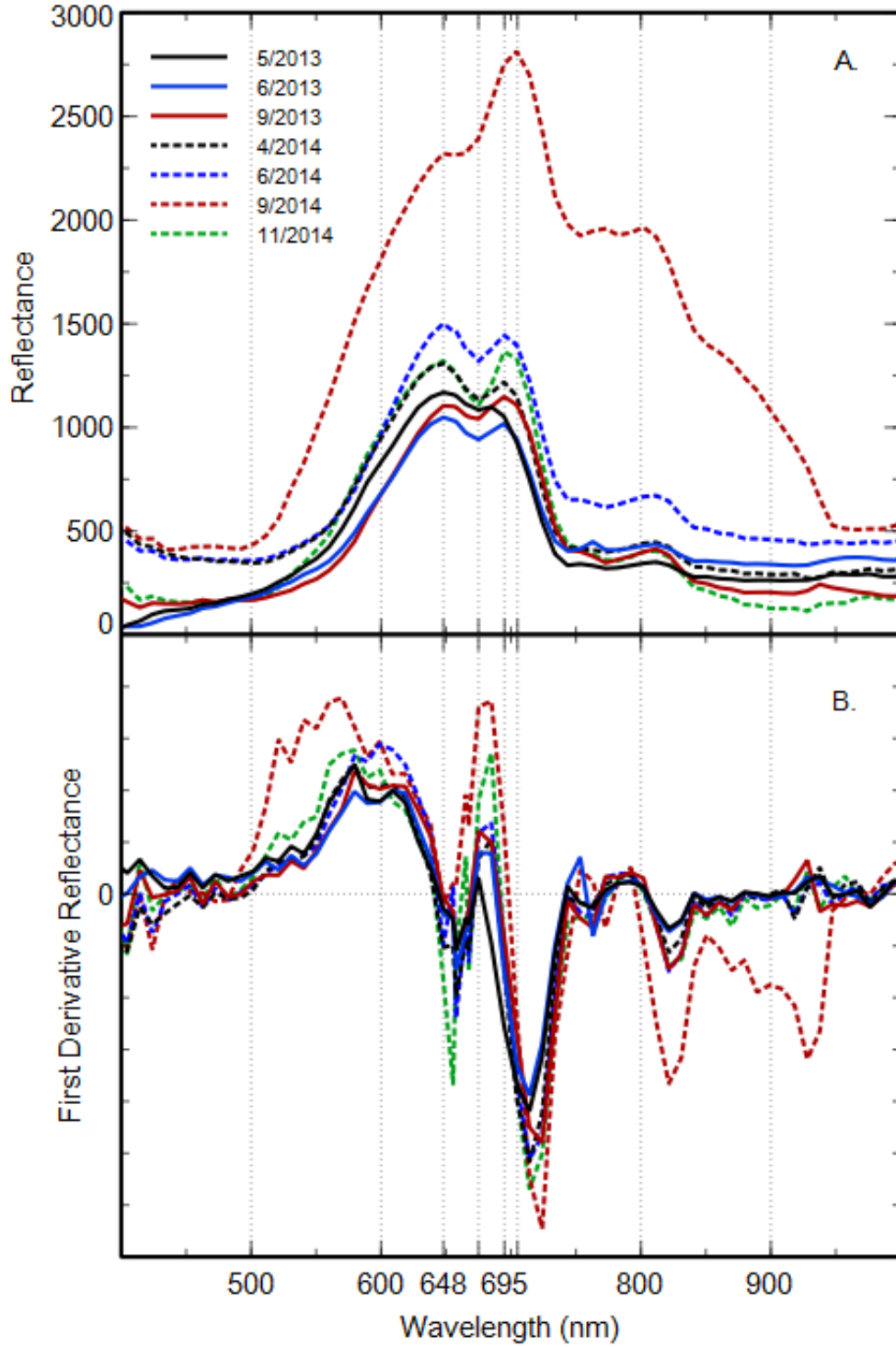
Fig. 6 Pond 1 ROI comparison. a) Spectral reflectance b) Spectral first derivative reflectance. Gridlines at 500, 600, 648, 675, 695, 705, 800, and 900
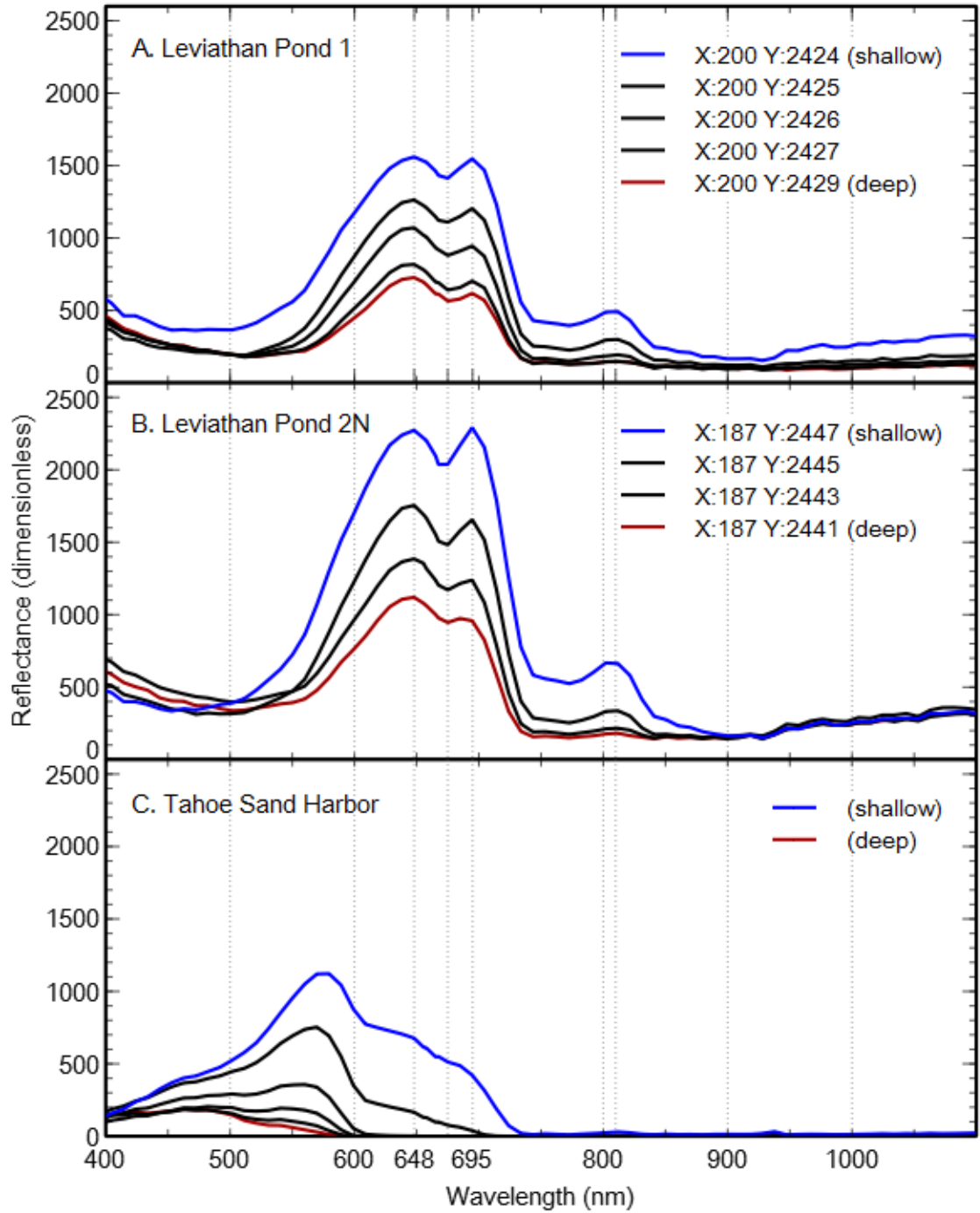
Fig. 7 Pixel-by-pixel water depth comparison from 4/2014 flight. Gridlines at 500, 600, 648, 675, 695, 800, 810, 900, and 1000
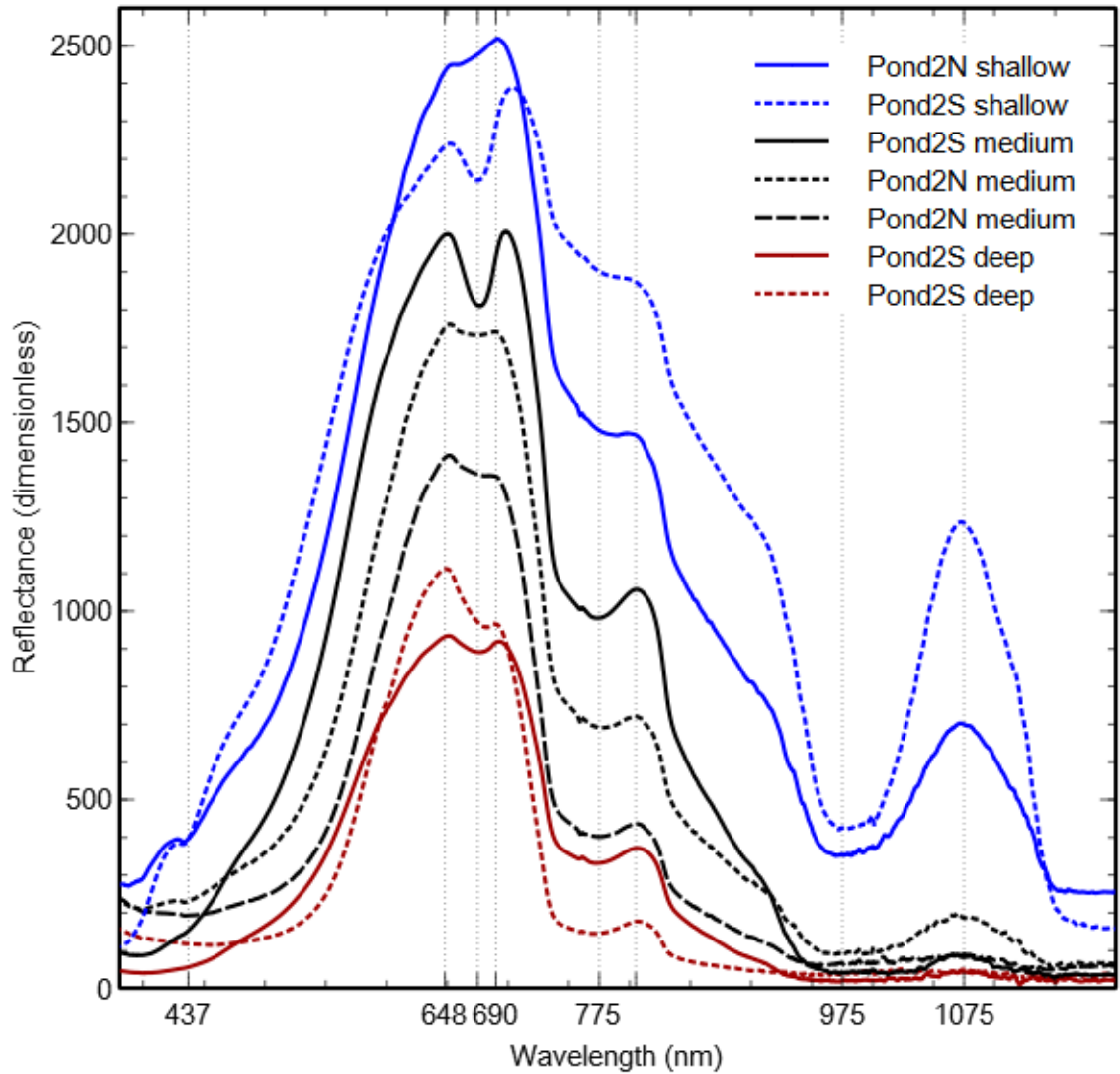
Fig. 8 Field data from Pond 2 North and 2 South on 04/24/14. Spectra collected from the rim of ponds with ASD pistol grip pointed downward at shallow to deep water. Gridlines at 437, 648, 675, 690, 775, 805, 975, and 1075 nm
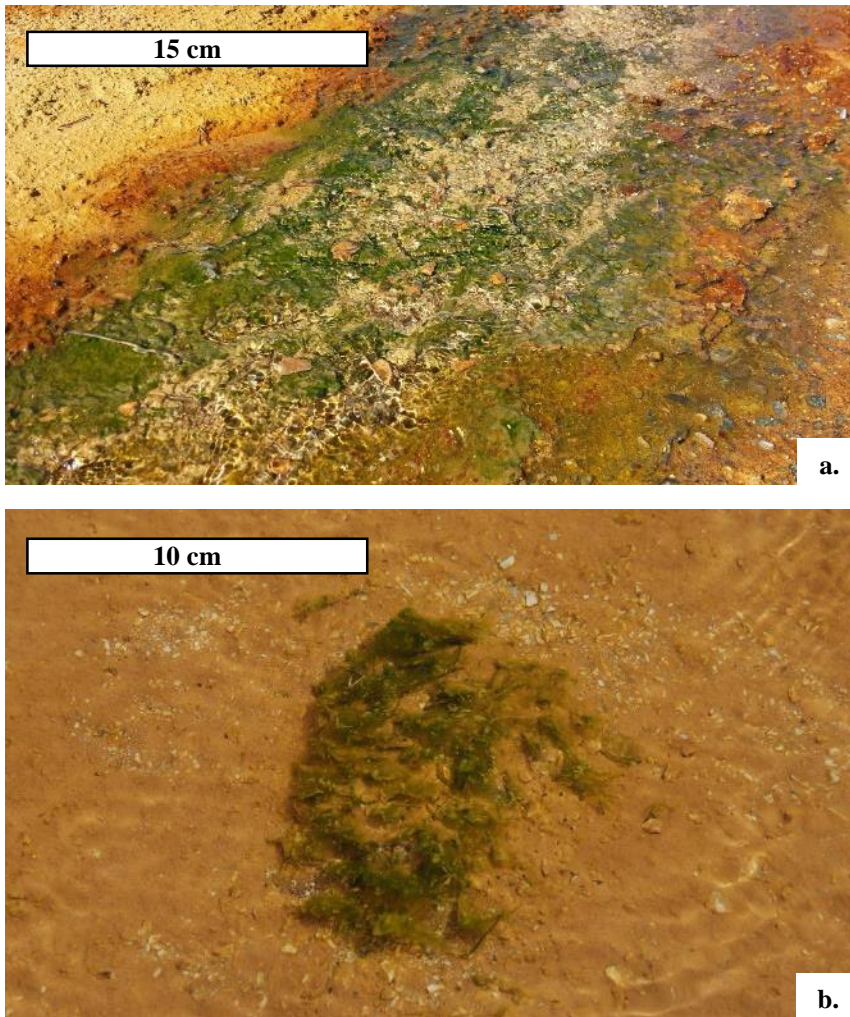
Fig. 9 Algal growth on Leviathan pond liners: a) Pond 1. Photo taken by author on 10/09/2014 b.) Pond 3. Photo taken by author on 04/24/14
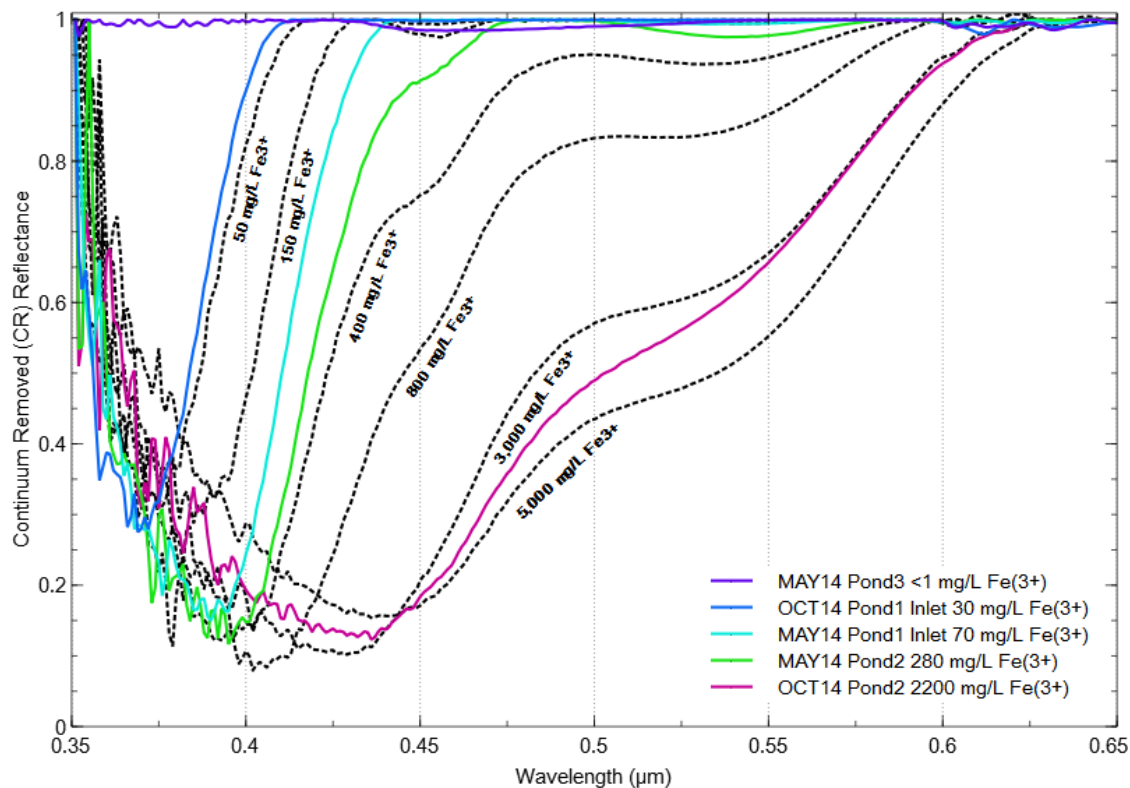
Fig. 10 Continuum Removed (CR) Reflectance of acid waters from: Davies and Calvin (2015) Quantifying iron concentration in local and synthetic acid mine drainage waters: A new technique using handheld field spectrometers (manuscript submitted for publication 09/2015). Colored plots are local AMD samples with known Fe concentration (from SEM Inc. analysis). Local AMD samples are unfiltered. Dotted contour plots are from synthetic AMD solutions

9. References

Bukata PB, Jerome JH, Kondratyev KY, Pozdnyakov DV (1995) Optical properties and remote sensing of inland and coastal waters. CRC Press, New York

California Dept of Health Services (2003) Public Health Assessment: Evaluation of Leviathan Mine Site. Agency for Toxic Substances and Disease Registry. http://www.atsdr.cdc.gov/HAC/pha/PHA.asp?docid=33&pg=0. Accessed 1 September 2015

California Regional Water Quality Control Board, Lahontan Region (2015) Year-end report for the 2014 field season at Leviathan Mine. http://www.swrcb.ca.gov/lahontan/water_issues/projects/leviathan_project/docs/lev2014rpt.pdf. Accessed 20 August 20 2015

Campbell JB, Wynne RH (2011) Ch.19 Hydrospheric sciences. In: Introduction to remote sensing 5th edition. Guilford Press, New York, New York, pp 549-584

Castendyk DN, Eary LE (2009) Ch.1 The nature and global distribution of pit lakes. In: Mine pit lakes - characteristics, predictive modeling, and sustainability, Vol 3. Society for mining, metallurgy, and exploration, Inc. (SME), electronic edition, pp 1-11

Davies GE, Calvin WM (2015) Quantifying iron concentration in local and synthetic acid mine drainage waters: A new technique using handheld field spectrometers (manuscript in review)

Environmental Protection Agency (2006) EPA Hardrock Mining Innovative Technology Case Study, Leviathan Mine. http://semspub.epa.gov/src/collection/HQ/SC32068. Accessed 3 November 2015

Evans JR (1977) Zaca mine and Leviathan mine. In: Mines and mineral resources of alpine county, California, county report 8. California division of mines and geology, pp 22–27

Gammons CH, Harris LN, Castro LM, Cott PA, Hanna BW (2009) Creating lakes from open pit mines: process and considerations, with emphasis on northern environments. Canadian technical report of fisheries and aquatic sciences. http://digitalcommons.mtech.edu/geol_engr/2/. Accessed 3 November 2015

Gläβer C, Groth D, Frauendorf J (2011) Monitoring of hydrochemical parameters of lignite mining lakes in Central Germany using airborne hyperspectral casi-scanner data. International Journal of Coal Geology 86: 40–53. doi:10.1016/j.coal.2011.01.007

Hamilton MK, Davis CO, Rhea WJ, Pilorz SH (1993) Estimating chlorophyll content and bathymetry of Lake Tahoe using AVIRIS data. Remote Sens. Environ. 44: 217-230. doi:10.1016/0034-4257(93)90017-R

Hershey RL (2010) Limnology, Arsenic Sorption, and Geochemical Modeling of Mine Pit Lakes. Dissertation, University of Nevada, Reno

Javor B (1999) Ch.20 Hypersaline, alkaline lakes. In: Hypersaline environments: Microbiology and biogeochemistry. Springer-Verlag, New York, pp 292-301. doi:10.1007/978-3-642-74370-2

Jerlov NG (1976) Marine Optics 2nd edition. Elsevier, New York

Kopackova V (2014) Using multi spectral feature analysis for quantitative pH mapping in a mining environment. International Journal of Applied Earth Observation and Geoinformation 28: 28-42. doi:10.1016/j.jag.2013.10.008

Kruse FA, Lefkoff AB (1993) Knowledge-based geologic mapping with imaging spectrometers. Remote Sensing Reviews, special issue on NASA Innovative Research Program (IRP) results 8: 3-28. doi:10.1080/02757259309532188

Lodhi MA (2002) Influence of bright bottom depth on reflectance from clear and turbid water bodies. Geocarto International, 17, 3, 7-15. doi:10.1080/10106040208542239

Lodhi MA, Rundquist DC (2001) A spectral analysis of bottom-induced variation in the colour of Sand Hills lakes, Nebraska, USA. Int. J. Remote Sensing 22: 9: 1665-1682. doi:10.1080/01431160117495

Lottermoser BG (2003) Ch.3 Mine water. In: Mine wastes. Springer, New York, pp 83-141

Miller G (2002) Precious metals pit lakes: Controls on eventual water quality. Southwest Hydrology 1: 3: 16-17

Mishra S, Mishra D (2012) Normalized difference chlorophyll index: A novel model for remote estimation of chlorophyll-a concentration in turbid productive waters. Remote Sensing of Environment 117: 394-406. doi:10.1016/j.rse.2011.10.016

Mishra DR, Schaeffer BA, Keith D (2014) Performance evaluation of normalized difference chlorophyll index in northern Gulf of Mexico estuaries using the hyperspectral imager for the coastal ocean. GIScience & Remote Sensing 51: 2: 175-198. doi:10.1080/15481603.2014.895581

Montero IC, Brimhalla GH, Alpers CN, Swayze GA (2005) Characterization of waste rock associated with acid drainage at the Penn mine, California, by ground-based visible to short-wave infrared reflectance spectroscopy assisted by digital mapping. Chemical Geology, 215, 453-472. doi:10.1016/j.chemgeo.2004.06.045

Nevada Division of Environmental Protection (2008) Nutrient assessment protocols for lakes and reservoirs in Nevada. http://ndep.nv.gov/BWQP/file/nutrientprotocols_lakes.pdf. Accessed 6 November 2015

Pilzor SH, Davis CO (1990) Investigations of ocean reflectance with AVIRIS data. In: Proceedings of the second airborne visible/infrared imaging spectrometer workshop, JPL publication 90-54, Pasadena, CA, pp 224-231

Riaza A, Buzzi J, Garcia-Melendez E, Vazquez I, Bellido E, Carrere V, Müller A (2012a) Pyrite mine waste and water mapping using Hymap and Hyperion hyperspectral data. Environmental Earth Science, 66, 1957-1971. doi:10.1007/s12665-011-1422-0

Riaza A, Buzzi J, Garcia-Melendez E, Carrere V, Sarmiento A, Muller A (2012b) River acid mine drainage: sediment and water mapping through hyperspectral Hymap data. International Journal of Remote Sensing 33: 19: 6163–6185. doi:10.1080/01431161.2012.675454

Riaza A, Buzzi J, Garcia-Melendez E, Carrere V, Sarmiento A, Muller A (2015) Monitoring acidic water in a polluted river with hyperspectral remote sensing (HyMap). Hydrological Sciences Journal 60: 6: 1064-1077. doi:10.1080/02626667.2014.899704

Rundquist DC, Schalles JF, Peake JS (1995) The response of volume reflectance to manipulated Algal concentrations above bright and dark bottoms at various depths in an experimental pool. Geocarto International 10: 4: 5-14. doi:0.1080/10106049509354508

Schroeter L, Gläβer C (2011) Analyses and monitoring of lignite mining lakes in Eastern Germany with spectral signatures of Landsat TM satellite data. International Journal of Coal Geology 86: 27–39. doi:10.1016/j.coal.2011.01.005

Shevenell LA (2000) Water quality in pit lakes in disseminated gold deposits compared to two natural, terminal lakes in Nevada. Environmental Geology 36: 7: 807-815. doi:10.1007/s002540050497

Swayze GA, Smith KS, Clark RN, Sutley SJ, Pearson RM, Vance SJ, Hageman PL, Briggs PH, Meier AL, Singleton MJ, Roth S (2000) Using imaging spectroscopy to map acidic mine waste. Environmental Science Technology, 34, 47-54. doi:10.1021/es990046w

Swayze GA, Clark RN, Sutley SJ, Hoefen TM, Plumlee GS, Meeker GP, Brownfield IK, Livo KE, Morath LC (2006) Spectroscopic and x-ray diffraction analysis of asbestos in the world trade center dust: Asbestos content of the settled dust. In: Urban aerosols and their impacts. doi:10.1021/bk-2006-0919.ch003

Vandersluis GD, Straskraba V, Effner SA (1995) Hydrogeological and Geochemical Aspects of Lakes Forming in Abandoned Open Pit Mines. In: proceedings of Water Resources at Risk. IMWA-162-IMWA-177. https://www.imwa.info/imwa-meetings/proceedings/197-proceedings-1995.html. Accessed 6 November 2015

Vikre PG, Henry CD (2011) Quartz-alunite alteration cells in the southern segment of ancestral Cascades magmatic arc. In: Steininger R, Pennell B, eds., Great Basin evolution and metallogeny: Geological Society of Nevada 2010 Symposium: Lancaster, Pennsylvania, DEStech Publications, Inc., pp 701-745

Chapter 3—Manuscript draft for future submission

Title: Mapping acidic mine waste with seasonal airborne hyperspectral imagery at varying spatial scales.

1. Introduction
2. Study Area—Leviathan Mine
3. Dataset
4. Methods
5. Results
   a. Field Spectra
   b. DCS, Band Ratio
   c. Spectral Hourglass Wizard
6. Discussion
7. Conclusions
8. Figures
9. References

1. Introduction

Acid mine drainage (AMD) resulting from the oxidation of sulfides in mine waste is a major environmental issue facing the mining industry today (Lottermoser 2003). It is estimated that mining activities in the United States produce between 9.1×10^{11} and 1.8×10^{12} kg (1-2 billion tons) of solid mine waste annually (MSE 2000). The weathering of mine wastes may produce acidity and the release of heavy metals, degrading soil and water resources (Lottermoser 2003). Open mine pits, tailings ponds, ore stockpiles, and waste rock dumps can all be significant sources of pollution, primarily heavy metals (EPA 2003).

A large number of minerals with varying chemical properties result from AMD, including iron oxides, hydroxides, oxyhydroxides, and sulfates (Nordstrom 1982). These minerals are indicative of the chemical conditions in which they form (Alpers et al. 1994; Bigham 1994; Nordstrom et al. 1978). For example, jarosite $((K,H_3O, Na)Fe_3(SO_4)_2(OH)_6)$, generally forms between pH 1.5 and 3.0 and with SO_4^{2-} concentration greater than 3000 mg/L, while goethite (α-FeO(OH)), generally forms at pH less than 6 and with SO_4^{2-} concentration greater than 1000 mg/L (Montero et al. 2005). These minerals have unique chemical and structural properties that make them identifiable using diffuse reflectance spectroscopy in the visible to short wave infrared (VSWIR) range (Cloutis et al. 2006; Crowley et al. 2003; Crowley et al. 2006). Hence, mineral maps using spectral reflectance can be used to identify the most acidic "hot spots" at mine waste sites.

Hyperspectral remote sensing (200 or more spectral bands) has been widely used to characterize mine waste environments (Swayze et al. 2000; Montero et al. 2005; Riaza et al. 2012; Kopachova 2014). These studies employ an assortment of spectral datasets, varying in spectral and spatial resolutions. They focus on mapping the unique mineralogy of AMD, and subsequently assign "high" and "low" priority contamination zones to mine waste surfaces. Most notably, Swayze et al. (2000) demonstrated the effectiveness of remotely sensed hyperspectral data for the rapid screening of waste rock piles at the California Gulch Superfund site, which accelerated remediation efforts by two years and saved the U.S. government millions of dollars.

With advancements in remote sensing technology and the introduction of new satellite sensors, there is a constant need for more refined methods in mapping mine waste environments. Understanding the limits of current and proposed imaging spectrometers will further the progress of remote sensing based environmental monitoring. This study will examine the ability to map AMD minerals on mine waste surfaces at the Leviathan Mine Superfund site with seasonal hyperspectral imagery at varying spatial resolutions. The goals are to 1) identify the mineralogy in dried-out AMD retaining ponds and on aging overburden piles, 2) examine if seasonal AMD mineral variation occurs on these surfaces, and 3) compare the ability to map AMD mineralogy at varying spatial scales.

2. Study Area—Leviathan Mine

The study area is previously described in chapter 1.2 and 2.2. Although parts of the original pit have been graded and contoured, significant wall rock is still exposed. Overburden piles remain along the northern portion of the property and soils with heavy metal toxicity persist, prohibiting complete re-vegetation.

3. Dataset

A total of eight flight images were examined in this study. The commercial airborne hyperspectral sensor ProSpecTIR (http://www.spectir.com/) was flown over Leviathan Mine on 08/17/2007. The sensor provided 356 spectral channels at 5 nm intervals across wavelengths 398 to 2455 nm, with a spatial resolution of 2 meters. The remaining seven images were collected as part of the National Aeronautics and Space Administration (NASA) Hyperspectral Infrared Imager (HyspIRI) preparatory mission. The mission used NASA's Airborne Visible/Infrared Imaging Spectrometer (AVIRIS) flown on the ER-2 aircraft for a series of seasonal (spring, summer, fall) data collections over two years (2013-2014). Collection dates are summarized in Table 1. AVIRIS provided 204 spectral channels at 10 nm intervals across wavelengths 366 to 2496 nm, with a spatial resolution of 15 meters. In addition to the eight flight images, two supplementary images were produced by the HyspIRI preparatory mission team at the Jet Propulsion Laboratory (JPL) in Pasadena, California. These supplementary images were derived from the 09/19/2013 image by resampling reflectance for a simulated 30 and 60 meter spatial resolution product. These products were resampled using Gaussian weighted sampling with 30 or 60 meter full-width half-maximum, over a 90 meter by 90 meter, or 180 meter by 180 meter area, respectively. Noise approximating a HypsIRI VSWIR noise function was added to the resampled images.

Field data was collected with the ASD FieldSpec Pro spectrometer, which provided 2151 spectral channels at 1 nm intervals across wavelengths 350 to 2500 nm. Field visits occurred about one to four weeks before or after the corresponding flight date (between 09/2013-11/2014). Additionally, several field visits occurred in 2015. Reflectance was collected using both the ASD contact probe with halogen light source, and the pistol grip option. Field data collection was focused on taking transects of the pond liner surfaces, which were exposed by the declining water level. Single point and short transects were taken on the overburden waste piles as well, however, access was limited as the piles were steeply sloped and unstable. Sediment and rock specimens were collected at each field visit and spectrally analyzed in the lab immediately after collection and additionally after specimens were sufficiently air dried.

AMD water in the evaporation ponds was monitored between 05/2014-09/2015. Field pH was measured with a Double Junction Waterproof pHTestr 20, calibrated using pH 4 and 7 buffer solutions. Pond water was sampled on two occasions and analyzed for general water chemistry parameters at SEM, Inc. (Reno, NV), as described in chapter 2.

Airborne Data Acquisition Date	Field Data Acquisition Date	Water Level in Ponds	Spatial Resolution (pixel size)	Spectral Sampling (number of bands)	Sensor
08/17/2007	--	Nearly empty	2 m	356	ProSpecTIR
05/02/2013	--	Full	15 m	204	AVIRIS
06/04/2013	--	Full	15 m		
09/19/2013	10/31/2013	Ponds 2 empty; Pond 1 low	15 m		
09/19/2013	10/31/2013	Ponds 2 empty; Pond 1 low	30 m		
09/19/2013	10/31/2013	Ponds 2 empty; Pond 1 low	60 m		
04/10/2014	04/24/2014	Full	15 m		
06/02/2014	05/22/2014	Full	15 m		
09/09/2014	08/08/2014	Ponds 2 empty; Pond 1 low	15 m		
11/17/2014	10/09/2014	Ponds 2 empty; Pond 1 full	15 m		

Table 1. Imagery summary

4. Methods

All image processing was completed using the software package Environment for Visualizing Images (ENVI) version 5.1. The ProSpecTIR image was corrected for atmospheric effects using the ENVI Fast Line-of-sight Atmospheric Analysis of Hypercubes (FLAASH) function. AVIRIS images were calibrated and corrected for atmospheric effects by the HypsIRI preparatory mission team.

All images were subset to include only the mine area (about 11 square km box). Pixels containing vegetation were masked using the Normalized Difference Vegetation Index (NDVI) with a threshold of 0.5 (Tucker 1979). Expert analysis was performed on all images focusing on identifying spectral variations between the pond liner surfaces and the overburden piles. United States Geological Survey (USGS) spectral libraries were used to visually identify different minerals within the scenes (USGS 2013). Reference mineral spectra from the USGS library included: copiapite, gypsum, anhydrite, jarosite, ammoniojarosite, alunite, schwertmannite, hematite, magnetite, maghemite, goethite, lepidocrosite, ferrihydrite, and kaolinite.

The decorrelation stretch (DCS) technique (Gillespie 1992) was used to enhance contrast at specific wavelengths and provide emphasis on major compositional variation in materials. DCS channels were selected around wavelengths 437 nm and 911 nm, which are diagnostic absorption bands for jarosite (Crowley et al. 2003). Additionally, a band ratio positioned around the broad characteristic absorption feature of iron-bearing minerals between 750-910 nm (Hunt and Ashley 1979), was used to identify AMD "hotspots" throughout the seasonal images. The ratio was calculated by the division of the reflectance value of AVIRIS band 40 (725 nm) by band 63 (947 nm). This ratio was similar to those presented in Mielke et al. (2014), which were used to map iron oxides as a proxy for mine waste contamination.

ENVI's Spectral Hourglass Wizard classification function was employed to produce mineral distribution maps. The Spectral Hourglass Wizard function used a series of operations (MNF, PPI, n-D, SAM) to extract the most spectrally unique pixels within the dataset and map their locations (Kruse 1999). First, the Minimum Noise Fraction (MNF) transform identified the dimensionality of the data, segregated noise, and partitioned data so that only channels which contained variance were used in subsequent processing. Reflectance values from each channel were transformed into eigenvalues in a matrix space, and ordered according to decreasing signal-to-noise-ratio (SNR). Based on the MNF results, lower-order MNF bands were discarded. In the ProSpecTIR image, the first 43 MNF bands were selected for further processing. In the AVIRIS images, the first 25 MNF bands were selected. These bands were then used in the Pixel Purity Index (PPI), which identified the most spectrally pure or extreme pixels. Extreme pixels corresponded to unique materials (endmembers). The n-Dimenional scatterplot was used to visualize the clustering distribution of extreme pixels. Finally, the Spectral Angle Mapper (SAM) algorithm was used to classify all pixels in each image into the previously defined endmember classes. In vector space, SAM compared the angle between the endmember spectrum vector and each pixel spectrum vector. Smaller angles represented closer matches to endmember spectrum. The maximum angle was set at 0.2 radians in all images.

Complete mineral maps were produced for the September images, when the ponds were mostly dried out and pond liner surfaces could be fully mapped.

5. Results
    a.   Field Data

Field photos of the pond liner surfaces are presented in Fig. 1-3. Field spectra from the exposed Pond 2 North and 2 South surfaces are summarized in Fig. 4. These surfaces did not vary significantly throughout the sampling date range. Using USGS spectral libraries for guidance, jarosite was visually identified as the exclusive mineral present on the pond liner surfaces. Diagnostics features included: absorption bands typical of crystal field transitions in ferric iron at 437 and 911 nm, with a weak shoulder

at 650 nm; absorption bands related to vibrational processes in hydroxyl and absorbed water at 1467, 1849, and 1936 nm; and a doublet feature related to Fe-O-H vibration modes at 2264 nm (Crowley et al. 2003). Additional features at 675 and 1170 nm occurred only in the 04/24/14 (Fig. 4b) and 10/09/14 (Fig. 4d) spectra. The sharp feature at 675 nm was likely due to chlorophyll-a (chl-a) absorption from biomass coatings on pond sediments (Campbell and Wynne 2011). This feature was absent in dried out sediment and prominent in moist sediment adjacent to standing water. The 1170 nm feature was likely due to water absorption (Cloutis et al. 2006). Finally, a shallow feature at 1775 nm occurred only in the 04/24/14 (Fig. 4b) and 10/09/14 (Fig. 4d) spectra, which is a diagnostic feature of alunite related to a combination of the OH fundamental stretch with the first overtone of the Al-OH bend (Cloutis et al. 2006). Overall, the spectra in Ponds 2 North and 2 South were consistent throughout the sampling range and were classified as jarosite, with minor variations in the strength of absorption features due to the presence of absorbed water and the abundance of jarosite.

Field spectra from the exposed Pond 1 surface is summarized in Fig. 5. Considerably more spectral variation was observed in Pond 1 on 10/09/14, when the water level was quite low and surplus lime had been deposited onto the north shore. Spectra were complex and could not be classified as one discrete mineral using VSWIR reflectance alone. Rather, mixtures of iron oxides, hydroxides, oxyhydroxides, and sulfates (including jarosite, copiapite, goethite, hematite, ferrihydrite, alunite, and gypsum) were deduced using visual comparison to the USGS spectral library. Spectra in Pond 1 were characterized by: low reflectance between 400 and 700 nm, which was linked to the intense absorption band centered in the UV region near 250 nm related to charge transfer between ferric cations and adjacent oxygen anions (Sherman and Waite 1985); a broad absorption near 900 nm, which was linked to crystal field absorption of the ferric cation (Crowley et al. 2003); and absorptions of various strengths near 1200, 1400, and 1900 nm, which were linked to water absorptions commonly seen in evaporate minerals (Cloutis et al. 2006; Crowley 1991).

Field spectra of biomass observed in the ponds are summarized in Fig.6. Algae was identified in all ponds with standing water throughout the sampling date range. Algal biomass was clustered mainly around the inlet pipes and along shore lines. Biomass was spectrally characterized by deep absorption in the red wavelengths (centered at 675 nm) and a rapid increase in reflectance in the near infrared (NIR) region. This behavior was due to the spectral properties of chl-a contained in biomass, and commonly referred to as the "red edge" (Campbell and Wynne 2011).

Field spectra from the overburden piles are summarized in Fig. 7. The dominant mineral present was kaolinite, identified by the very strong and characteristic hydroxyl bands near 1400 and 2200 nm (Hunt and Salisbury 1970). The weaker bands in the visible range were indicative of ferric iron (Hunt and Salisbury 1970). Particularly, the absorption bands at 675 and 939 nm, related to paired excitations of magnetically coupled ferric cations, are diagnostic of goethite (Sherman and Waite 1985).

Finally, field spectra from the sludge pond is summarized in Fig. 8. Gypsum was the dominate mineral identified, with trace amounts of iron sulfates. Diagnostics features included: a weak band near 1000 nm due to a combination of overtones of the O-H stretching and the H-O-H bending fundamentals; the more pronounced feature at 1200 nm due to a combination of the H-O-H bending fundamental and the first overtone of the O-H stretch; a doublet at 1490 due to the first overtone of the O-H stretching fundamental; a feature near 1740 nm due to combinations of the fundamental H-O-H bend and fundamental O-H stretch; and a feature near 2200 nm due to the fundamental O-H stretch (Crowley 1991). Variable absorption features between 400-900 nm were again linked to ferric iron.

Pertinent water chemistry results are summarized in Tables 2 and 3. Pond 1 remained relatively constant from spring to fall, while Pond 2 became more acidic and more concentrated in iron over the summer.

Location	05/22/2014	08/08/2014	10/09/2014	05/14/2015	09/16/2015
Pond 1 (at inlet)	2.65	2.91	2.97	2.73	2.79
Pond 2 North	2.59	2.25	2.23	2.26	2.5
Pond 3	3.72				

Table 2. Field pH

Location	05/22/2014		10/09/2014		
Pond 1 (at inlet)	460		530		
Pond 2 North	310		2215		
Pond 3	8				

Table 3. Total Fe (mg/L) from laboratory analysis (SEM Inc.)

b.   DCS, Band Ratio

The DCS method was useful as an initial assessment of surface type. The DCS placed at wavelengths 590, 529 and 483 nm produced a particularly good visual of secondary iron mineral variability and distribution. Iron mineral "hotspots" were identified on the pond liner surfaces and are denoted by red and yellow shades in Fig. 9. Similarly, the band ratio was a useful metric to identify the most intense absorption of iron bearing minerals. Again, "hotspots" were identified in the pond liners, as well as on several small regions of the overburden piles (Fig. 10).

c.   Spectral Hourglass Wizard

Five main categories of mine waste surfaces were classified. Those included 1) AMD water surface, 2) wet pond sediment, 3) iron sulfates, 4) iron hydroxides and clays, and 5) gypsum. Spectral

curves of these endmember categories from all images are summarized in Fig. 11-16. The endmembers maps are presented in Fig. 17-18. The color coded variation within each endmember group indicates differences in strength of diagnostic absorption features.

Overall, the 2 meter image (2007) most accurately mapped the widest range of surfaces (Fig. 17). Three different depths of pond water were identified (Fig. 11a). The narrow regions of moist sediment bordering standing water, which supported the largest algal populations, were precisely identified (Fig. 12a). A unique white sulfate mineral was identified along the north shore in Pond 1 (Fig. 13a). Absorption features in this material occurred near 990, 1190, and 1490 nm, which are similar to those in gypsum and are characteristic of efflorescent evaporates (Crowley 1991). Additional features occurred in the white sulfate mineral between 500 and 650 nm, and were likely due to small amounts of ferric or ferrous sulfate hydrates, or minor Fe substitution in the Mg hydrates. There is no precise analog in any spectral library and field samples were not collected in 2007. The spectral signature was not identified in the 2013 and 2014 field/airborne data.

Gypsum with varying amounts of iron hydroxides were identified in the sludge pond, in discrete regions in Pond 1 and Pond 3, and in small clusters throughout the overburden piles (Fig. 14a). Several variations of jarosite were identified in all of the ponds (Pond 1, Pond 2 North, Pond 2 South, Pond 3, and the sludge pond) (Fig. 15a). The variations exhibited differing absorption depths at 437 and 911 nm. Except for a few pixels scattered along the disturbed surfaces, "pure" jarosite was not readily identified on any surface outside of the pond liners (Fig. 17). Mixtures of iron hydroxides and kaolinite were identified on the overburden piles and on disturbed surfaces (Fig. 16a). These endmembers varied in iron mineral abundance. The coloring grade of "Overburden Fe Hydroxides/Clays" in Fig. 17 assigned classes with the deepest iron absorption features to the darkest shades of red.

In general, the 15 meter images (2013, 2014) (Fig. 18a-b) identified all of the same endmembers as the 2 meter image (2007). Standing water and wet sediment were identified in each image (Fig. 11b-c, 12b-c). The unique white Mg sulfate was not identified in Pond 1, and this was not surprising as these soluble salts can mobilize quickly during natural precipitation events (rain, snow). Gypsum in Pond 1 and the sludge pond were classified in the 2014 image, while no gypsum pixels were classified in the 2013 image (Fig. 14b-c). However, using expert pixel by pixel analysis, two pixels of gypsum were identified in the sludge pond in the 2013 image. Several variations of jarosite were identified in Ponds 1, 2 North, and 2 South, however, not in Pond 3 (Fig. 15b-c). Several pixels of jarosite were classified on the overburden piles along the southeastern border of the mine (Fig. 18a-b). The remaining area of overburden piles and disturbed surfaces were classified as mixtures of iron hydroxides and kaolinite, again with varying iron mineral abundance (Fig. 16b-c).

The 30 meter image identified the same endmembers as the 15 meter 2013 image, but with less accurate spatial boundaries (Fig. 18c). Fewer variations of each classification were identified. The 60 meter

image identified only jarosite and iron hydroxides/kaolinite mixtures (Fig. 18d). Again, fewer variations were identified and the spatial boundaries were very coarse.

The success rate of each image in mapping these five categories are summarized in Table 4.

Endmember	2m (ProSpecTIR 8/2007)	15m (AVIRIS 9/2013)	15m (AVIRIS 9/2014)	30m (AVIRIS 9/2013)	60m (AVIRIS 9/2013)
1) AMD water surface	Y	Y	--	Y	N
2) Wet pond sediment	Y	Y	Y	Y	N
3) Iron sulfates	Y	Y	Y	Y	Y
4) Iron hydroxides/clays	Y	Y	Y	Y	Y
5) Gypsum	Y	Y*	Y*	N	N

Table 4. Endmember classification success rate. *Indicates endmember was not identified with unsupervised SHGW classification, however expert analysis identified several pixels by hand

6. Discussion

The spectral consistency of Pond 2's liner surface is not surprising given the relative consistency of the water chemistry. The speciation of iron minerals in iron sulfide-rich mine water is largely dictated by other constituents present and by the pH and Eh (redox potential) of the water (Langmuir 1997). Given the water chemistry observed during this sampling period, and from supplementary data provided by the Lahontan Regional Water Quality Control Board, pH is consistently between 1.5 and 3.0, and SO_4^{2-} is greater than 3000 mg/L—conditions which should yield jarosite (Fig. 19).

The main difference between the variations of jarosite identified by field spectrometer and airborne image "Pond Iron Sulfate" endmembers are the depth of absorptions at 437 and 911 nm due to ferric iron, and the depth of the water bands at 1400 and 1900 nm (Fig. 4, 15). The depth of an absorption feature is related to the abundance of the absorber and the grain size of the material (Campbell and Wynne 2011). The 9/2014, 15 meter image (Fig. 18b) resolves the best jarosite evolution in Pond 2 North and 2 South. More hydrated jarosite is found in the northeastern corner of the ponds, where some standing water is still present. Jarosite with the deepest ferric iron absorption is found in the middle section of the ponds, where more concentrated AMD evaporated. And finally, the least hydrated jarosite with shallowest ferric iron absorption is found along the southwestern edge of the ponds, which is the first region to be exposed

by a decreasing water level and where AMD water has minimal contact with the pond liner surface. This general jarosite evolution is distinguishable very well in the 2 and 15 meter images, and less so in the 30 and 60 meter images.

Field spectra from Pond 1 on 10/09/2014 show much wider mineral variation than that observed in Pond 2 North and 2 South (Fig. 4, 5). This variation is observable in the 8/2007, 2 meter image (Fig. 17), where jarosite mixtures, gypsum, and Mg sulfates are classified. A large portion of the Pond 1 pixels are also strongly influenced by algae and classified as "Wet Pond Sediment". The robust "red edge" features of the algae mask those of the iron minerals species. This variation is lost in the 15 meter images (Fig. 18a-b) because Pond 1 is only about 5500 square meters in area. Resolving variation in Pond 1 requires much finer spatial resolution (<15 meters).

Jarosite endmembers are also identified in Pond 3 in the 8/2007, 2 meter image (Fig. 17). Although no AMD was stored in Pond 3 during the date range of this study (2007, 2013-2014), AMD and sludge was stored in Pond 3 during the 2006 water treatment season. Sludge from 2006 was stored in Pond 3 until about one month before the 2007 image was collected. The imagery was able to identify remnant jarosite on these surfaces.

The iron hydroxide and clay endmembers are distributed over the overburden piles, disturbed surface, and old pit wall faces (Fig. 17, 18). Additionally, these endmembers are identified along the rims of the evaporation ponds (pond liner surfaces that do not contact AMD water). Direct comparison between the 9/2013 and 9/2014 15 meter images show little variation between seasons (Fig. 18a-b). Because discrete pixels of individual secondary iron minerals are not identified in the disturbed surfaces, recognition of seasonally induced mineral variation between scenes is not possible at this spatial scale. The 15 meter pixels encompass mixtures of acidic jarosite, less acidic goethite (among other iron oxides), and weathering kaolinite. In order to identify seasonal variation, much finer spatial resolution is needed (< 2 meter), which may be achieved with emerging drone technology.

7.   Conclusions

All images in this study (2-60 meter spatial resolution, 204-356 band spectral resolution) were able to differentiate surfaces that had direct contact with AMD and those that did not. Iron sulfates (jarosite) were identified exclusively on the dried pond liner surfaces. Weathering iron hydroxides and clays were identified on the remaining disturbed surface and overburden piles. These two groups of endmembers could be considered "high priority" and "low priority" remediation zones. Additionally, small regions of gypsum were identified in the 2 meter and 15 meter images. The ability to resolve this fine feature was lost in the 30 and 60 meter images. Overall, 2 meter spatial resolution provided the best classification with more endmembers and with more accurate spatial boundaries. The 15 meter images were

comparable with the 2 meter image in endmember identification. The 30 meter and 60 meter images lost the ability to identify small features like the sludge pond and the various hydration states of jarosite in the ponds. Given the results of this study, authors recommend a spatial resolution of at least 30 meters in hyperspectral imagery for the application of environmental monitoring at mine waste sites.

8. Figures
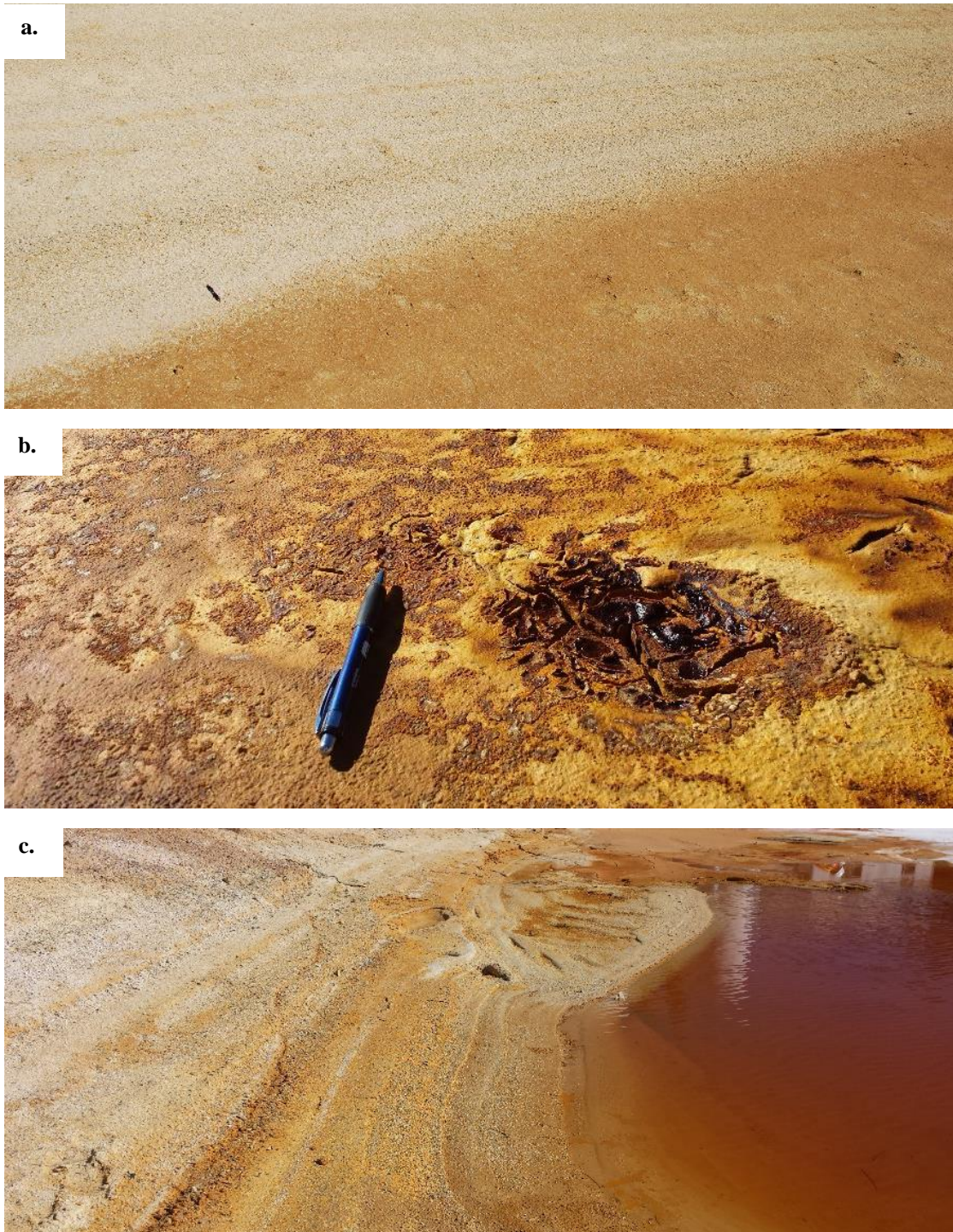

Fig. 1 Field Photos a) Pond 2 South on 10/31/14, b) Pond 2 North on 08/08/2014

Fig. 2 Field Photos a) Pond 2 North on 08/08/2014, b)-c) Pond 1 on 10/09/2014
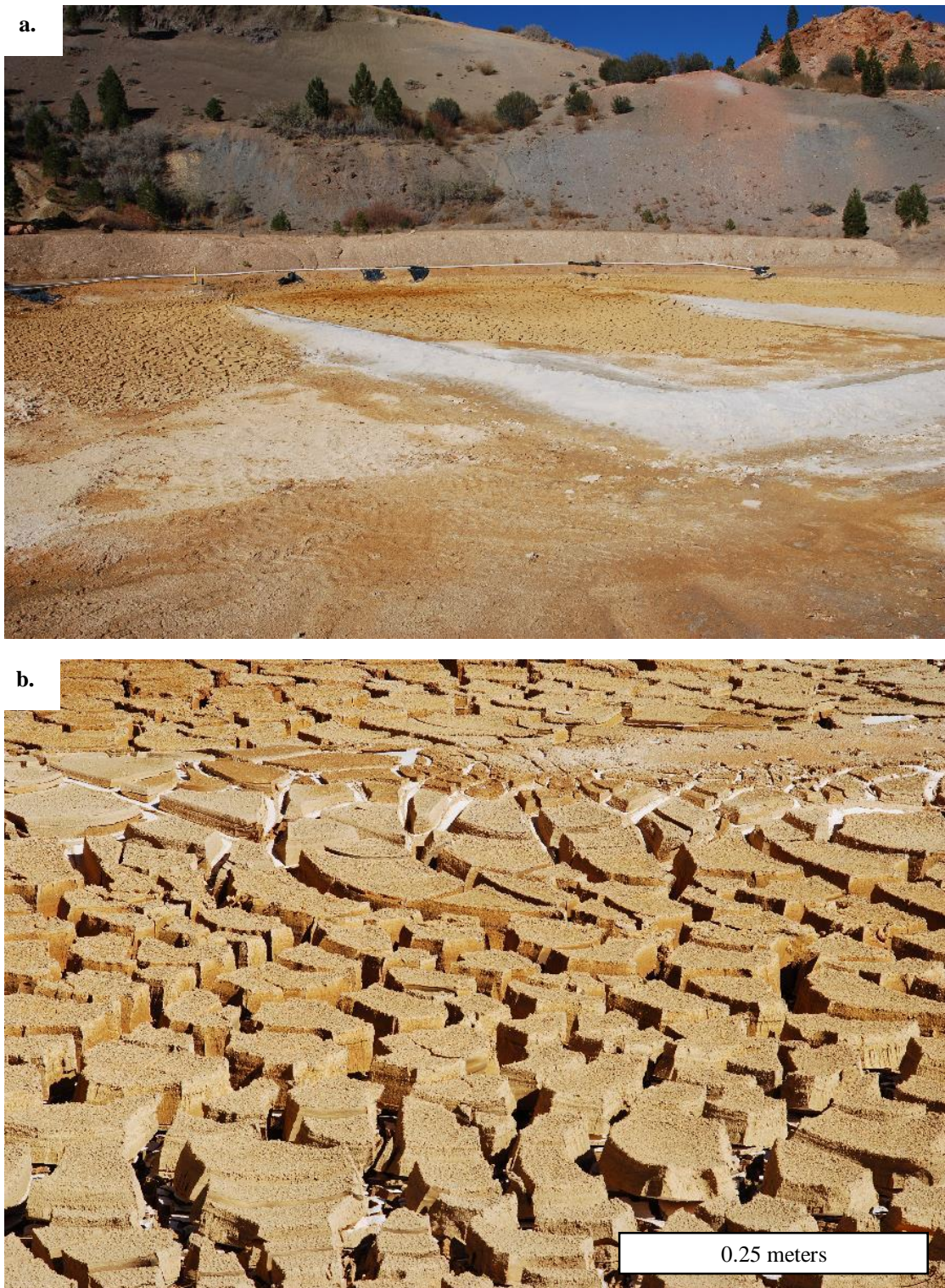
Fig. 3 Field Photo a) The "Pit Clarifier" (sludge pond) on 05/22/2014, and b) on 10/11/2013
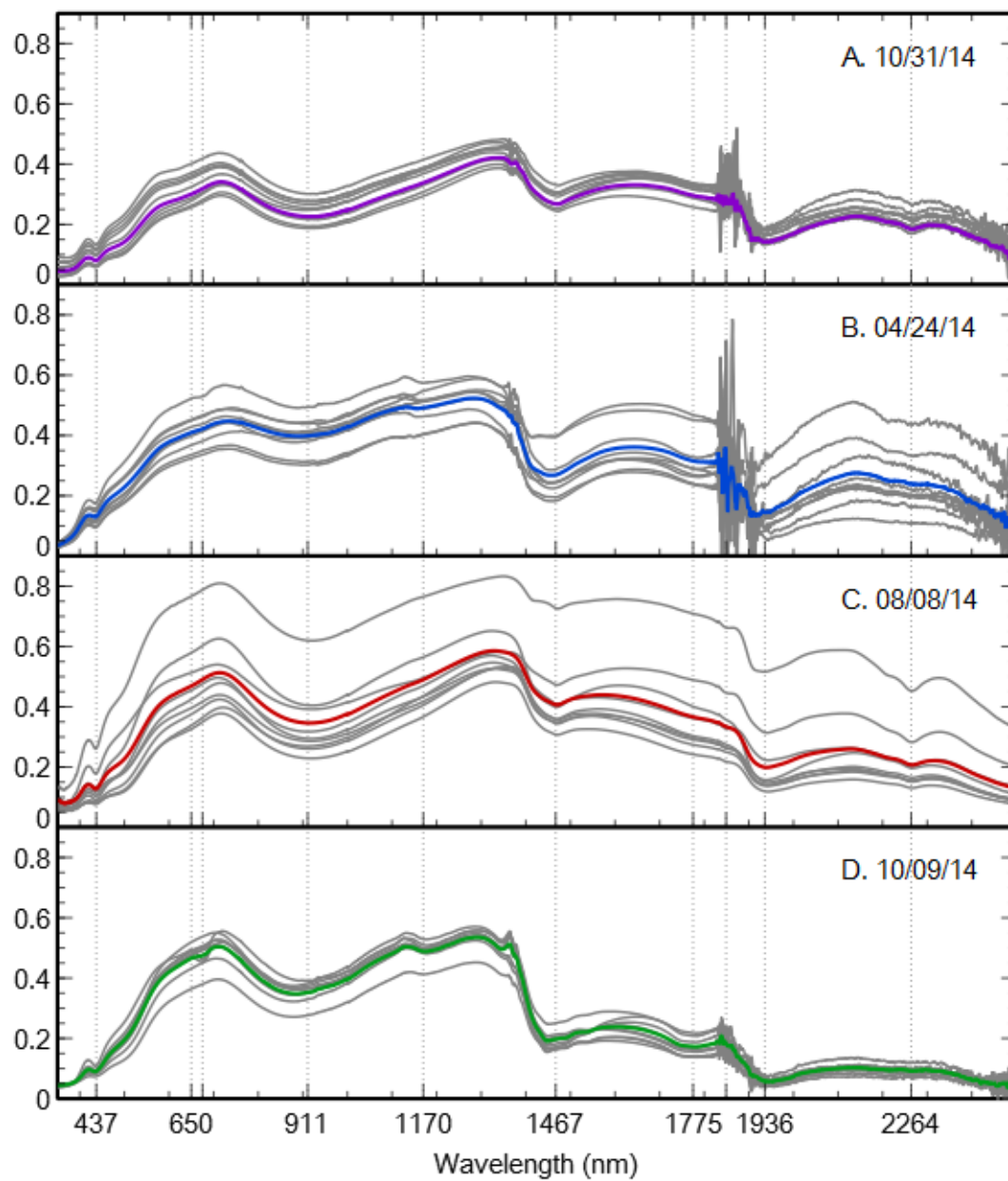
Fig. 4 Field spectra from exposed Pond 2 North and 2 South pond liner surfaces. Colored curves are spectral averages of gray curves. Gridlines at 437, 650, 675, 911, 1170, 1467, 1775, 1849, 1936, and 2264 nm
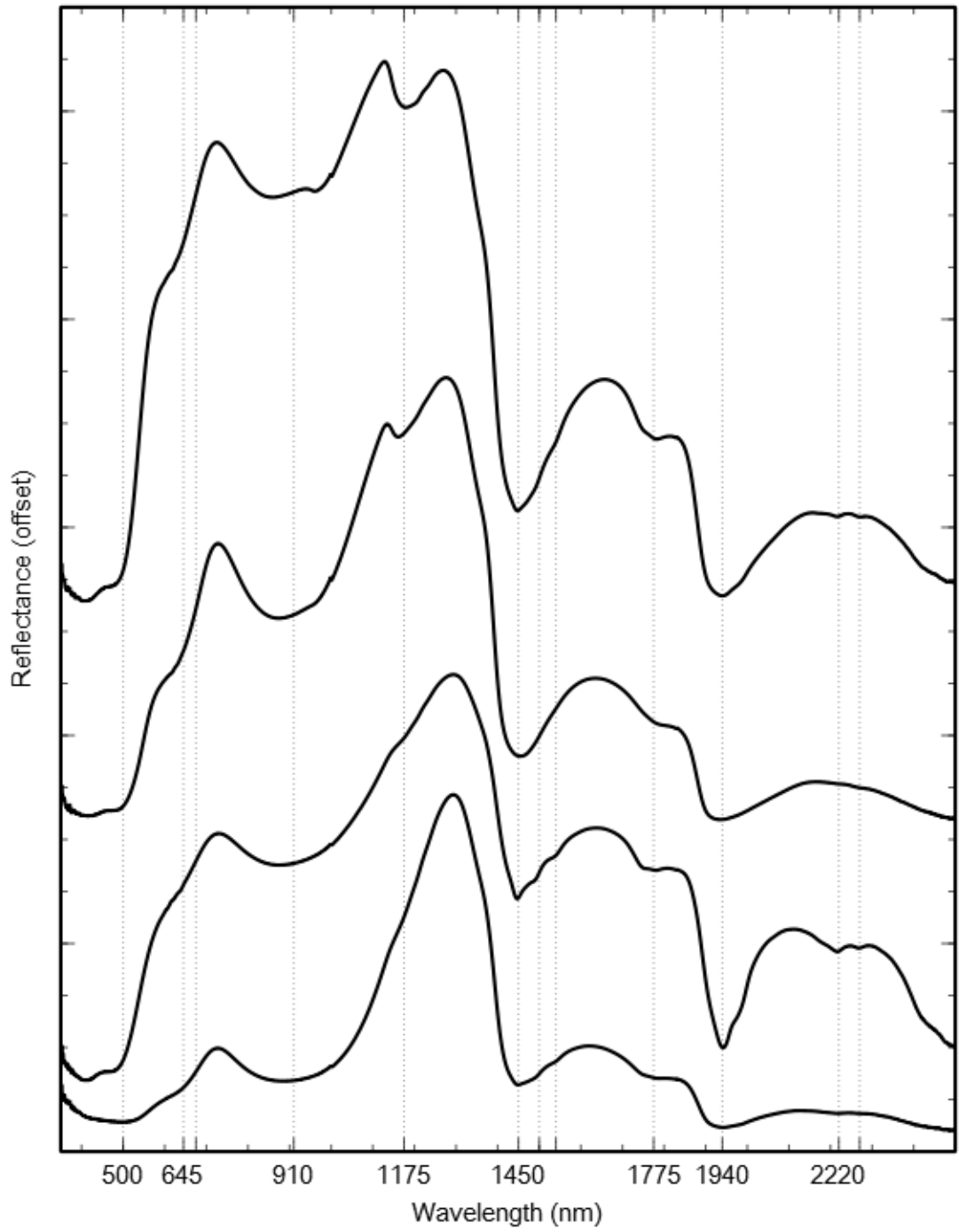
Fig. 5 Field spectra from exposed Pond 1 liner surface collected on 10/09/14. Gridlines at 500, 645, 675, 910, 1175, 1450, 1500, 1540, 1775, 1940, 2220, and 2270 nm
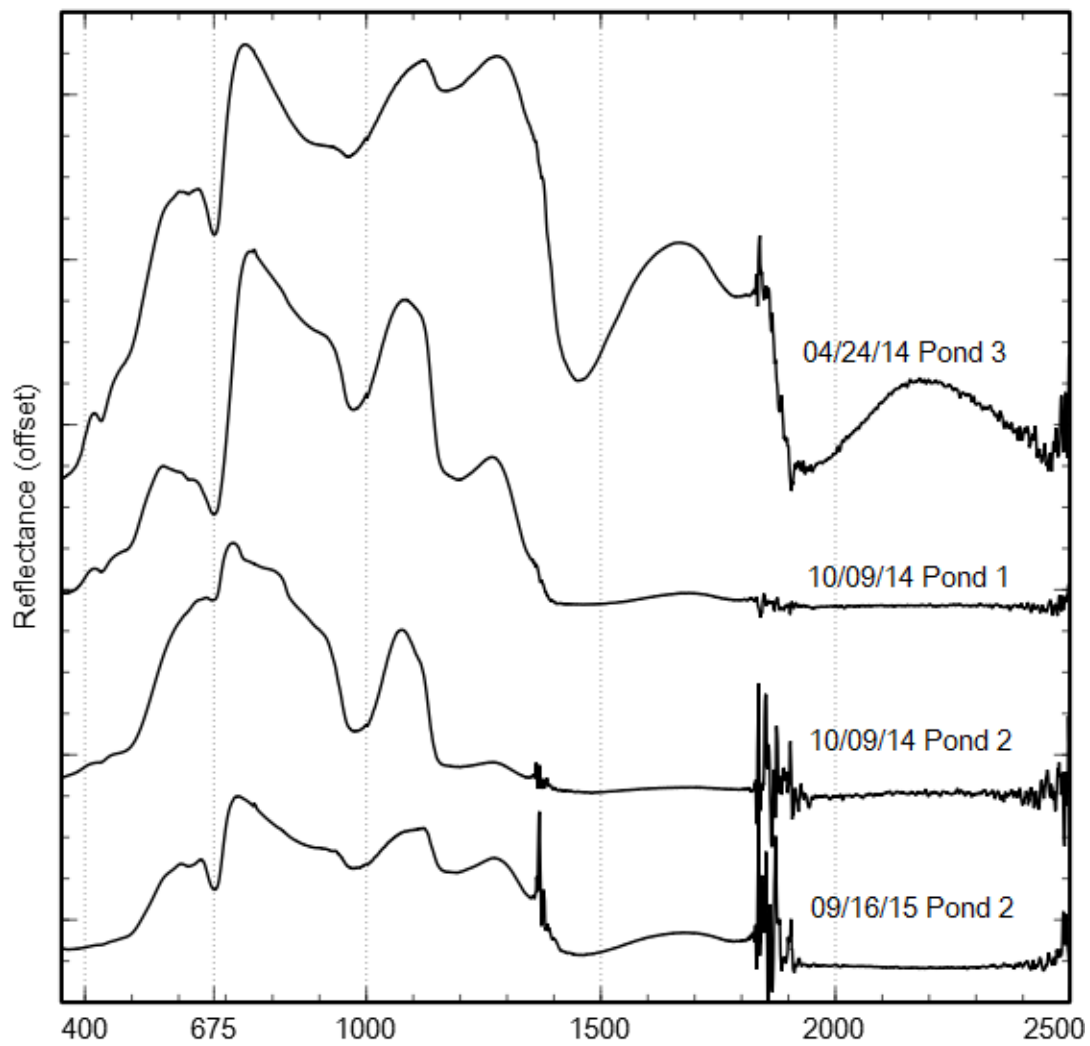
Fig. 6 Field spectra of algae coated sediment. Gridlines at 400, 675, 1000, 1500, 2000, and 2500 nm
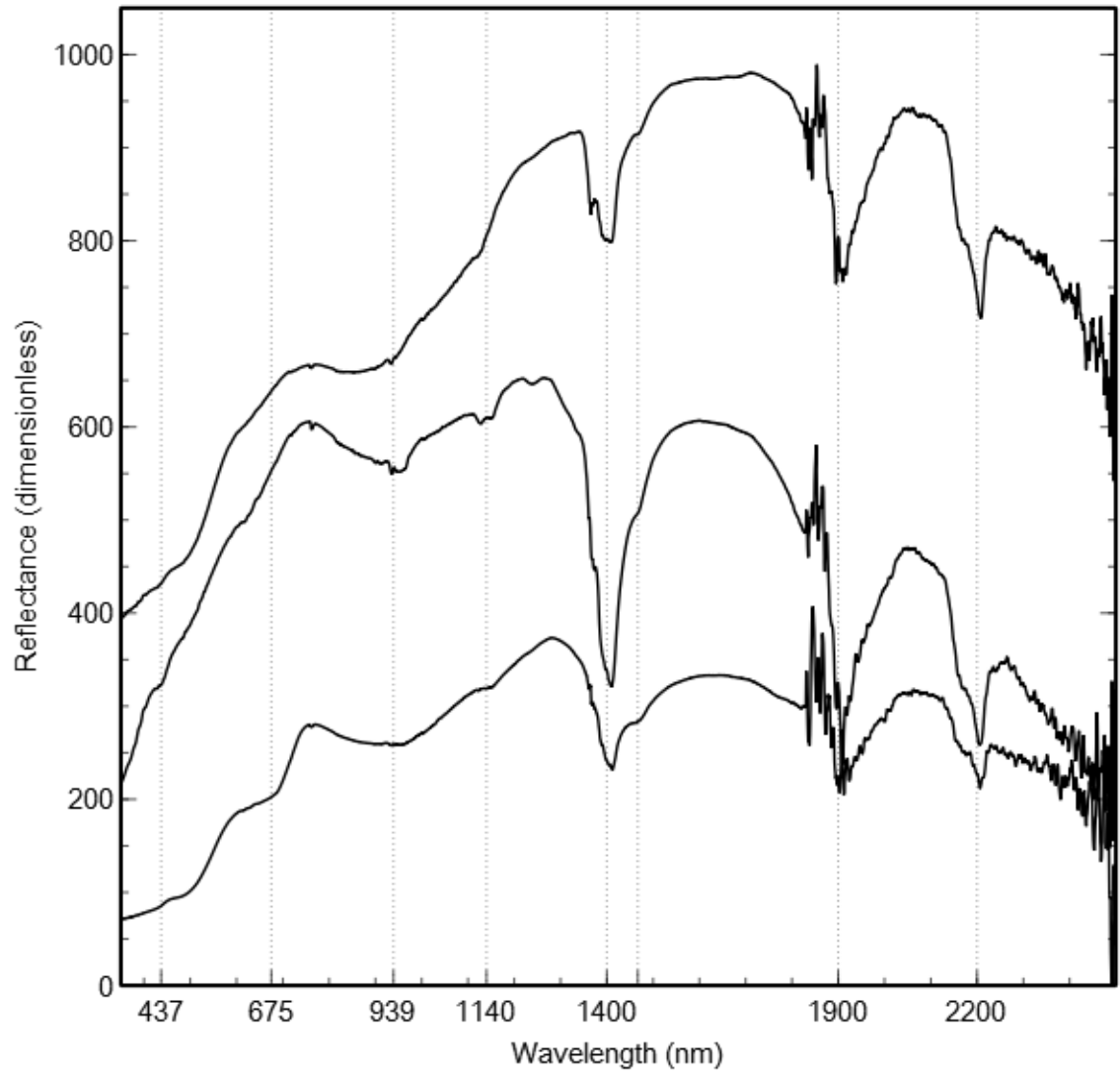
Fig. 7 Field spectra from overburden piles and disturbed surfaces collected on 09/16/15. Gridlines at 437, 675, 939, 1140, 1400, 1467, 1900, and 2200 nm
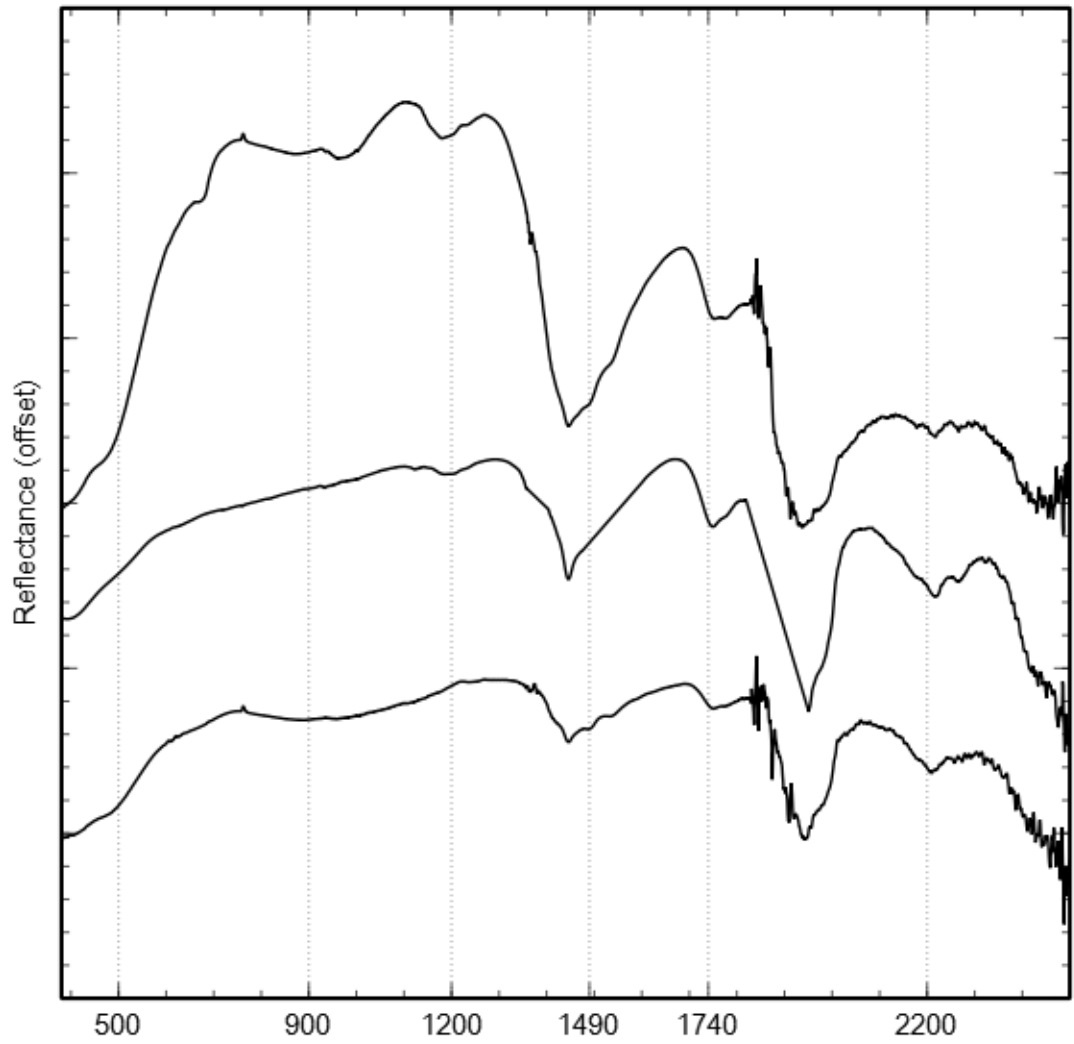
Fig. 8 Field spectra from the "Pit Clarifier" (sludge pond) collected on 10/09/2014 and 10/31/2013. Gridlines at 500, 900, 1200, 1490, 1740, and 2200 nm
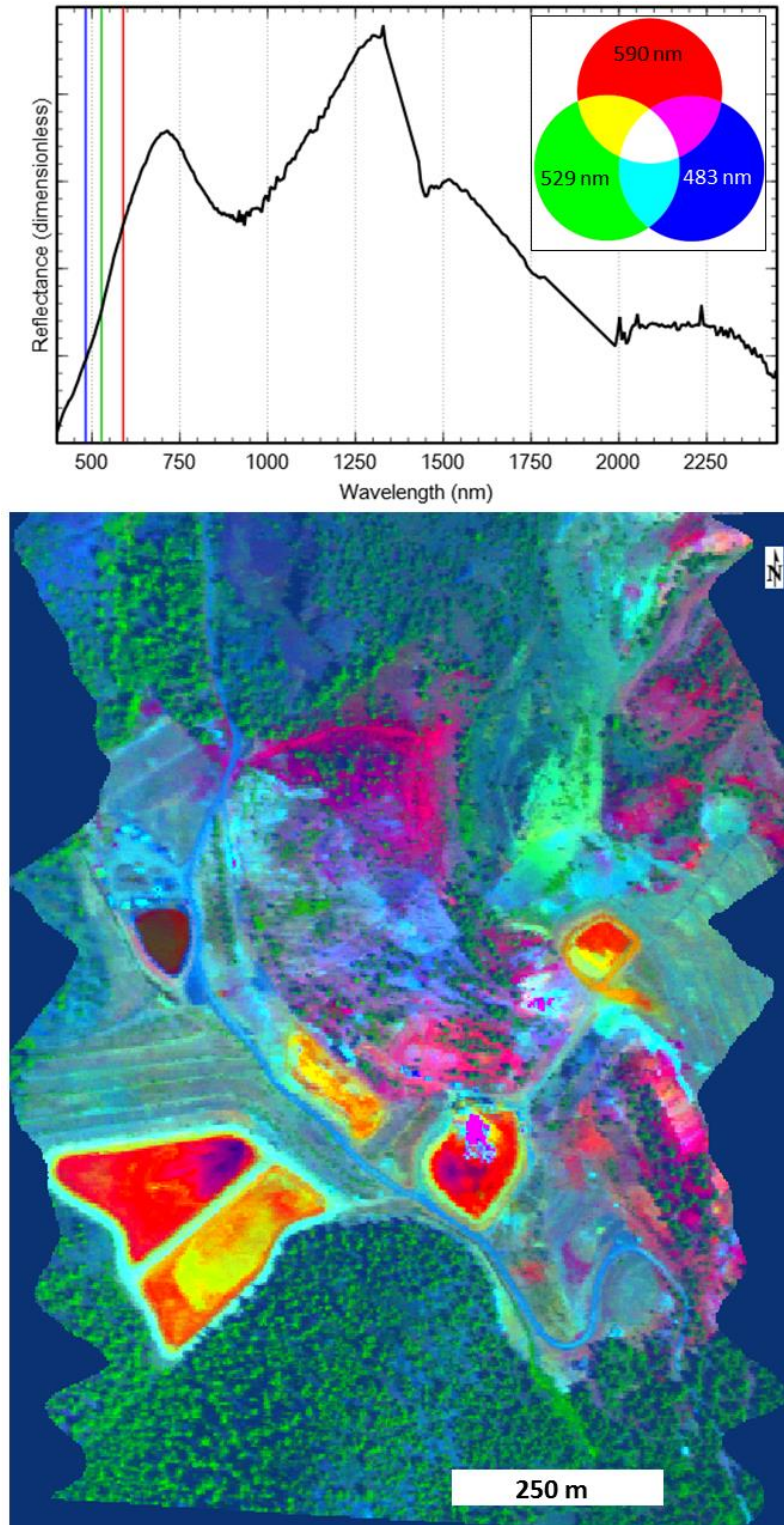
Fig. 9 DCS from 2007 ProSpecTIR image illustrating spectral variation in iron minerals. Band assignments: Red: 590 nm, Green: 529 nm, Blue: 483 nm. Red and yellow shades indicate pixels are strongly influenced by iron minerals. Sample pixel spectra is from the center of dried out Pond 2 North
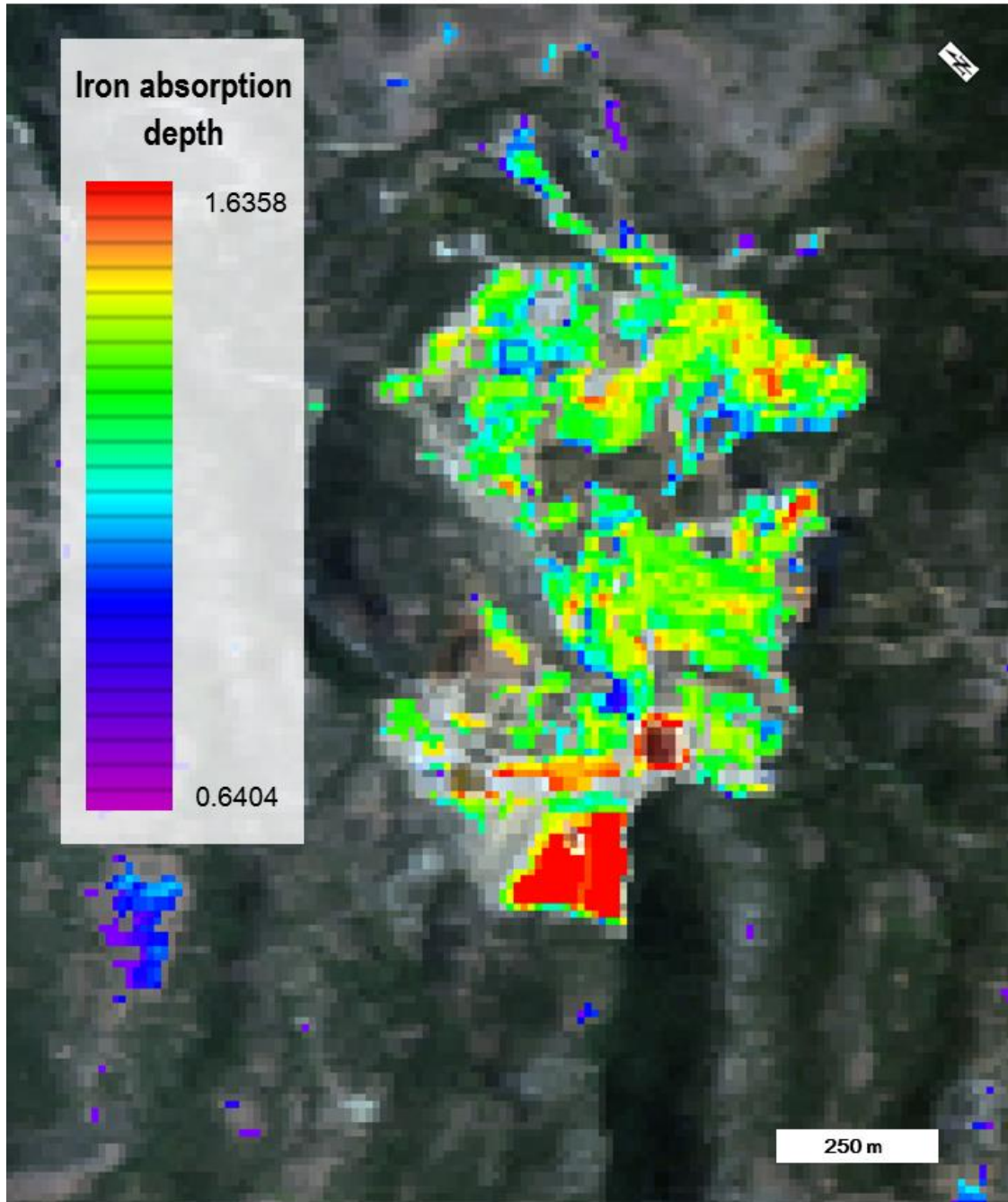
Fig. 10 Iron Absorption Depth from 9/2013 AVIRIS image. Ratio = R_{b40} / R_{b63}, where R = reflectance value, b40 = 725 nm, b63 = 947 nm. Red pixels indicate the deepest iron absorption
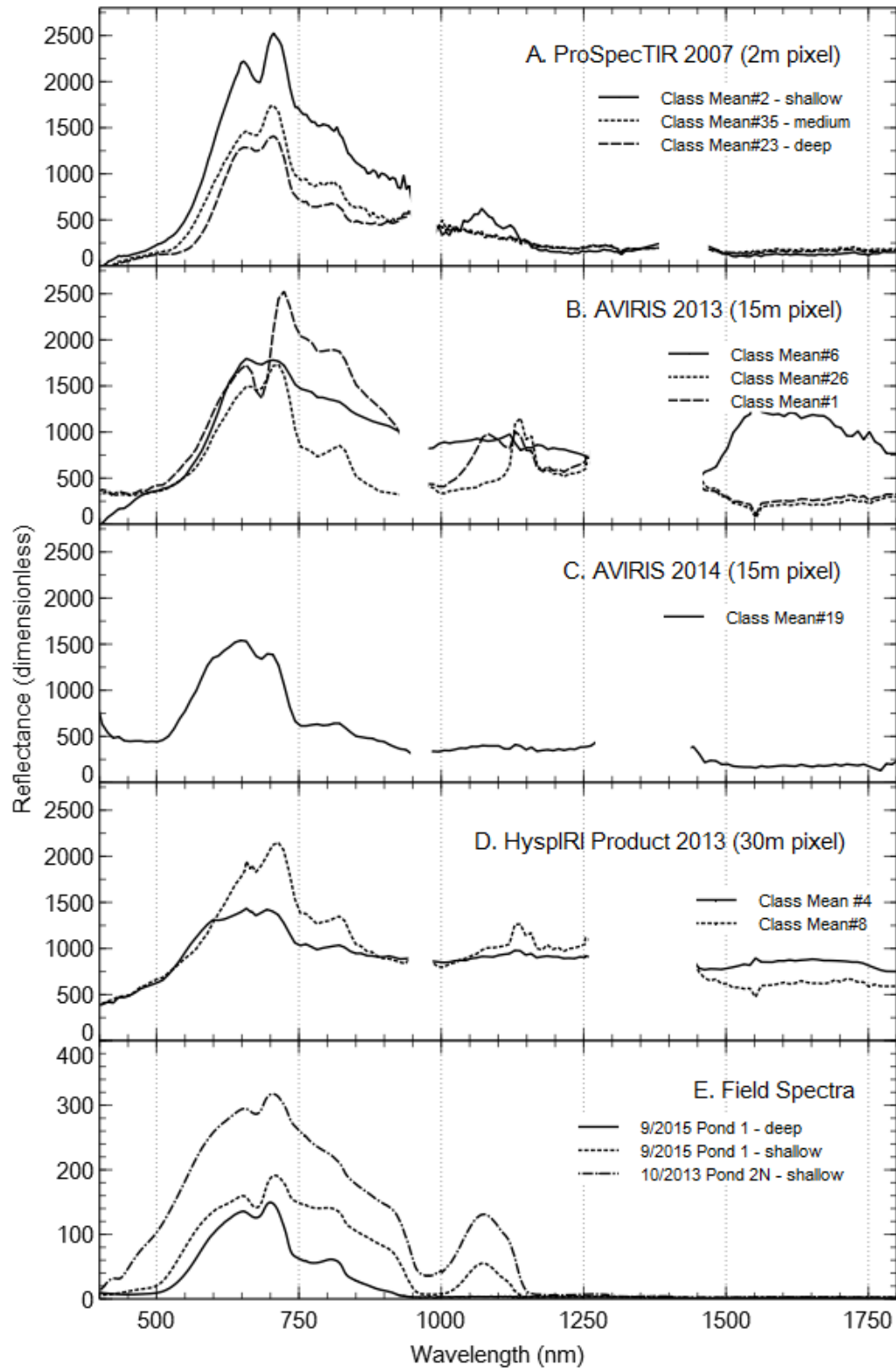
Fig. 11 Pond water endmembers
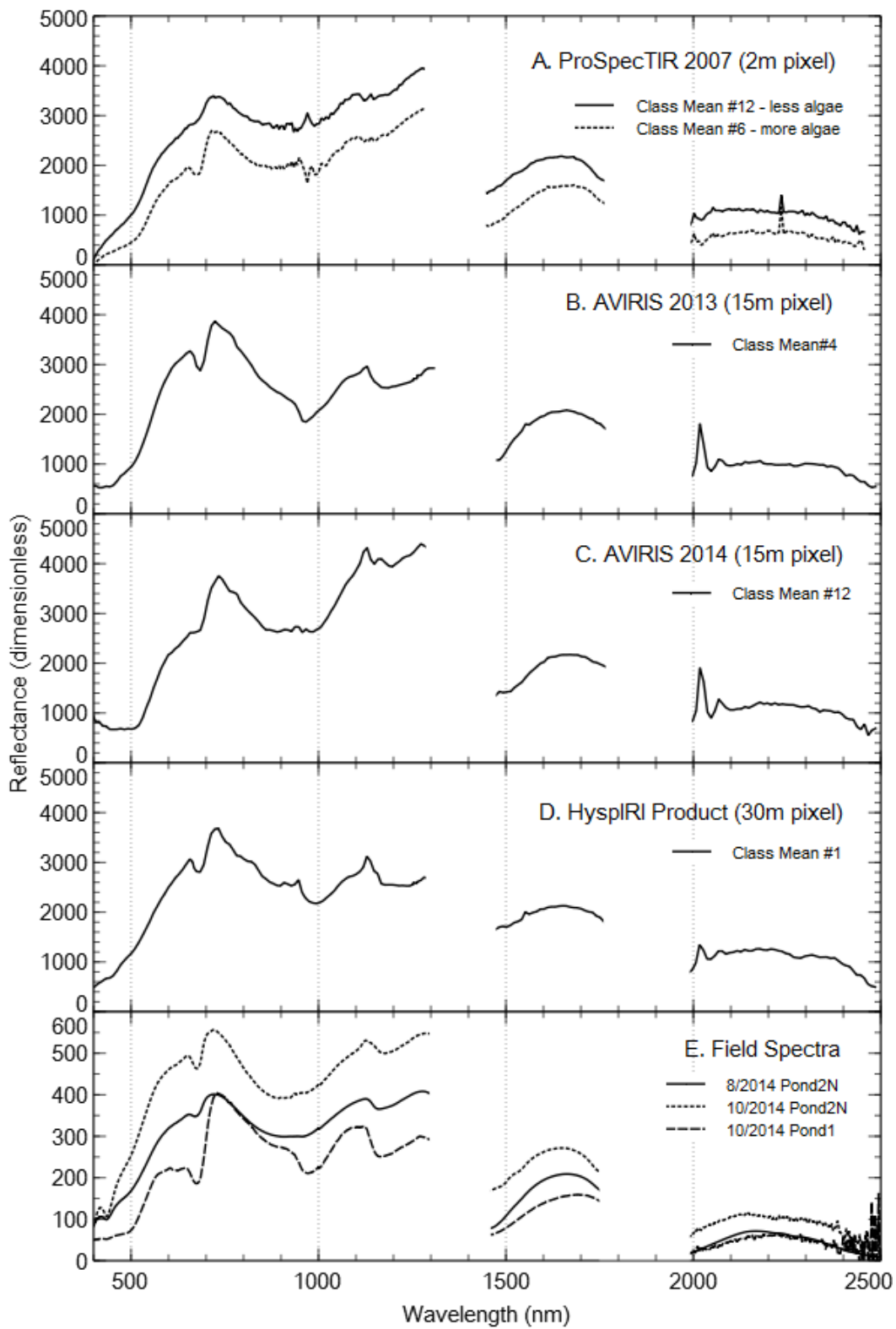
Fig. 12 Wet sediment endmembers
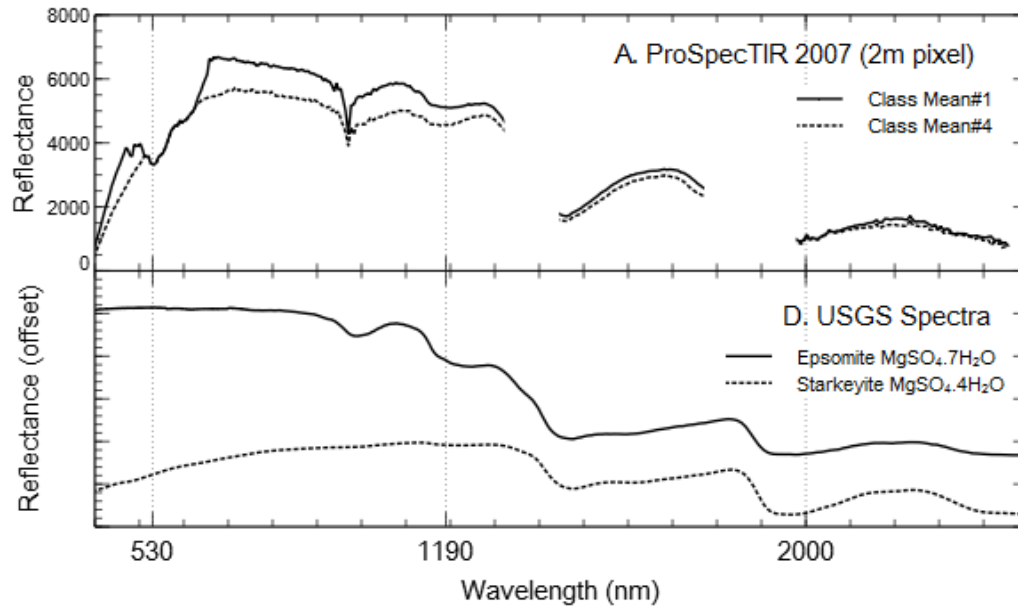
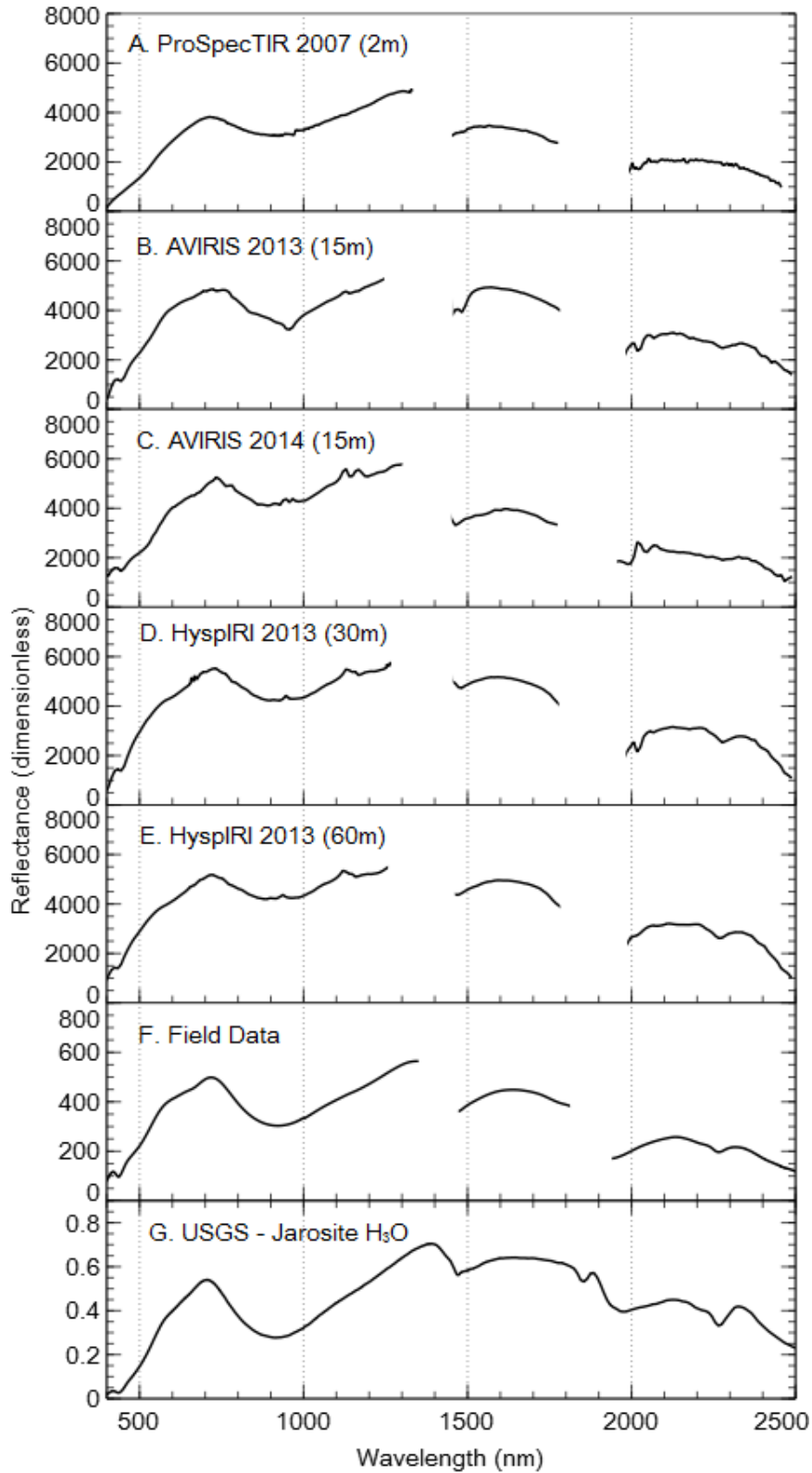**Fig. 13** Magnesium sulfate endmembers
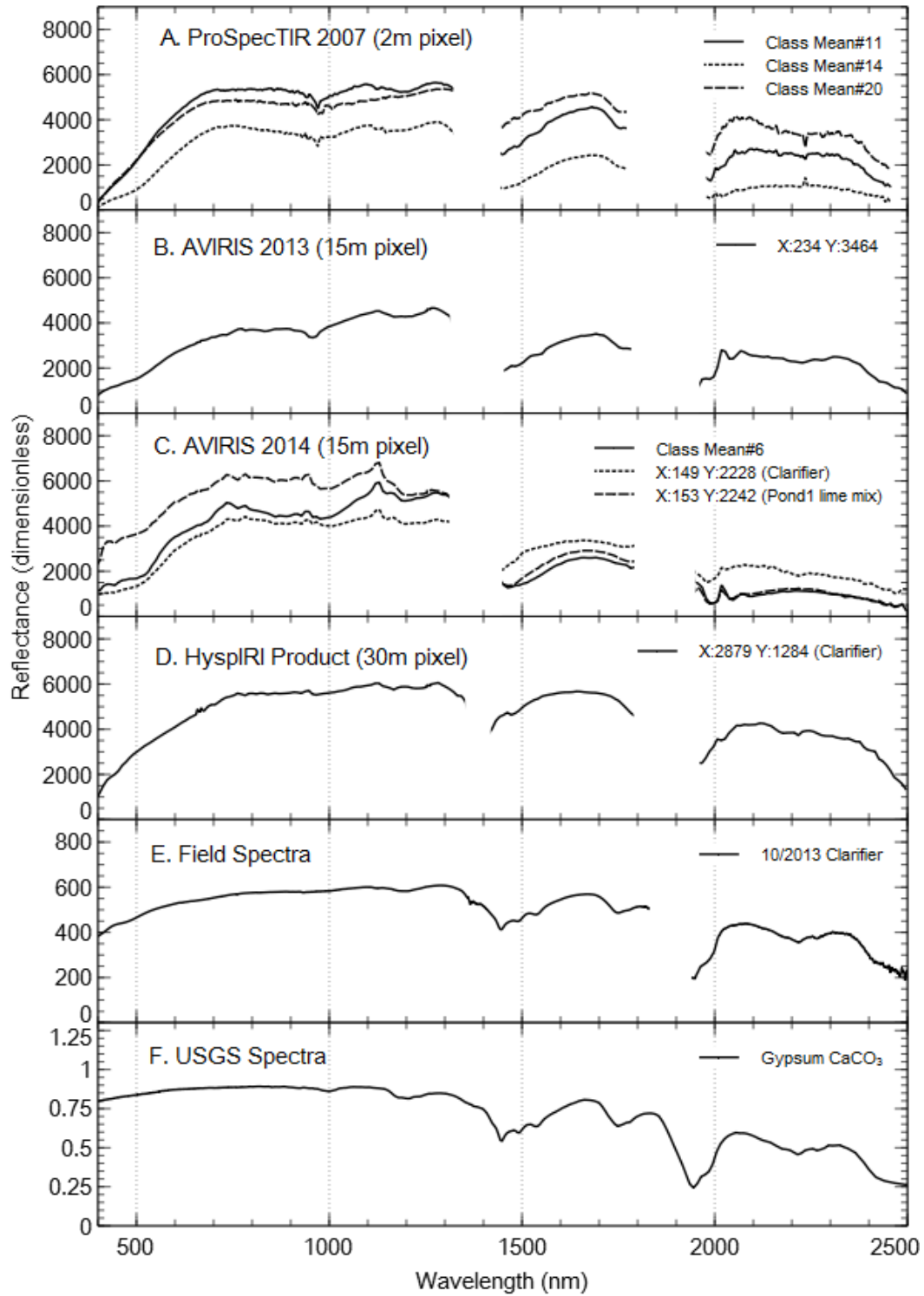
Fig. 14 Gypsum endmembers

Fig. 15 Pond iron sulfate endmembers. Plotted curves are spectral averages of endmembers within the class "pond iron sulfates"
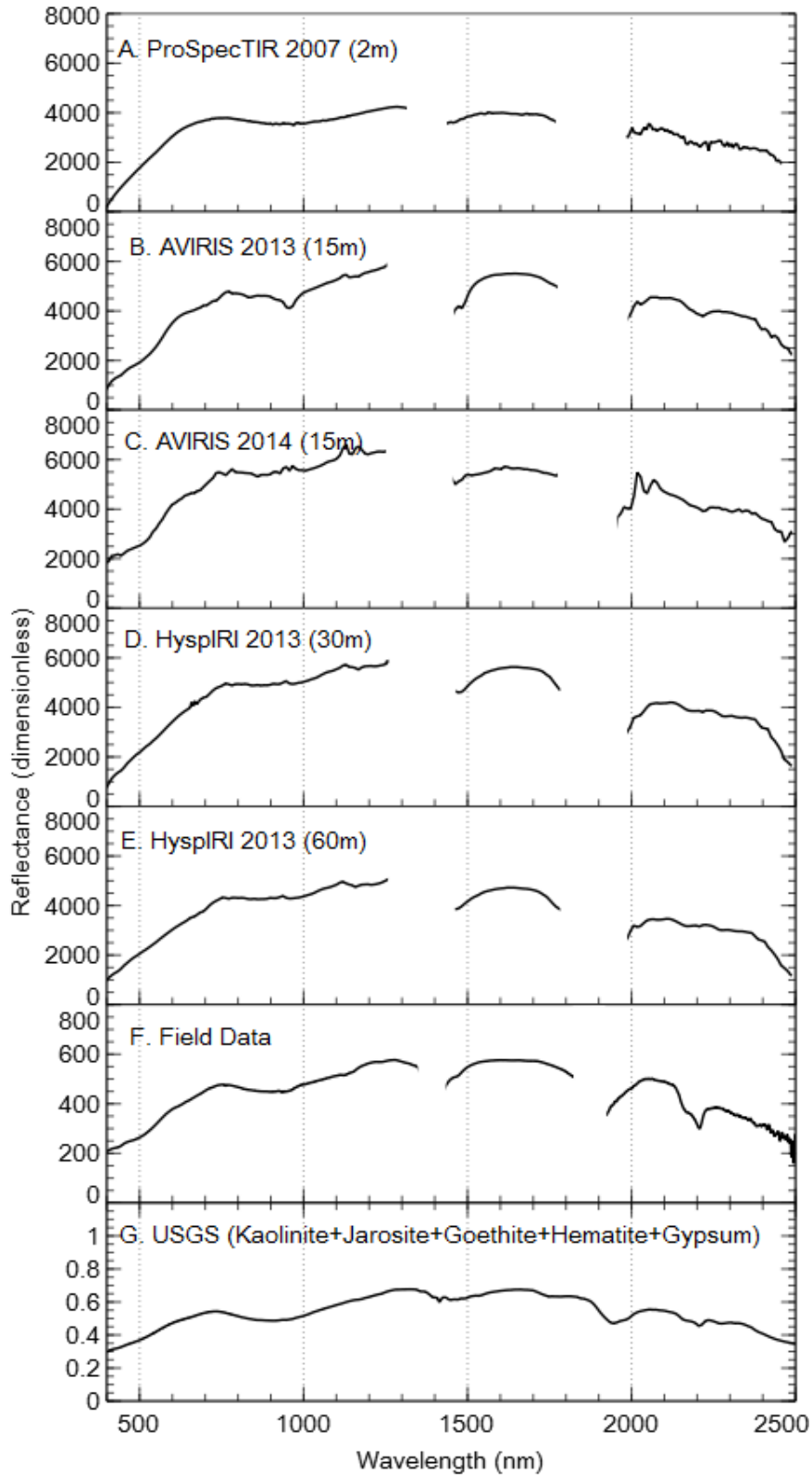
Fig. 16 Iron hydroxide and clay endmembers. Plotted curves are spectral averages of endmembers within the class "iron hydroxides and clays"
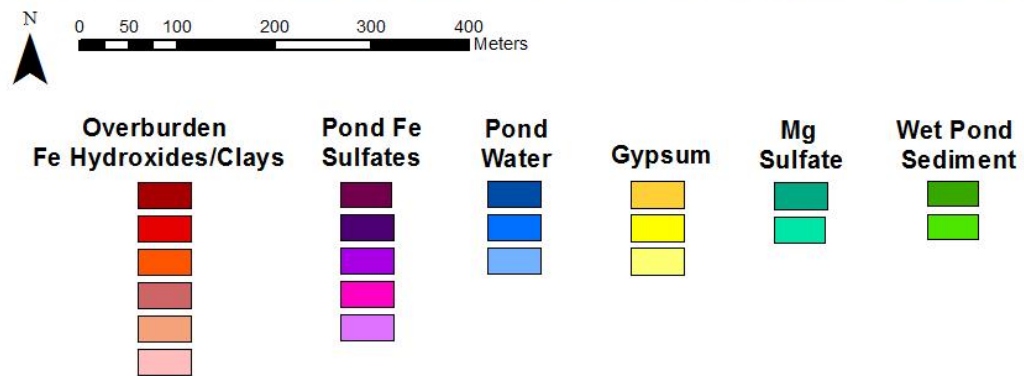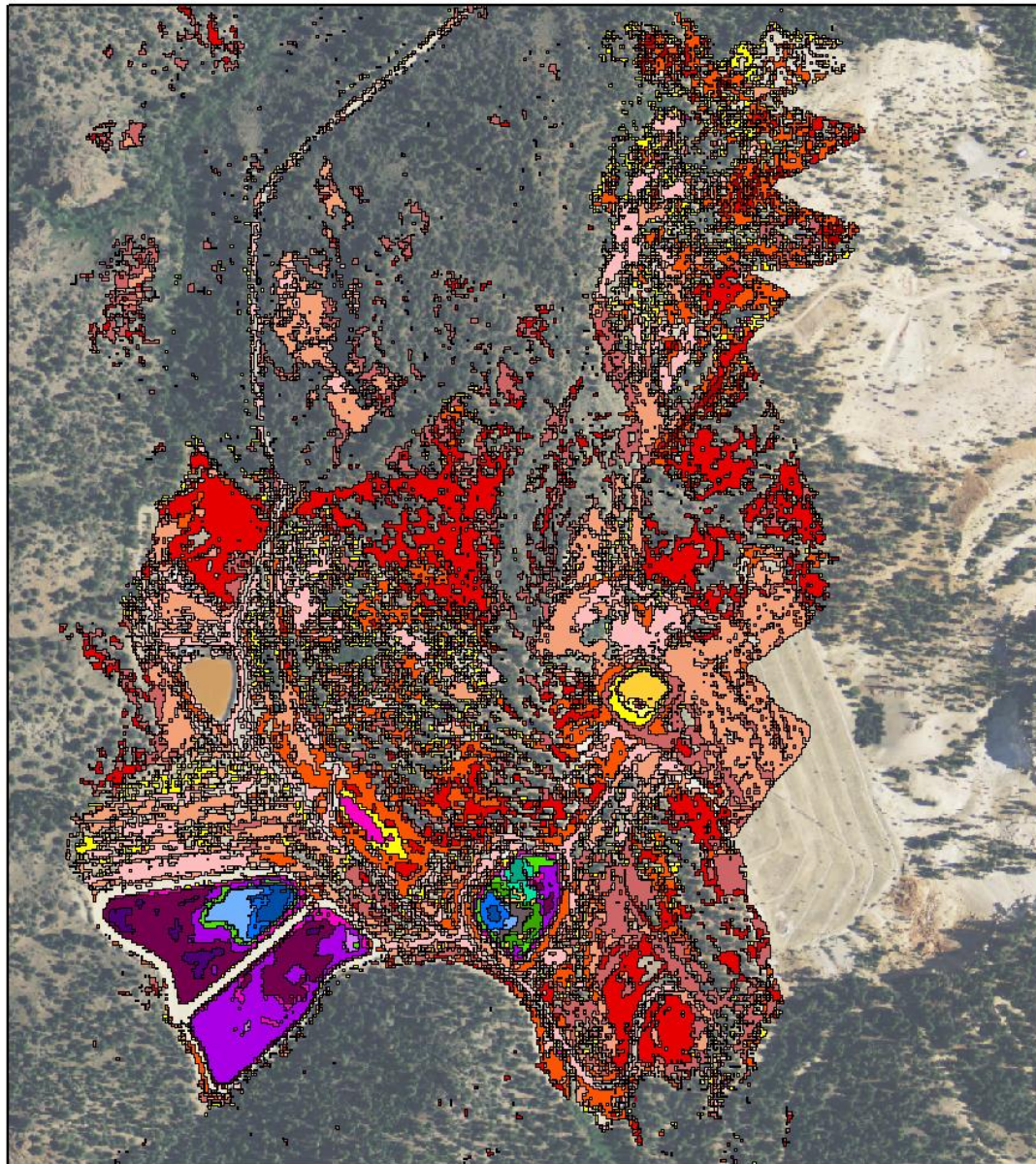
Fig. 17 ProSpecTIR Class Map, 311 channels, 2 meter pixels. Image acquired 08/17/2007
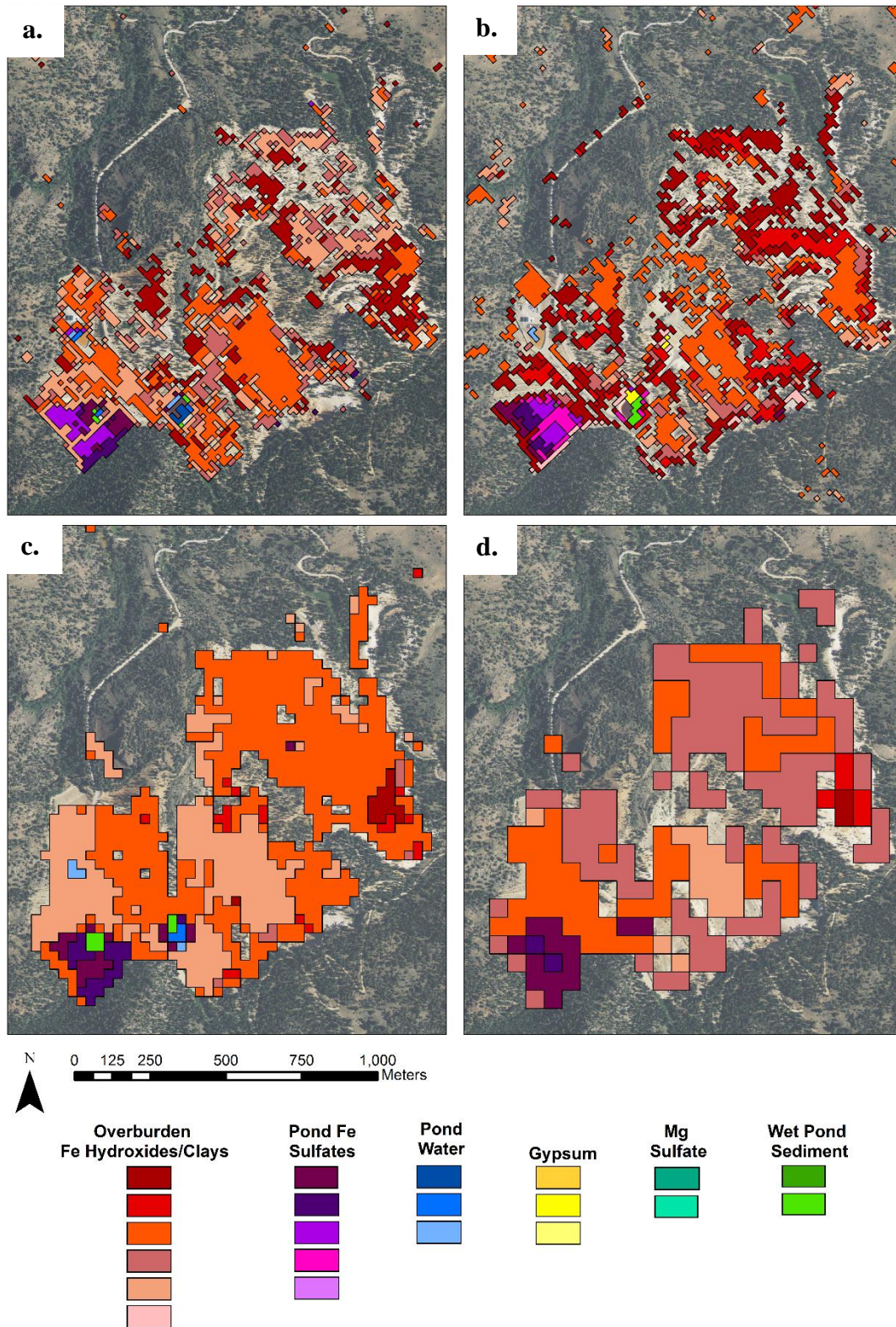
Fig. 18 AVIRIS and HyspIRI product Class Map, 204 channels. A) 09/19/2013 15 meter pixel, B) 09/19/2014 15 meter pixel, C) 09/19/2013 30 meter pixel, D) 09/19/2013 60 meter pixel
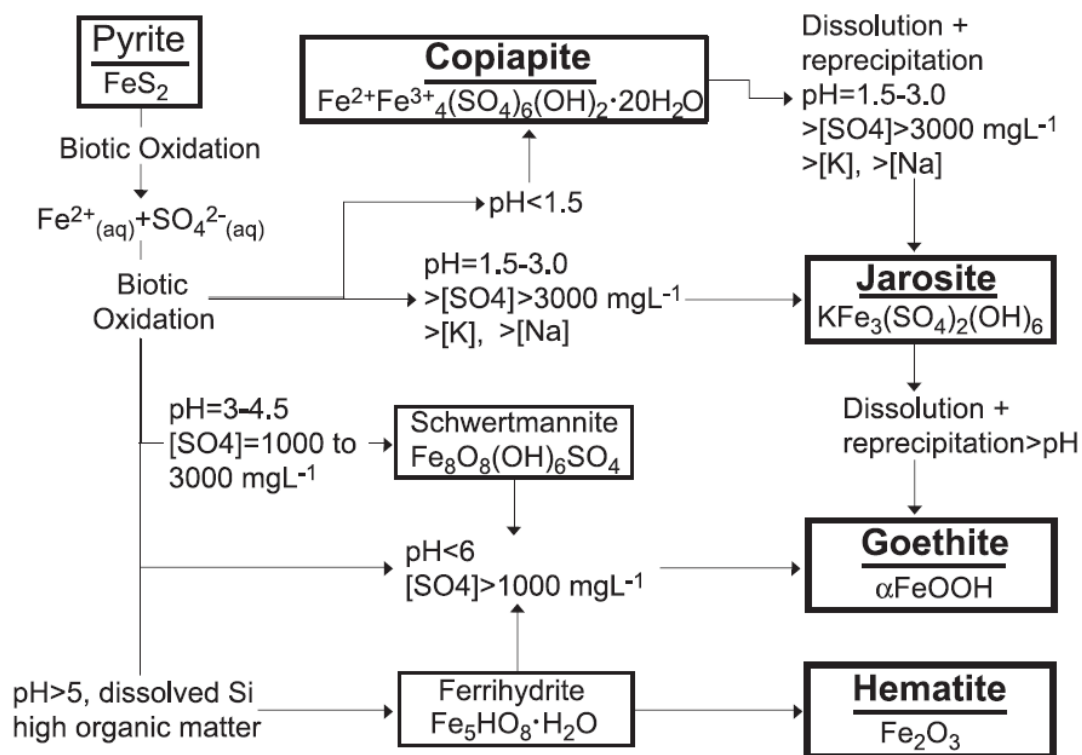
Fig. 19 Model of the accumulation of secondary iron minerals in iron sulfide-rich mine waste environments according to pH values. From Montero et al. (2005)

9.   References

Alpers CN, Blowes DW, Nordstrom DK, Jambor JL (1994) Secondary minerals and acid mine-water chemistry. In: Jambor JL, Blowes DW (eds) Environmental Geochemistry of Sulfide Mine-Wastes, Mineral. Assoc. Can. Short Course, vol 22, pp 247–270

Bigham JM (1994) Mineralogy of ochre deposits formed by sulfide oxidation. In: Jambor JL, Blowes DW (eds) Environmental Geochemistry of Sulfide Mine-Wastes, Mineral. Assoc. Can. Short Course, vol 22, pp 105– 133

Campbell JB, Wynne RH (2011) Ch.17 Plant sciences. In: Introduction to remote sensing 5th edition. Guilford Press, New York, New York, pp 549-584

Cloutis EA, Hawthorne FC, Mertzman SA, Krenn K, Craig MA, Marcino D, Methot M, Strong J, Mustard JF, Blaney DL, Bell JF, Vilas F (2006) Detection and discrimination of sulfate minerals using reflectance spectroscopy. Icarus, 184: 1: 121-157. doi:10.1016/j.icarus.2006.04.003

Crowley JK (1991) Visible and near-infrared (0.4-2.5 μm) reflectance spectra of playa evaporate minerals. Journal of geophysical research 96: B10: 16,240-16,240. doi:10.1029/91JB01714

Crowley JK, Williams DE, Hammarstrom JM, Piatak N, Chou IM, Mars JC (2003) Spectral reflectance properties (0.4-2.5 μm) of secondary Fe-oxide, Fe-hydroxide, and Fe-sulphate-hydrate minerals associated with sulphide-bearing mine wastes. Geochemistry: Exploration, Environment, Analysis 3: 3: 219-228. doi:10.1144/1467-7873/03-001

Crowley JK, Williams DE, Hammarstrom JM, Piatak N, Mars JC, Chou IM (2006) Spectral reflectance properties (0.4-2.5 um) of secondary Fe-oxide, Fe-hydroxide, and Fe-sulfate-hydrate minerals associated with sulfide-bearing mine waste. USGS Open File Report Rep. 2003-196

Environmental Protection Agency (2003) Implementation, information, and statutory obstacles impede achievement of environmental results from EPA's National Hardrock Mining Framework, Report No. 2003-P-00010

Gillespie AR (1992) Enhancement of multispectral thermal infrared images; Decorrelation contrast stretching. Remote sensing of environment 42: 2: 147-155. doi:10.1016/0034-4257(92)90098-5

Hunt GR, Ashley RP (1979) Spectra of altered rocks in the visible and near infrared. Economic Geology 74: 1613-1629. doi:10.2113/gsecongeo.74.7.1613

Hunt GR, Salisbury JW (1970) Visible and near-infrared spectra of minerals and rocks: I silicate minerals. Modern Geology 1: 283-300

Kopackova V (2014) Using multi spectral feature analysis for quantitative pH mapping in a mining environment. International Journal of Applied Earth Observation and Geoinformation 28: 28-42. doi:10.1016/j.jag.2013.10.008

Kruse FA (1999) Visible-infrared sensors and case studies. In: Rencz AN (ed) Remote sensing for the Earth sciences: Manual of remote sensing, 3rd ed. John Wiley & Sons, Inc, pp 567-611

Langmuir D (1997) Ch.12 Iron and sulfur geochemistry. In: Aqueous environmental geochemistry. Prentice-Hall, Upper Saddle River, New Jersey, pp 431-474

Lottermoser BG (2003) Ch.3 Mine water. In: Mine wastes. Springer, New York, pp 83-141

Mielke C, Boesche NK, Rogass C, Kaufmann, Christoph G, de Wit M (2014) Spaceborne mine waste mineralogy monitoring in south Africa, application for modern push0broom missions: Hyperion/OLI and EnMAP/Sentinel-2. Remote Sens. 6: 6790-6816. doi:10.3390/rs6086790

Montero IC, Brimhalla GH, Alpers CN, Swayze, GA (2005) Characterization of waste rock associated with acid drainage at the Penn mine, California, by ground-based visible to short-wave infrared reflectance spectroscopy assisted by digital mapping. Chemical Geology, 215, 453-472. doi:10.1016/j.chemgeo.2004.06.045

MSE Technology Applications, Inc. (2000) Mine waste technology program, annual report. http://www2.epa.gov/nscep. Accessed 30 October 2015

Nordstrom DK, Jenne EA, Ball JW (1978) Redox equilibria of iron in acid mine waters. In: Jenne EA (ed) Chemical Modeling in Aqueous Systems: Speciation, Sorption, Solubility, and Kinetics, Am. Chem. Soc. Symp. Ser., vol 93, pp 51– 79

Nordstrom DK (1982) Ch.3 Aqueous pyrite oxidation and consequent formation of secondary iron minerals. In: Kittrick JA, Acid sulfate weathering Soil science society of America. SSSA special publication, No. 10, pp 37-58

Riaza A, Buzzi J, Garcia-Melendez E, Vazquez I, Bellido E, Carrere V, Müller A (2012) Pyrite mine waste and water mapping using Hymap and Hyperion hyperspectral data. Environmental Earth Science, 66, 1957-1971. doi: 10.1007/s12665-011-1422-0

Sherman DM, Waite TD (1985) Electronic spectra of Fe^{3+} oxides and oxide hydroxides in the near IR to near UV. American Mineralogist 70: 1262-1269

Swayze GA, Smith KS, Clark RN, Sutley SJ, Pearson RM, Vance SJ, Hageman PL, Briggs PH, Meier AL, Singleton MJ, Roth S (2000) Using imaging spectroscopy to map acidic mine waste. Environmental Science Technology, 34, 47-54. doi:10.1021/es990046w

Tucker CJ (1979) Red and photographic infrared linear combinations for monitoring vegetation. Remote Sensing of Environment 8: 127-150. doi:10.1016/0034-4257(79)90013-0

US Geologic Service (2013) USGS Digital spectral library 06. http://speclab.cr.usgs.gov/spectral.lib06/. Accessed 30 October 2015

Chapter 4—Thesis Summary, Conclusions, and Recommendations

1. In a controlled laboratory setting, the spectral response (in the VSWIR region) of small volumes of ferric iron dominated AMD water was unique when compared to non-iron rich impaired water, turbid river water, and DI water. The unique spectral curves of Leviathan AMD water were imitated with iron sulfate solutions. The spectral curves of Leviathan AMD water with < 500 mg/L Fe^{3+} plotted very similarly to laboratory iron sulfate solution curves with comparable Fe^{3+} concentrations. Likewise, spectral curves of Leviathan AMD water with > 500 mg/L Fe^{3+} plotted very similarly to laboratory iron sulfate solution curves with comparable Fe^{3+} concentrations. This led us to conclude that subtle changes in ferric iron concentration could also be observed with hyperspectral remotely sensed imagery.

2. Specifically, the region between 0.35 and 0.625 μm could be used to approximately quantify ferric iron concentration in mine waters. This method is best suited for mine waters that are acidic, high in sulfate, and low in turbidity.

3. Using multi-season airborne hyperspectral imagery, the unique spectral response of mine water was identified when compared to various other natural water bodies. The spectral curves of acidic water collected in ponds at the Leviathan Mine were characterized by shifted peak reflectance to red wavelengths (638-690 nm) and high overall reflectance. These curves serve as an analog to mine pit lake water curves.

4. Environmental influences such as bottom reflectance, turbidity, biomass, and seasonality, strongly affected the spectral signatures of mine water spectral curves. Shallow waters exhibited a shift in peak reflectance from 638 to 690 nm, and displayed higher overall reflectance. Turbidity also shifted peak reflectance and increased overall reflectance. Biomass contributed to a prominent absorption feature at 675 nm, which was also emphasized by bottom surface brightness.

5. Airborne spectral curves were similar to those from the laboratory experiment in that they displayed strong absorption at the blue and green wavelengths. However, airborne curves were not directly compared to laboratory spectral curves for qualitative analysis due to variability from bottom reflectance, turbidity, and biomass. For this application, a study area with more constant water levels and larger variation in pH and ferric iron concentration is needed.

6. These results show potential for use of hyperspectral imagery in the monitoring of pit lake water quality. As a minimum, pit lake waters which have a spectral curve with peak reflectance in the red region can be identified as having potentially poor water quality linked to acidic pH and dissolved iron. These techniques should be limited to higher spatial resolution data, or over large areas of mine-affected waters at least 2300 square meters in size.

7. Multi-season airborne hyperspectral imagery with varying spatial scales were also used to characterize mine waste surfaces. As a minimum, 60 meter imagery could differentiate surfaces that had direct contact with AMD and those that did not. Additionally, 2 to 30 meter imagery could also differentiate mine waste surfaces such as mine water, gypsum resulting from AMD neutralization, and algal coated sediment. Chiefly, the 2 meter imagery could further differentiate various depths of mine water and additional sulfate minerals.

8. Given the results of spatial scale comparison, we recommend a spatial resolution of at least 30 meters in hyperspectral imagery for the application of environmental monitoring at mine waste sites. For superlative identification of discrete minerals, spatial scales of < 2 meters (such as those acquired with low flying unmanned aerial vehicles) are recommended.